Novel Methods for Deriving Snow Data from Remote Cameras and Applications to Wildlife Habitat and Ungulate Management

A Thesis
Presented in Partial Fulfillment of the Requirements for the
Degree of Master of Science
with a
Major in Natural Resources
in the
College of Graduate Studies
University of Idaho
by
Kaitlyn M. Strickfaden

Approved by
Major Professors: David Ausband, Ph.D.; Timothy Link, Ph.D.
Committee Members: Janet Rachlow, Ph.D.; Jocelyn Aycrigg, Ph.D.
Department Administrator: Janet Rachlow, Ph.D.

December 2022

Abstract

Snow, in both its quantity and its dynamics, is a key driver of many geophysical and ecological processes and is well understood from a purely hydrologic perspective. However, snow as it affects wildlife habitat and survival is only understood very broadly despite its potential effects on thermoregulation, movement, foraging, and escape from predation over winter. This knowledge gap can largely be attributed to the lack of snow data at temporal and spatial scales meaningful to wildlife. Remote cameras are already widely used in wildlife research and potentially are a low-cost, low-maintenance option for collecting snow data at high spatial and temporal resolutions in complex forested terrain. My thesis explores how remote cameras can be used to collect snow and weather data and then applies these data to two wildlife habitat questions.

I begin by asking what hydrometeorological data can be derived from remote camera images. Chapter 1A focuses on snow depth and a package I built in program R to measure snow depth without the use of permanent snow stakes deployed in the camera viewshed. The potential use of this code in distance sampling with remote cameras is heavily emphasized because it may be of interest to other users of the package. However, for this thesis, no distance sampling was performed; the code was only implemented in creating virtual snow stakes which could be used to measure snow depth in the camera images for Chapters 2 and 3. This R package provides a means for other camera studies to collect fine-scale snow depth data without potentially impacting wildlife behavior. Chapter 1B focuses on correcting air temperature measurements made by cameras and deriving precipitation phase from combined image data and temperature data. The temperature correction model gives researchers more confidence in the temperature measurements collected by their cameras. However, precipitation phase is complicated to discern because of the relatively low resolution of images and the effects of wind and canopy interception.

My other two chapters use these methods and models to address two wildlife habitat questions. One, what biophysical conditions promote retention of snow in complex forested terrain? Using snow and temperature data derived from the remote cameras and biophysical data collected at the camera sites, I built a model predicting locations of snow refugia in complex forested terrains. Knowledge about late-season snow cover provides insight into how forests can be managed to promote snow retention and thus promote habitat for snow-dependent wildlife species. Two, how do snow characteristics and winter severity affect the movement and distribution of ungulates over winter? I built a model relating deer and elk detections at my cameras to snow depth and temperature from cameras and snow density and hardness from on-site measurements. Snow density and hardness are expected to change drastically to the possible detriment of ungulates, but these properties are not included in current winter severity indices; My model is the first attempt at including these snow properties to better define winter severity for ungulates in a changing climate.

Acknowledgements

I have a long, long list of people to thank. Of course, I have to start by thanking Dave Ausband and Tim Link for putting their faith in me to see this project through, for guiding and teaching me, and for kicking me in the pants when I needed it (which was more often than I'd like to admit). Thank you also to Adrienne Marshall for all of her advice on coding and statistics, Leona Svancara for asking me great questions and pushing me to answer great questions, Jocelyn Aycrigg and Janet Rachlow for taking time out of their schedules to serve on my committee, and all four of these wonderful mentors for being role models to me as fellow women in science.

Thank you to my two rockstar field technicians Reagan Barron and Elijah Disse and to my additional volunteer field helpers George Naughton, Clayton Christiensen, Jaz Ammon, Pete Rebholz, and Macy Swift for spending many hours out in the cold and snow to collect all of the amazing data I used for this project. Thank you also to my image analysts Clayton Christiensen, Ryan Martin, and Star Campos Garcia for sifting through the hundreds of thousands of images we collected throughout the main field season.

Thank you to my fellow Ausband lab members Ariana Cerreta, Matt Nelson, Pete Rebholz, and Bri Winkel for letting me talk through problems with you, providing feedback on thesis drafts and presentations, and bringing camaraderie and laughter to the office. Thank you to my fellow Link lab members Paul Robinson and Ian Hellman for your technical expertise as I built all of my field equipment and figured out how to take hemispherical photographs. Thank you to Colin Campbell and Doug Cobos of Meter Environment for providing the ATMOS station that I used for my temperature accuracy assessment. Thank you to University of Idaho Experimental Forest, Bennett Lumber Products, Idaho Department of Lands, City of Troy, and Mark Solomon for giving me access to your lands for conducting my research. Finally, thank you to the Northwest Climate Adaptation Science Center for funding this project (Cooperative Agreement G19AC00284), to the Idaho Department of Fish and Game for providing many of the cameras I used, and to the Coeur d'Alene Tribe and the U.S. Fish and Wildlife Service for partnering with me on this project.

Dedication

This thesis is dedicated to my amazing friends, family, and boyfriend for supporting me and cheering me on even when you didn’t really know what I was yammering on about most of the time. I truly couldn’t have done this without every one of you, and I am incredibly grateful.

Table of Contents

List of Tables

List of Figures

Chapter 1A: Deriving Snow Depth Data from Camera Images

Abstract

Remote cameras are used to study demographics, ecological processes, and behavior of wildlife populations. Additionally, cameras have successfully been used to measure snow depth with physical snow stakes. Cameras can provide fine-scale snow data as well as data for wildlife abundance estimation simultaneously within the same image. Current snow data sources are often broad scale either spatially or temporally, making the fine-scale snow data collected by cameras valuable. Recently developed models that adapt distance sampling techniques to cameras can provide accurate population density estimates if encounter rates are unbiased. However, logistical constraints, namely concerns that physical instruments at camera sites may influence animal behavior, discourage installation of instruments to facilitate collecting these data. Given that environmental and distance data are inherently contained within images, potential inferences that could be made using these data are lost. To address this, we developed an R package called *edger* to superimpose "virtual" objects onto images. The *edger* package uses a simple, fast, and effective edge detection algorithm to identify pixels belonging to the edges of an object in one image that can then be recolored in subsequent images, eliminating the need for objects to be left at camera sites throughout their deployment. The virtual objects can then be used to manually take measurements. Functions in the *edger* package are highly customizable to account for a variety of deployment conditions. We validated the method for snow depth estimation using camera data from Latah County, Idaho, USA. We found that snow depth estimates from a virtual object superimposed using functions in the *edger* package were within 5 cm of true snow depth from a physical snow stake in 88% of observations. *edger* can provide researchers with a means to take critical measurements for ecological studies without the use of physical objects which may alter animal behavior.

Introduction

Hundreds of thousands of remote cameras are deployed worldwide to collect data on wildlife population dynamics, ecology, and behavior (Burton et al. 2015, Steenweg 2017). However, environmental "bycatch" data (Hofmeester et al. 2020) contained in these images are rarely used. Given the millions of images collected in camera studies every year, this is an immense source of unused but potentially valuable data. For instance, Sun et al. (2021) used cameras to collect data about vegetation characteristics to make inferences about habitat use of sandhill cranes (*Grus canadensis*), woodland caribou (*Rangifer tarandus*), and white-tailed deer (*Odocoileus virginianus*) that could not be found using satellite data.

Boelman et al. (2019) noted the need for fine-scale snow data across broad regions for use in wildlife studies. Remotely sensed, satellite-based, and modelled snow data products are relatively coarse-scale (typically hundreds of meters to several kilometers) and may be prone to error in complex terrain (Sirén et al. 2018), while finer-scale *in situ* measurements from weather stations, terrestrial or airborne LiDAR, structure-from-motion, and human observers can be costly, labor-intensive, and limited in spatial or temporal distribution (Kinar and Pomeroy 2015, Fernandes et al. 2018). Conversely, remote cameras are fine-scale in both time and space (e.g., detections at < daily intervals in < 100 m viewsheds), collect data remotely with minimal maintenance, can be deployed almost anywhere, and are relatively inexpensive to purchase and operate relative to common hydrometeorological equipment such as ultrasonic depth sensors (Steenweg et al. 2017). Cameras with physical snow stakes installed in the camera viewshed have been successfully used to collect snow depth data in several hydrologic studies (Dickerson-Lange et al. 2017, Sirén et al. 2018, Bongio et al. 2019). If the hundreds of thousands of cameras being used annually for wildlife studies could simultaneously collect snow data, this would provide a valuable data source spanning diverse and complex terrain. These data can be used directly in wildlife and hydrological studies, or they can be used to validate and improve existing snow models and data products which are known to be less certain under forest canopies and in heterogenous terrain (Pimentel et al. 2017, Sirén et al 2018, Thackeray et al. 2018, Kostadinov et al. 2019).

Additionally, distance sampling methods have been adapted for camera studies (Howe et al. 2017). Traditional distance sampling uses the number of animals detected from a point or transect to generate a density estimate, assuming detection rates of animals decrease as distance from the observer increases (Bessone et al. 2020). Camera distance sampling exchanges the human observer for a camera and adjusts detection rates dependent on the morphological and movement characteristics of the focal species and the viewshed area (Howe et al. 2017). As with traditional distance sampling, camera distance sampling relies on accurately estimating distances to detected animals. Palencia et al. (2021) used rocks and other natural objects placed in the camera viewshed at 5-m intervals to assess distances, while Corlatti et al. (2020) used wooden stakes. Camera distance sampling can generate reasonable density estimates if assumptions can be properly met (Corlatti et al. 2020, Harris et al. 2020, Palencia et al. 2021, Henrich et al. 2022). These assumptions include random distribution of cameras, availability of animals for detection in the camera viewshed (e.g., animals are not underground), and unbiased encounter rates (i.e., animals are not either attracted to or deterred from entering the camera viewshed; Corlatti et al. 2020, Henrich et al. 2022).

However, several factors must be considered when permanent objects are installed at camera sites to collect snow depth or distance data. Equipment must be purchased and then moved to and deployed at each camera site, which can be very expensive and labor-intensive depending on the number of camera sites; the cost, size, and weight of the equipment; and the remoteness of the study site. Objects may also draw further attention from human recreationists, making camera sites more subject to tampering and theft (Meek et al. 2019).

A primary concern is that objects installed at camera sites can further alter animal movement patterns or behavior beyond the disturbance already caused by the cameras themselves (Rowcliffe et al. 2008, Henrich et al. 2022; Meek et al. 2014). Many researchers have speculated about the influences of cameras and other objects on animal movement and behavior in studies using cameras (Séquin et al. 2003, Meek et al. 2014, Hofmeester et al. 2017, Bessone et al. 2020, Corlatti et al. 2020). For example, experimental data collected concurrently with the present study recorded several dozen unique instances of animals ranging in size from snowshoe hare (*Lepus americanus*) to moose (*Alces alces*) interacting with 1.5-m snow stakes (Strickfaden, unpubl. data). Documented interactions included looking at the snow stakes and subsequently changing their movement paths, stopping to smell them, or rubbing on them (Fig. 1). Hofmeester et al. (2017) noted carnivores and ungulates most often interacted with markers left in camera viewsheds in their study, which we also found to be the case. While interacting with objects, animals may move, topple, or destroy them, making them useless or less accurate for data collection. The objects, by acting as a lure, may cause animals to be detected when they otherwise would not have been, which may increase encounter rates. Conversely, an unknown number of animals may avoid cameras because of objects left in viewsheds, which might be particularly problematic for studies of low-density or elusive animals for which every detection is crucial (Bessone et al. 2020). Bias in encounter rates of animals, either due to animals spending more time in camera viewsheds interacting with objects or avoiding them altogether, can subsequently bias density estimates from distance sampling (Corlatti et al. 2020, Palencia et al. 2021, Henrich et al. 2022).

The use of "reference images" combined with image processing techniques provides means by which distance and depth measurements can be remotely acquired, precluding issues with animal responses to objects left in the camera viewshed. While we have not found any studies using reference images to measure snow depth, they have been used in camera distance sampling studies. Rowcliffe et al. (2011), Harris et al. (2020), and Howe et al. (2017) took still images or videos of researchers standing in the camera viewshed at known distances during deployment or retrieval and compared these images to the positions of detected animals to gauge distances. Henrich et al. (2022) placed transparent images containing distance markers on top of images containing animals to assess distance. Caravaggi et al. (2016) took this one step further by superimposing gridlines onto images, thereby eliminating the need to reference other images to measure distances in one image. Hofmeester et al. (2017) also suggested that markers in an image taken during deployment could be superimposed onto other images to measure distances.

The general objective of this research is to extend the utility of automated camera data by developing a method to measure lengths and heights or gauge distances in images without leaving objects in the camera viewshed. To accomplish this, we developed a package in the R programming language (R Core Team 2020) named *edger* (https://github.com/kaitlynstrickfaden/edger) which superimposes a "virtual" object onto images based on that object's position in a reference image. The virtual object can then be used to manually measure depths or heights or to gauge distances in images. *edger* is written in the R programming language (R Core Team, 2022), which is free, open-source, and frequently used in natural resources applications, making it accessible to natural resource practitioners. We describe the methodology behind *edger*, outline the main package functions, present a validation of the method for snow depth estimation using remote camera data, and provide some considerations for obtaining the best results using the package.

Methods

Edger Package Overview

The basis of the *edger* package is Canny edge detection (Canny 1986). Canny edge detection is robust but mathematically very simple, allowing it to be implemented very quickly even on high-resolution images. Pixels in an image are converted to grayscale and then assigned an x gradient and y gradient value. For a particular pixel, the x gradient is a numerical value indicating the difference in luminance (brightness) of that pixel versus the pixels immediately to the left and right, and the y gradient is the same for the pixels immediately above and below. From the x and y gradients, a gradient magnitude is computed using $\sqrt{x^2 + y^2}$, where x is the x gradient value and y is the y gradient value for each pixel. A larger gradient magnitude indicates a more defined edge. The *imager* package in R (Barthelme 2021) contains functions that perform these computations. For more details about the edge detection algorithm, refer to the “edger_methodology” vignette on the GitHub page for the package.

The *edger* package makes use of functions in the *imager* package to identify and change the color value of edge pixels in a particular region of the image. Pixels falling within a region of interest (ROI) with a gradient magnitude greater than a user-defined threshold are identified and assigned a new color value. By defining the ROI as the regions of a reference image taken during a camera’s deployment which contain objects of interest, *edger* can extract the outlines and gradations of those objects and superimpose them onto the remaining images from the camera to create virtual objects. Options to shift and rotate the recolored pixels allow the user to account for changes in the camera viewshed during deployment (e.g., when a human or animal bumps the camera or the camera mount slips). The user can manually take measurements using the virtual objects (Fig. 2). On the x plane, these measurements may include animal body length or width of an ephemeral stream; in the y plane, they may include snow depth, animal body height, or height of growing vegetation; and in the z plane, they may include animal distance or visibility distance through fog or turbid water.

Three main *edger* functions of interest are *edger_single, edger_multi,* and *edger_testr* (Table 1). Other functions listed in Table 1 are helper functions used by these three main functions. The *edger_testr* function provides an interface for the user to define the ROI in an image and interactively choose appropriate threshold, shift, and rotation values for that image. The *edger_single* function finds and displays edges in a single image, while the *edger_multi* function finds edges in one or several reference images and superimposes those edges onto other images. These functions do not overwrite the original image but instead create a new recolored copy of the image with "_edger" appended to the file name so the original image can be retained. The *edger_meta* function which is built into the *edger_single* and *edger_multi* functions attributes metadata such as date, time, temperature, and trigger mode from the original image to the recolored image. Both *edger_single* and *edger_multi* can take ROI coordinates and values output by the *edger_testr* function as inputs. Further details about the use of these three functions are available in the "edger_use" vignette.

The inputs of the three main functions are very similar. Images are input as file paths to the images on the computer or hard drive. If ROI coordinates are not input into calls to the *edger_single* and *edger_multi* functions, then the functions open a window which prompts the user to draw the ROI on the reference image. Threshold gradient magnitude values can range from 1-100, with lower values extracting both weak and strong edges and higher values extracting only strong edges. Other arguments included in all functions are the number of ROIs to define in each reference image and the color to assign to the virtual object.

The *edger_multi* function includes additional function arguments to facilitate processing image sets. The user can provide the number of reference images to use if reference objects appear in multiple images. The first *n* images in the vector of file paths are the reference images, and the rest of the images in the vector are recolored using edges found in the *n* reference images. The user can specify whether to display images as they are being processed so they can be checked for quality, though this slows the processing speed. Finally, the user can choose sequential or parallel processing and how many computer cores to use if running in parallel. Of these, the only required inputs are the image file paths, the ROI coordinates (which the function will prompt the user to draw on if not given as a function argument), and an appropriate threshold value. The other inputs provide additional efficiency and flexibility to image processing. Once all inputs are set as desired, the *edger_multi* function can process thousands of images with no user intervention.

Method Validation

We used images from 21 Reconyx® Hyperfire I cameras which were deployed on Moscow Mountain (approximately 46.8°N, 116.9°W) in Latah County, Idaho, USA to capture a variety of snow conditions. Twelve of these were deployed from January – May 2020, while 9 were deployed from March-May 2020. Cameras were deployed at least 1.5 m from the ground to prevent them from being buried in snow. Cameras were programmed to record 2.9 megapixel timelapse images every hour, including night hours. A physical snow stake was deployed in the viewshed of each camera for measuring snow depth. Each snow stake was a 150 cm section of 3.8 cm-diameter white PVC pipe that was marked with 2-cm gradations in black permanent marker and 10-cm gradations in brightly colored electrical tape. The pipe was fastened to a 180 cm U-post with cable ties and deployed 4–15 meters from the camera. The location of the physical snow stake in the viewshed was dependent on the terrain and the presence of objects that might block the view of the snow stake. The distance from the snow stake to the camera was recorded on deployment. Snow depth was measured by one observer using the physical snow stake in all images after cameras were retrieved. We expect minimal uncertainty in measurements with the physical snow stake, therefore the snow depth measurements made using the physical snow stake were considered truth for the purpose of the validation.

To compare snow depth measurements made with a virtual object to those made with a physical snow stake, we superimposed a “virtual snow stake” (VSS) onto images using functions in the *edger* package. The recolored pixels were shifted to the left or right by 100–200 pixels (~0.5 m) so that the VSS would not be superimposed on top of the physical snow stake or natural objects. However, the VSS had to be relatively close to the physical snow stake so that in situ variation in snow depth would not confound the accuracy assessment. Three observers (none of whom were the observer who measured snow depth with the physical snow stake) measured snow depth in the images using the VSS. Observers were instructed not to refer to the physical snow stake when making measurements with the VSS. This allowed us to directly compare the snow depth measurements made with a verified method (the physical snow stake) to snow depth measurements made in the same images using the novel method (the VSS). To evaluate the accuracy of the VSS method, we assessed the mean bias error (the directional difference between the two daily averages) and the mean absolute error (the magnitude of difference between the two daily averages) in VSS measurements versus physical snow stake measurements. We also calculated the Nash-Sutcliffe Efficiency (NSE) for each observer's VSS measurements for each camera. While NSE is commonly used to assess the fit of hydrologic models with observed data, we used it to determine how closely an observer's VSS measurements (the "model") compared to the measurements made with the physical snow stake (the "observations") at a particular camera site. We performed analyses in the R programming language (R Core Team 2022).

Results

We used 30,700 of the 49,000 timelapse images collected to assess the accuracy of the VSS compared to a physical snow stake. We removed images from analysis which did not contain snow (37% of images) or did not have a full view of the physical snow stake or VSS due to changes in the camera viewshed during deployment caused by the weight of snow on cameras (2% of images). The mean snow depth recorded in images using the physical snow stake was 55 cm, and the maximum snow depth recorded in any image was 140 cm. Observers recorded 81,960 hourly snow depth estimates, accounting for repeat observations by multiple observers (5 cameras were not scored by every observer). Images were recorded over 1,325 camera days. Observers on average were able to process approximately 1,100 images per hour.

The mean bias error was approximately -0.5 cm, indicating a slight tendency for observers to underestimate snow depths with the VSS. Mean bias error was -0.47 cm in daytime images and -0.59 cm in night images. Mean bias error per observer was -1.39, 0.78, and -0.99 cm. The mean absolute bias error was 2.55 cm in daytime images and 2.59 cm in night images. Mean absolute bias error per observer was 3.27, 1.82, and 2.58 cm. Overall, 88% of snow depth estimates were within 5 cm of true snow depth, and less than 1% of snow depth estimates differed more than 10 cm from the true snow depth. Hourly bias error ranged from -26 cm to 14 cm, and daily bias error ranged from -14 cm to 12 cm. The narrower range in the daily bias error values indicates that large errors in individual images were mitigated when snow depth estimates were averaged over the day.

The NSE values for each camera per observer ranged from -0.02 to 0.998 (Table S1). However, the majority (77%) of the camera/observer combinations had an NSE value greater than 0.90, indicating high agreement between the physical snow stake and VSS estimates. Those combinations with lower NSE values were typically cameras that were deployed for a shorter duration.

Based on visual assessment of time series plots (Fig. 3), more absolute error tended to occur at deeper snow depths. Error in snow depth estimates at particular cameras was also variable among observers (Fig. 4). Some cameras had approximately equal error in terms of direction, magnitude, and range among the three observers (e.g., Camera 04), while other cameras had very different patterns in errors among observers (e.g., Camera 08). Factors such as distance to the snow stake and camera height do not appear to have caused a noticeable difference in error.

Discussion and Conclusions

We created a software package that can be used to manually estimate snow depths and distances at remote camera stations without the need to leave equipment at the camera site. While other algorithms and packages are available which can automatically measure snow depth in images containing a physical snow stake (e.g., Bongio et al. 2019), *edger* fills a different need by allowing for simultaneous collection of data on wildlife and snow conditions without any concerns of altering movement or behavior via the presence of a physical snow stake. In addition to avoiding potential issues with animal behavior, this method also greatly reduces field cost and effort for studies, because each field team only needs one snow stake or one set of distance markers to deploy all cameras.

Despite its potentially strong influence on animal population demography, many studies do not collect fine-scale snow depth measurements. Instead, they use snow presence or general depth categories (Curtis et al. 2014, Gilbert et al. 2017), or they use data from satellites at relatively coarse-scales and less reliable under forest canopies (Horne et al. 2019). The *edger* package we developed will allow more studies using cameras to measure snow depth. Snow can be measured at one or multiple points in an image depending on the scale of data needed for a particular research question. These fine-scale data are useful for multiple natural resources disciplines and potentially allow for new inferences into wildlife population parameters and forest-snow interactions (Olson et al. 2021).

Sirén et al. (2018) found snow depth estimates from Snow Data Assimilation Systems (SNODAS) data in complex forested terrain comparable to our study area were frequently biased by >10 cm on average when compared to measurements taken with a camera and a physical snow stake or to direct measurements made in the field. Conversely, our evaluation found that <1% of snow depth estimates using the VSS were biased by >10 cm, and 88% of hourly snow depth estimates using the VSS were within 5 cm of physical snow stake measurements, indicating a high degree of accuracy compared to another common snow depth data source.

There was often variability in snow depth measurements made by different observers (Fig. 4), likely due to differences in spatial reasoning skills. Observer training and careful placement of the physical object in the reference image, as discussed later, may both improve the accuracy of snow depth measurements and reduce interobserver variability. The ability for observers to accurately measure snow depth may be further modified by the distance to the snow stake, which could lead to lower precision in snow depth estimates; camera height, which could affect the observer's perception of the top of the snowpack; and whether a particular image was taken during the day or at night, though we did not find strong evidence any of these factors affected snow depth measurements in our dataset. The effect each of these factors have on the potential for bias warrant further evaluation beyond what is possible with this small pool of data relative to the number of contributing factors.

Observers were explicitly instructed to ignore the physical snow stake while measuring snow depth with the VSS. We have three lines of evidence this instruction was followed. First, there were no numbers written on the physical snow stake, thus deriving quantitative measurements from the physical snow stake was difficult. Second, the magnitude and direction of errors individual observers reported was variable both within a camera and among all cameras they analyzed. We might expect more systematic errors (i.e., snow depth was always the same, always underestimated, or always overestimated) if observers were basing their VSS estimates off the physical snow stake. Third, the observers were incentivized based on the length of time worked and not by the accuracy of their snow depth estimates.

Qualitatively, camera height did not appear to affect bias error or absolute bias error, but it is an important consideration when deploying cameras to collect both wildlife and snow data. Cameras placed too high may fail to detect target wildlife, limiting possible inferences (Meek et al. 2016). Conversely, cameras placed too low are at risk of being buried in snow, making the data collected useless until the snow melts or is cleared away. Adjusting camera heights throughout the study period is only an option in study areas with winter access. It would also require the user to retake reference images for each camera height. The optimal camera height for a study will depend on the study species, the expected snow depths in the study area, and the cost of missing detections.

Though distance sampling methods specifically for camera studies have only been recently developed (Howe et al. 2017), they have been found to be accurate when assumptions about the availability and movement of animals can be met (Corlatti et al. 2020, Harris et al. 2020). Density estimates from camera distance sampling are sensitive to biases in encounter rates (Howe et al. 2017). Virtual distance markers may make these methods more robust and defensible to researchers interested in using this method. Though an application to distance sampling was not included in this study, the methods would be similar to those performed by Caravaggi et al. (2018). A reference image would need to be taken containing objects placed at regular distance intervals in the camera viewshed. These objects would then be superimposed onto images and used to gauge the distance of the animal from the camera when it was detected.

Perhaps the most important step in using the *edger* package is collecting suitable reference images containing the object of interest. There must be strong contrast between the object and any gradations on it, in the case of snow depth measurement, and strong contrast between the object and its background to obtain the best results. If the gradations on the object are weak, or if the background contains litter, shrubs, or other substrate that creates strong edges, the virtual object may be indistinct. A white object with black gradations drawn on it, or vice versa, provides the strongest contrast. A tarp or sheet could be held behind the object, or an individual could stand behind it to create a more homogenous background if a randomly selected camera site provides poor conditions for locating the edges of the object. However, this method may not be suitable if the entire camera viewshed is filled with brush blocking the camera from having a clear view of the snow stake or distance markers.

The amount of processing time needed to superimpose a virtual object onto images depends on the image resolution and number of pixels which are recolored. Reconyx® Hyperfire cameras take 2.9-megapixel images; *edger* was able to process approximately 1,200 Reconyx images per hour using one 1.6 GHz processor of a Lenovo Thinkpad® computer during testing of the package. Parallel processing across five computer processors doubled to tripled the number of images processed per hour. Many game camera brands can record images >2.9 megapixels. However, the higher image resolution of many remote camera brands can be the result of pixel interpolation, where the values of pixels captured by the image sensor are used to fill in the values of new pixels to make the image larger (Rovero and Zimmermann 2016). Though *edger* works on images of any size, the greater total number of pixels in higher-resolution images increases the processing time per image. We also speculate the interpolation weakens edges between pixels, which are the basis of *edger*'s function. We suggest against using the maximum resolution capable by the camera and instead suggest using the image resolution which matches the image sensor. This does not cause any noticeable detraction in image quality and allows a camera to operate for a longer time on a single memory card.

The threshold value should be set to minimize the number of extraneous pixels recolored while maximizing the utility of the virtual object. While a small number of extraneous pixels makes little difference in the processing time of a single image, the extra processing time may compound when applied over hundreds or thousands of images. Processing time can also be reduced by only recoloring a subset of all images being collected (i.e., only superimposing a virtual snow stake onto a timelapse image at a certain time of day, or only superimposing virtual distance markers onto images containing animals).

Additional time must be spent determining the correct input values before processing. If the camera viewshed does not change throughout its deployment, this simply requires finding the proper threshold value. However, if the viewshed changes, the shift and rotation values needed to superimpose the virtual object onto the correct position must also be found. This further requires splitting the image set into two sets, one before and one after the viewshed change, and processing them separately. Camera jitter, or rapid and unpredictable movement of the camera caused by instability of the camera on its mount or by wind, is the most difficult viewshed change to resolve because the camera viewshed is changing randomly across many images. If jitter is severe, then accurate measurements may not be possible. Care should be taken when deploying cameras to ensure they are fastened tightly and when maintaining cameras to keep the viewsheds constant. When possible, cameras should be deployed on large-diameter or sub-dominant trees to minimize jitter caused by wind.

Hofmeester et al. (2017) speculated superimposing markers onto images could avoid potential effects of markers on animal behavior but might come at the cost of some precision with measurements. We found this to be the case during the method validation. Discerning the top of the snowpack to measure snow depth could be very difficult at some camera sites, particularly at more open sites. This can be ameliorated by placing the reference object at the same distance from the camera as some natural object such as a tree or rock so the natural object can be used to provide some spatial context. However, in the case of snow depth measurements, the reference snow stake should not be placed immediately next to the natural object because of the potential for the natural object to alter snow accumulation and melt processes.

Important areas for future work include evaluating sources of error in a VSS relative to physical snow stakes (i.e., distance to the snow stake, daytime versus nighttime images, etc.) and using the VSS to better characterize snow depth heterogeneity below the forest canopy. Our R package can also be used to evaluate snow depth or distance measurements in existing historical camera datasets for which these measurements are desirable, provided the camera viewshed can be replicated so reference images can be recorded. Altogether, the *edger* package allows for extraction of additional data from massive existing datasets, providing opportunities for new scientific inquiry and understanding across multiple fields including wildlife ecology, hydrology, snow science, and forest ecology.

References

Barthelme, S. 2021. imager: image processing library based on 'CImg'. R package version 0.42.10. https://CRAN.R-project.org/package=imager.

Bessone, M., Kühl, H.S., Hohmann, G., Herbinger, I., N'Goran, K.P., Asanzi, P., Da Costa, P.B., Dérozier, V., Fotsing, E.D.B., Beka, B.I., Iyomi, M.D., Iyatshi, I.B., Kafando, P., Kambere, M.A., Moundzoho, D.B., Wanzalire, M.L.K., and Fruth, B. 2020. Drawn out of the shadows: Surveying secretive forest species with camera trap distance sampling. Journal of Applied Ecology 57:963–974.

Boelman, N.T., Liston, G.E., Gurarie, E., Meddens, A.J.H., Mahoney, P.J., Kirchner, P.B., Bohrer, G., Brinkman, T.J., Cosgrove, C.L., Eitel, J.U.H., Hebblewhite, M., Kimball, J.S., LaPoint, S., Nolin, A.W., Pedersen, S.H., Prugh, L.R., Reinking, A.K., and Vierling, L.A. 2019. Integrating snow science and wildlife ecology in Arctic-boreal North America. Environmental Research Letters 14:010401.

Bongio, M., Arslan, A.N., Tanis, C.M., and De Michele, C. 2019. Snow depth estimation by time-lapse photography: Finnish and Italian case studies. The Cryosphere. Preprint. https://doi.org/10.5194/tc-2019-193.

Burton, A.C., Neilson, E., Moreira, D., Ladle, A., Steenweg, R., Fisher, J.T., Bayne, E., and Boutin, S. 2015. Wildlife camera trapping: A review and recommendations for linking surveys to ecological processes. Journal of Applied Ecology 52:675–685.

Canny, J. 1986. A computational approach to edge detection. IEEE Transactions on Pattern Analysis and Machine Intelligence 6:679–698.

Caravaggi, A., Zaccaroni, M., Riga, F., Schai-Braun, S.C., Dick, J.T.A., Montgomery, W.I., and Reid, N. 2016. An invasive-native mammalian species replacement process captured by camera trap survey random encounter models. Remote Sensing in Ecology and Conservation 2(1):45–58.

Corlatti, L., Sivieri, S., Sudolska, B., Giacomelli, S., and Pedrotti, L. 2020. A field test of unconventional camera trap distance sampling to estimate abundance of marmot populations. Wildlife Biology 2020(4):1–11. https://doi.org/10.2981/wlb.00652.

Curtis, J.A., Flint, L.E., Flint, A.L., Lundquist, J.D., Hudgens, B., Boydston, E.E., and Young, J.K. 2014. Incorporating cold-air pooling into downscaled climate models increases potential refugia for snow-dependent species within the Sierra Nevada ecoregion, CA. PLoS ONE 9(9):e106984. https://doi.org/10.1371/journal.pone.0106984.

Dickerson-Lange, S.E., Gersonde, R.F., Hubbart, J.A., Link, T.E., Nolin, A.W., Perry, G.H., Roth, T.R., Wayand, N.E., and Lundquist, J.D. 2017. Snow disappearance timing is dominated by forest effects on snow accumulation in warm winter climates of the Pacific Northwest, United States. Hydrological Processes 31:1846–1862.

Fernandes, R., Prevost, C., Canisius, F., Leblanc, S. G., Maloley, M., Oakes, S., Holman, K., and Knudby, A. 2018. Monitoring snow depth change across a range of landscapes with ephemeral snowpacks using structure from motion applied to lightweight unmanned aerial vehicle videos. The Cryosphere 12:3535-3550.

Gilbert, S.L., Hundertmark, K.J., Person, D.K., Lindberg, M.S., and Boyce, M.S. 2017. Behavioral plasticity in a variable environment: snow depth and habitat interactions drive deer movement in winter. Journal of Mammalogy 98(1):246–259.

Harris, G.M., Butler, M.J., Stewart, D.R., Rominger, E.M., and Ruhl, C.Q. 2020. Accurate population estimation of Caprinae using camera traps and distance sampling. Scientific Reports 10:17729. doi: 10.1038/s41598-020-73893-5.

Henrich, M., Hartig, F., Dormann, C.F., Kühl, H.S., Peters, W., Franke, F., Peterka, T., Šustr, P., and Heurich, M. 2022. Deer behavior affects density estimates with camera traps, but is outweighed by spatial variability. Frontiers in Ecology and Evolution 10:881502. doi: 10.3389/fevo.2022.881502.

Hofmeester, T.R., Rowcliffe, J.M., and Jansen, P.A. 2017. A simple method for estimating the effective detection distance of camera traps. Remote Sensing in Ecology and Conservation 3(2):81–89.

Hofmeester, T.R., Young, S., Juthberg, S., Singh, N.J., Widemo, F., Andrén, H., Linnell, J.D.C., and Cromsig, J.P.G.M. 2020. Using by-catch data from wildlife surveys to quantify climatic parameters and timing of phenology for plants and animals using camera traps. Remote Sensing in Ecology and Conservation 6(2):129–140.

Horne, J.S., Hurley, M.A., White, C.G., and Rachael, J. 2019. Effects of wolf pack size and winter conditions on elk mortality. Journal of Wildlife Management 83(5):1103–1116.

Howe, E.J., Buckland, S.T., Després-Einspenner, M., and Kühl, H.S. 2017. Distance sampling with camera traps. Methods in Ecology and Evolution 8:1558–1565.

Kinar, N.J., and Pomeroy, J.W. 2015. Measurement of the physical properties of the snowpack. Reviews of Geophysics 53:481–544.

Kostadinov, T.S., Schumer, R., Hausner, M., Bormann, K.J., Gaffney, R., McGwire, K., Painter, T.H., Tyler, S., and Harpold, A.A. 2019. Watershed-scale mapping of fractional snow cover under conifer forest canopy using lidar. Remote Sensing of Environment 222:34–49.

Meek, P.D., Ballard, G.A, Claridge, A., Kays, R., Moseby, K., O'Brien, T., O'Connell, A., Sanderson, J., Swann, D.E., Tobler, M., and Townsend, S. 2014. Recommended guiding principles for reporting on camera trapping research. Biodiversity Conservation 23:2321–2343.

Meek, P.D., Ballard, G.A, and Falzon, G. 2016. The higher you go the less you will know: Placing camera traps high to avoid theft will affect detection. Remote Sensing in Ecology and Conservation 2(4):204–211.

Meek, P.D., Ballard, G.A., Sparkes, J., Robinson, M., Nesbitt. B., and Fleming, P.J.S. 2019. Camera trap theft and vandalism: Occurrence, cost, prevention and implications for wildlife research and management. Remote Sensing in Ecology and Conservation 5(2):160–168.

Olson, L.O., Van Deelen, T.R., Storm, D.J., and Crimmins, S.M. 2021. Understanding environmental patterns of canid predation on white-tailed deer (*Odocoileus virginianus*). Canadian Journal of Zoology 99:912–920.

Palencia, P., Rowcliffe, J.M., Vicente, J., and Acevedo, P. 2021. Assessing the camera trap methodologies used to estimate density of unmarked populations. Journal of Applied Ecology 58:1583–1592.

Pimentel, R., Herrero, J., and Polo, M.J. 2017. Quantifying snow cover distribution in semiarid regions combining satellite and terrestrial imagery. Remote Sensing 9:995.

R Core Team. 2022. R: A language and environment for statistical computing. R Foundation for Statistical Computing, Vienna, Austria. <https://www.R-project.org/>

Rowcliffe, J.M., Field, J., Turvey, S.T., and Carbone, C. 2008. Estimating animal density using camera traps without the need for individual recognition. Journal of Applied Ecology 45: 1228–1236.

Rowcliffe, J.M., Carbone, C., Jansen, P.A., Kays, R., and Kranstauber, B. 2011. Quantifying the sensitivity of camera traps: An adapted distance sampling approach. Methods in Ecology and Evolution 2:464–476.

Séquin, E.S., Jaeger, M.M., Brussard, P.F., and Barrett, R.H. 2003. Wariness of coyotes to camera traps relative to social status and territory boundaries. Canadian Journal of Zoology 81(12):2015–2025.

Sirén, A.P.K., Somos-Valenzuela, M., Callahan, C., Kilborn, J.R., Duclos, T., Trager, C., and Morelli, T.L. 2018. Looking beyond wildlife: Using remote cameras to evaluate accuracy of gridded snow data. Remote Sensing in Ecology and Conservation 4(4):375–386.

Steenweg, R., Hebblewhite, M., Kays, R., Ahumada, J., Fisher, J.T., Burton, C., Townsend, S.E., Carbone, C., Rowcliffe, J.M., Whittington, J., Brodie, J., Royle, J.A., Switalski, A., Clevenger, A.P., Heim, N., and Rich, L.N. 2017. Scaling-up camera traps: monitoring the planet's biodiversity with networks of remote sensors. Frontiers in Ecology and Evolution 15(1):26–34.

Sun, C., Beirne, C., Burgar, J.M., Howey, T., Fisher, J.T., and Burton, C., 2021. Simultaneous monitoring of vegetation dynamics and wildlife activity with camera traps to assess habitat change. Remote Sensing in Ecology and Conservation 7(4):666-684.

Thackeray, C.W., Fletcher, C.G., and Derksen, C. 2018. Quantifying the skill of CMIP5 models in simulating seasonal albedo and snow cover evolution. Journal of Geophysical Research: Atmospheres 120:5831–5849.

Figures and Tables

Table 1. Functions in the edger package. Bolded function names are main package functions.

Name	Description
edger_df_to_im_bw	Converts a data frame to a black and white image.
edger_df_to_im_color	Converts a data frame to a color image.
edger_display	Shows an image.
edger_extract	Extracts the coordinates and unique pixel identifiers of edge pixels.
edger_identify	Identifies edge pixels in the region of interest (ROI). The ROI is either drawn on by the user or the coordinates are taken in as a function argument.
edger_im_to_df	Converts an image to a data frame and assigns unique pixel identifiers.
edger_im_to_grad	Calculates gradient magnitude values for each pixel in an image.
edger_match	Finds edge pixels in an image and performs any shifts and rotations.
edger_meta	Attributes metadata from original image to recolored image.
edger_multi	Finds edge pixels in the first image(s) and recolors those edge pixels in other input images.
edger name	Find name of new recolored image.
edger_overlay	Recolors edge pixels in an image and saves the image.
edger_recolor	Assigns new color value to edge pixels.
edger_save	Saves an image.
edger_single	Finds edge pixels in an input image.
edger_testr	Launches a user interface for drawing a region of interest and selecting threshold, shift, and rotation values for input images.

Fig. 1. Images from remote cameras deployed in Idaho, USA showing wildlife interacting with snow stakes. Top left is white-tailed deer (*Odocoileus virginianus*), top right is moose (*Alces alces*), bottom left is wild turkey (*Meleagris gallopavo*), and bottom right is snowshoe hare (*Lepus americanus*).

Fig. 2. Workflow of edger package from camera deployment to data extraction.

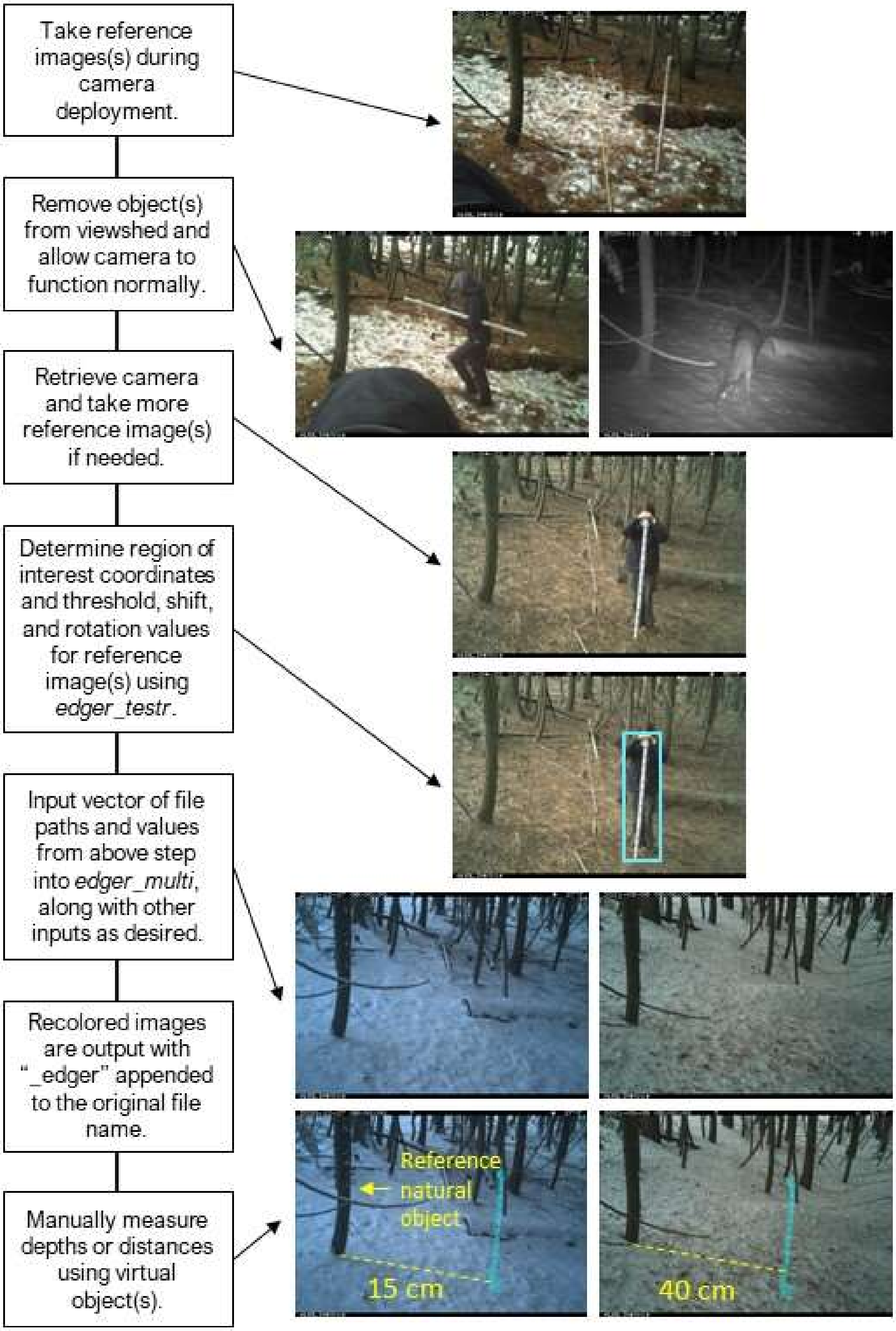

Fig. 3. Time series plots of snow depth measurements with a virtual snow stake (VSS) for each observer (colored lines) versus measurements with a physical snow stake (shaded area) for a subset of cameras. The colors of the Nash-Sutcliffe Efficiency (NSE) values in the upper righthand corner of each plot correspond with the line color for each observer.

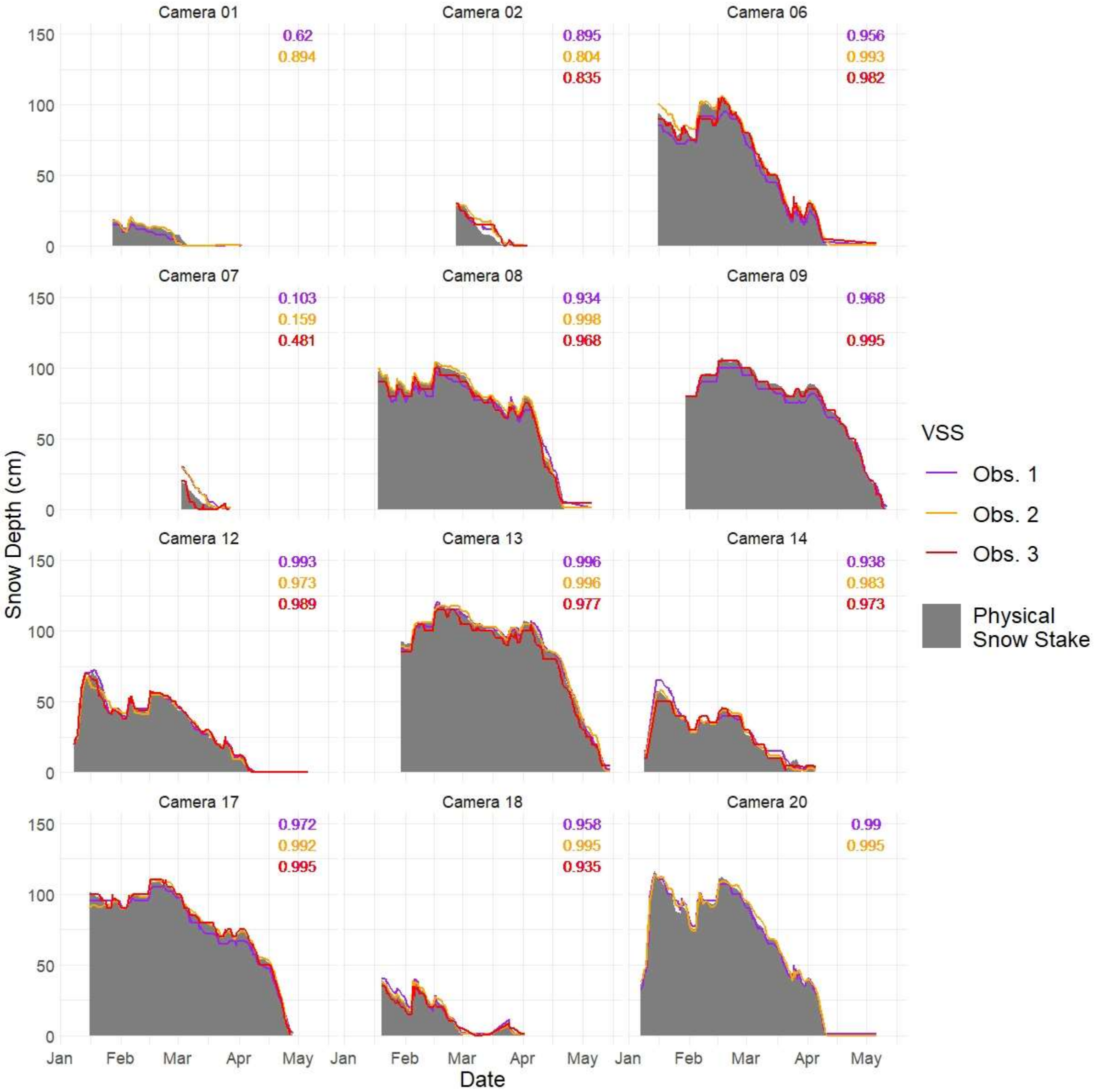

Fig. 4. Mean (points) and range (whiskers) of A) daily averaged bias error and B) daily averaged absolute bias error in snow depth measurements made with a virtual snow stake (VSS) compared to a physical snow stake by observer and camera. Line colors correspond to the color of the camera ID number below.

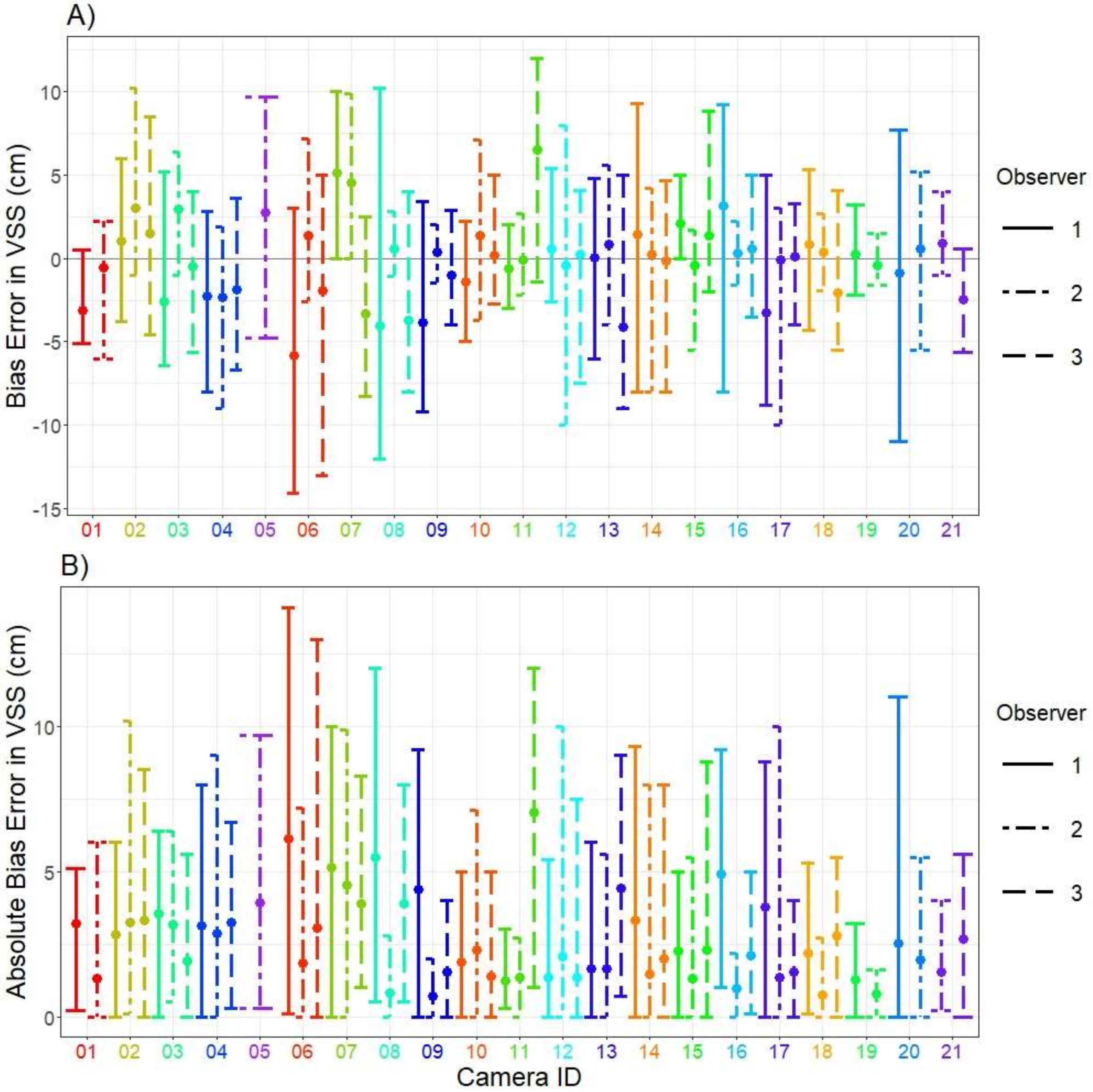

Chapter 1B: Deriving Weather Data from Camera Images

Abstract

Remote cameras provide important insight into wildlife demography, ecological processes, and behavior. Hydrometeorological information at fine scales is very valuable, and cameras may also be able to provide these data if their reliability can be verified and/or if methods can be developed to derive such data from remote cameras. Cameras often have built-in temperature sensors that output a temperature reading with every image. Images can also be used to identify local precipitation events. The objective of this chapter was to 1) assess the accuracy of temperature readings made by Reconyx® cameras, 2) build a model to correct biased temperature readings made by cameras, and 3) determine whether precipitation events and precipitation phase can be reliably determined from images alone. An energy balance model was developed and tested using data from two cameras paired with weather stations which collected corrected air temperature measurements and other environmental data. Mean bias error of uncorrected temperatures was -0.41°C, so cameras tended to underestimate temperatures, but the maximum daily temperature could be overestimated by as much as 20°C by cameras. In general, camera temperatures agreed well with temperatures from the weather station, with the correlations being 0.72 for uncorrected temperatures and 0.88 for corrected temperatures. Precipitation events and phase could not be reliably determined using still images. Given the widespread use of cameras for natural resources applications and particularly for wildlife studies, this corrective temperature model improves the accuracy and reliability of temperature data from cameras and is useful for multiple natural resource disciplines.

Introduction

Remote cameras are an increasingly common data collection tools in natural resources (Steenweg et al. 2017). Many remote cameras record temperature measurements along with each image. When paired with the images, these temperature measurements can be used to investigate the timing of phenologically important events such as snowmelt and leaf emergence (Hofmeester et al. 2020) and to detect patterns in activity levels of wildlife species (Hofmann et al. 2016). Despite this, temperature measurements by cameras are rarely used in ecological studies, and instead studies often use temperature data from other sources such as iButtons® (Maxim Integrated Products) or nearby weather stations (e.g., Buchholz et al. 2021) to assess these relationships.

No major camera manufacturer lists accuracy information about temperature readings from its cameras, which may be a reason for their minimal use (Buchholz et al. 2021). Previous research found temperature measurements made by Moultrie® and Bushnell® cameras have little correlation ($R^2 < 0.05$) with true air temperature (Sirén et al. 2018; A. Sirén, pers. comm.). We know of only two peer-reviewed studies which examine temperature measurements by cameras. Hofmann et al. (2016) deployed air temperature loggers with their Reconyx® RapidFire™ Professional (PC90) cameras, but they only reported on correlation between the air temperature measurements and not any measure of bias. Hofmeester et al. (2020) compared temperature measurements from Reconyx Hyperfire™ (HC500) cameras to those from a single weather station in their 200 km^2 study area and reported a mean temperature bias of +1.9°C. Using a single weather station for comparison may not have captured fine-scale variations in air temperature across their study area, and they did not assess bias as a function of any site covariates except for distance to coast. Given the widespread use of cameras both for research and recreational purposes, the lack of temperature accuracy information for the most popular camera models is a knowledge gap needing to be addressed. If temperature measurements from cameras are biased, then camera users would benefit from having a means to correct the temperature measurements to maximize the utility of their cameras.

Images also contain visual information about precipitation events. Cameras have been used in studies to determine the occurrence of precipitation events. Liu et al. (2015) used a broad-scale camera deployed to capture images of an entire hillslope to determine the elevation of the rain-snow transition. Floyd and Weiler (2008) used cameras and climate stations to examine the interactions of canopy cover, snow accumulation and melt, and precipitation phase locally. Droghini and Boutin (2018) found that wolves (*Canis lupus*) reduce their activity levels and movement speeds after local snow events >5 cm depth. Rain-on-snow events are often the focus of these studies because these events cause earlier and large amounts of run-off, making them of interest hydrologically (Floyd and Weiler 2008). Rain-on-snow events can reduce survival of elk (*Cervus canadensis*) due to ice layers blocking forage access (Mech et al. 2001). However, if precipitation data are needed for a study, cameras are often paired with another instrument to determine precipitation phase. It would be advantageous if cameras could be used alone to determine precipitation phase because it would reduce instrumentation needs for camera studies. Knowledge about local weather would be beneficial as it would take full advantage of a huge dataset of local and spatially extensive information from cameras.

The general scientific objective of this study was to expand the utility of remote cameras for collecting accurate fine-scale hydrometeorological data. Our first specific objective was to determine the accuracy of temperature measurements made by Reconyx Hyperfire II Professional Series (hereafter "HP2X") cameras. We developed an energy balance model for the HP2X cameras using data collected from the cameras themselves and temperature, wind speed, and radiation data collected by two meteorological stations. Our second objective was to investigate if cameras could be used to identify precipitation events with the aim of pairing precipitation event with concurrent temperature measurements to determine the phase of the precipitation event (i.e., rain or snow).

Methods

The study area for this experiment was a south-facing edge of a small clearing in Latah County, ID at an elevation of 1070 m above sea level. The ground cover is a mix of exposed soil, shortgrass, and litter. Two HP2X cameras (hereafter temperature cameras) with the dark green case color were deployed facing south at a height of 1.25 m. Both cameras had similar understory cover and were under similar canopy cover (~ 20%). The temperature cameras were programmed to take a timelapse photo every 15 minutes throughout their deployment. Temperature cameras were deployed on 20 March 2021, checked once for proper function on 3 April 2021, and retrieved on 17 April 2021. This timing coincides with a period of moderate shortwave radiation loading in the northern hemisphere.

To model air temperature from camera temperature, we used the following equation:

$$T_a = T_{cam} - \frac{\alpha_s[F_a S_{bd} + F_s(S_{bd}\rho_s)] + \alpha_L(F_a L_a + F_s L_s) - \alpha_L \sigma (T_{cam} + 273.15)^4}{c_p\left[\left(1.4 * 0.135\sqrt{\frac{u}{d}}\right) + \frac{4\alpha_L \sigma (T_{cam} + 273.15)^3}{c_p}\right]} \qquad \textit{Eq. 1}$$

This equation is a modification of the equation in Campbell and Norman (1998) for the energy balance of a leaf from which the terms for evapotranspiration have been removed. This model describes the camera's temperature measurement as a result of 1) heat added by shortwave and longwave radiation from the sun and surrounding objects, 2) heat lost through longwave radiation emitted by the camera itself, and 3) equilibration of the camera with true air temperature controlled by the wind speed and physical properties of the camera (Table 2). By accounting for these different sources of heat gain and loss, the actual air temperature can be calculated from the camera temperature.

We deployed an ATMOS 41 weather station (METER Group, Inc., Pullman, WA; hereafter "ATMOS") within 20 m of both cameras in an area with sparse canopy cover. The ATMOS collected air temperature, wind speed, and shortwave radiation data every 15 minutes throughout its deployment. The ATMOS uses the wind speed and radiation data it collects to automatically correct its air temperature measurements with <0.5°C accuracy (Meter Environment 2021). Thus, temperature measurements made by the ATMOS were considered truth for our purposes. A separate meteorological station at the site recorded longwave radiation data every 30 minutes throughout the experiment using a Kipp and Zonen CG-1 pyrgeometer. We took hemispherical photographs at each camera location to calculate incoming shortwave radiation and approximate the proportion of the camera's surroundings composed of sky and surrounding objects (i.e., the view factors of sky and surroundings). Shortwave radiation estimates from the hemispherical photographs were calculated using Hemisfer software (Thimonier et al. 2010).

Some variables needed for this model, the shortwave and longwave absorptivity of the camera and the reflectivity of the ground, were unknown. To approximate these values, we used the Solver functionality (Fylstra et al. 1998) in Microsoft Excel (2016). After inputting the environmental variables into the energy balance equation, we used Solver to iteratively solve for the absorptivity and reflectivity values minimizing the sum of squared differences between the true and modelled air temperatures. There was a snow event on 21 March which left snow on the ground until approximately 25 March. We calculated a snow-covered ground reflectivity for those days and a bare ground reflectivity for all other days.

We assessed differences between true air temperature from the ATMOS, uncorrected camera temperature, and corrected camera temperature using several metrics both throughout the entire study period and on an hourly basis. We calculated R^2 values to determine the goodness of fit between the true air temperature and the camera temperatures. We also calculated the mean bias error (the directional difference between the true air temperature and the camera temperature), mean absolute bias error (the magnitude of difference between the true air temperature and the camera temperature), and root mean squared deviation (RMSD) of uncorrected and corrected camera temperatures. Additionally, we determined the percent of camera observations falling within 2°C and 1°C of the true air temperature. We analyzed the data in the R programming language (R Core Team 2022).

Precipitation events were recorded in images from 138 Reconyx Hyperfire I and Hyperfire II cameras deployed from October 2021 – May 2022 (hereafter precipitation cameras; Chapters 2 & 3). Images were taken hourly or via motion-trigger. A precipitation event was recorded if snow was seen to accumulate or if visual markers, such as streaks or opacities, could be seen in the image which might be indicative of precipitation.

Results

The temperature cameras collected 5,390 observations. The values for shortwave absorptivity, longwave absorptivity, bare ground reflectivity, and snow-covered ground reflectivity which minimized the sum of squared differences were 1.00, 0.87, 0.230, and 0.412, respectively. The average air temperature recorded by the ATMOS was 5.0°C, while the average temperature recorded by the cameras was 4.6°C, suggesting a slight tendency for cameras to underestimate temperatures on average. However, more than 75% of daily maximum temperatures were overestimated by cameras by at least 5°C, and one day's maximum temperature was overestimated by 20°C, so high temperatures can be dramatically overestimated by the cameras. Minimum temperatures were less error-prone, with the daily minimum temperature never being underestimated by cameras by >4°C (Fig. 5).

The model was able to improve temperature estimates of cameras based on all metrics. The R^2 value comparing the goodness of fit of the uncorrected camera temperatures to the true air temperatures was 0.73, and the R^2 value for the corrected temperatures was 0.88. The mean bias error of the uncorrected camera temperatures was -0.41°C, while the mean bias error of the corrected camera temperatures was -0.13°C. The mean absolute bias error of the uncorrected camera temperatures was 1.92°C, while the mean absolute bias error of the corrected camera temperatures was 1.28°C. Mean bias error and mean absolute bias error varied throughout the course of the day. Error tended to increase as the amount of shortwave radiation increased (Fig. 6). The root mean squared deviation (RMSD) of uncorrected temperature observations was 7.32, while the RMSD of corrected temperature observations was 3.28. Hourly RMSDs were lowest in the night to early morning hours (6PM-7AM) and highest in the midday hours (11AM-4PM; Fig. 7). RMSD was greater for the corrected temperatures than for the uncorrected temperatures between 8-10AM and again from 4-5PM, indicating the model was overcorrecting temperatures at these times (i.e., the uncorrected camera temperature was closer to true air temperature than the corrected temperature).

For most observations (55.7%), both the uncorrected and corrected camera temperatures were within 2°C of truth. Uncorrected temperatures recorded by the temperature cameras were within 2°C of true air temperature for 66% of observations and within 1°C for 32% of observations. The model-corrected camera temperatures were within 2°C of true air temperature for 81% of observations and within 1°C of true air temperature for 54% of observations. These are improvements in the percent of observations falling within these thresholds of 23% and 69%, respectively. The improvement in temperature accuracy varied across days (Fig. 8).

Precipitation events were recorded in 74,500 of the 867,000 images collected by the precipitation cameras. However, the resolution of images made it challenging to determine the occurrence of precipitation events during the day unless snow accumulated during the event. Even if visual markers indicative of precipitation were observed in images, it was often not clear if these visual markers were the result of falling precipitation, fog, snow displaced from the canopy, or snow blown by the wind. Thus, further exploration of precipitation events and phase was abandoned.

Discussion

The energy balance equation improved the accuracy of temperature measurements from HP2X cameras. We decreased bias error, nearly halved the RMSD, and improved the goodness of fit of the HP2X camera temperatures with the true air temperatures using the energy balance equation. The corrected temperature measurements had a mean bias error and mean absolute bias error of -0.13°C and 1.28°C, respectively, while uncorrected temperature measurements had a mean bias error and mean absolute bias error of -0.41°C and 1.92°C, respectively. The cameras were deployed on the south-facing sides of trees to maximize potential bias, meaning that cameras deployed on more shaded sides of trees would likely record even more accurate temperature measurements than the cameras in our study. However, Hofmeester et al. (2020) found their cameras overestimated temperatures by 1.9°C on average, even though their cameras were deployed on the north-facing sides of trees. Air temperature can vary considerably in space, particularly in complex terrain (Holden et al. 2011). It is possible their cameras were experiencing different true air temperatures than were being recorded at the weather station used for comparison. Our use of a weather station in proximity to the cameras allowed us to have high confidence in the comparisons of true air temperature and the temperatures recorded by the cameras.

If direct measurements of other variables cannot be collected, some values could be estimated from available data sources (Table 2). For example, Flerchinger et al. (2009) summarized and compared several different algorithms for estimating longwave radiation, and Chen et al. (2021) summarized and compared different models of wind speed. Our study was performed with HP2X cameras in the dark green case color, but Reconyx also manufactures cameras with other case colors. Shortwave and longwave albedos of cameras with other case colors warrant further research.

The variable estimates generated by Solver may require further research to estimate more accurately. The value for shortwave absorptivity suggests the cameras are blackbodies, which is highly unlikely. The value for longwave absorptivity (0.87) is also lower than expected of a normal terrestrial object (~ 0.97), though this may be explained by the glass on the face of the camera. The meteorological station collecting longwave radiation data was placed about 30 m from the cameras and with less surrounding vegetation, so it may have experienced lower incoming longwave radiation than was experienced by the cameras. This could have forced Solver to bias the shortwave absorptivity value high and the longwave absorptivity value low to compensate for the additional longwave radiation coming from the surrounding vegetation.

The bare ground reflectivity value is a reasonable value for a mixture of exposed soil and vegetation (Campbell and Norman 1998). Bare ground reflectivity is dependent on the proportions of ground cover composed of exposed soil versus vegetation at a particular camera site, therefore bare ground reflectivity needs to be estimated for each camera site. The snow-covered ground reflectivity is a reasonable average, but this value likely decreased throughout the snow-covered days as the snow aged, leading to lower snow reflectivity, and as snow melted, leading to more exposed bare ground. Better model performance during snow-covered conditions may require an additional view factor for snow.

A potential source of error in our corrected temperature measurements was the longwave emittance values from the surrounding trees and ground. Tree and ground temperature measurements were not taken during the experiment, so we assumed the trees and ground were at the same temperature as the camera. However, the trees and ground, having a larger thermal mass than the cameras, would equilibrate with true air temperature more slowly than the cameras; this would cause the trees and ground to retain more heat and thus emit more longwave radiation than was estimated. Properly accounting for the longwave emittance of the trees and ground would likely reduce overestimations at times of high shortwave radiation.

Though precipitation events and phase were of interest, these had to be abandoned. The main interest in exploring precipitation events with cameras was to determine the occurrence of rain-on-snow events, but rain events were rarely detected even in night images. However, we speculate precipitation events may be more easily determined using videos instead of still images. This idea warrants further exploration.

Conclusions

This is the first formal assessment of the accuracy and error of temperature measurements made by a camera model popular with researchers. We found the HP2X cameras in our study had a mean bias error of -0.41°C and a mean absolute bias error of 1.92°C. We also found 66% and 32% of temperature observations from HP2X cameras were within 2°C and 1°C of true air temperature, respectively. The energy balance model used improved the number of temperature observations within 2°C of true air temperature by 23% and within 1°C of true air temperature by 69%.

While we could not assess the feasibility of collecting precipitation event and phase data with still images, this does not mean cameras cannot collect information about precipitation. Rather, video may be necessary to confidently determine when precipitation events are truly happening instead of other processes such as canopy unloading or wind redistribution of snow.

References

Buchholz, R., Stamn, J., and Neha, S.A. 2021. Can camera traps be used to measure climate change induced alterations of the activity patterns of elusive terrestrial vertebrates? Climate Change Ecology 2:100020.

Campbell, G.S., and Norman, J.M. 1998. *An Introduction to Environmental Biophysics* (2nd edition). Springer-Verlag. New York.

Chen, H., Birkelund, Y., Anfinsen, S.N., Staupe-Delgado, R., and Yuan, F. 2021. Assessing probabilistic modelling for wind speed from numerical weather prediction model and observation in the Arctic. Scientific Reports 11:7613.

Droghini, A., and Boutin, S. 2018. The calm during the storm: Snowfall events decrease the movement rates of grey wolves (*Canis lupus*). PLoS One 13(10):e0205742.

Flerchinger, G.N., Xaio, W., Marks, D., Sauer, T.J., and Yu, Q. 2009. Comparison of algorithms for incoming atmospheric long-wave radiation. Water Resources Research 45:W03423.

Floyd, W., and Weiler, M. 2008. Measuring snow accumulation and ablation dynamics during rain-on-snow events: Innovative measurement techniques. Hydrological Processes 22:4805-4812.

Fylstra, D., Lasdon, L., Watson, J., and Waren, A. 1998. Design and use of the Microsoft Excel Solver. Informs Journal on Applied Analytics 28(5):29-55.

Hofierka, Y., and Śúri, M. 2002. The solar radiation model for Open source GIS: Implementation and applications. Proceedings of the Open source GIS - GRASS users conference 2002 - Trento, Italy, 11-13 September 2002.

Hofmann, G.S., Coelho, I.P., Bastazini, V.A.G., Cordeiro, J.L.P., and de Oliveira, L.F.B. 2016. Implications of climatic seasonality on activity patterns and resource use by sympatric peccaries in northern Pantanal. International Journal of Biometeorology 60:421-433.

Hofmeester, T.R., Young, S., Juthberg, S., Singh, N.J., Widemo, F., Andrén, H., Linnell, J.D.C., and Cromsig, J.P.G.M. 2020. Using by-catch data from wildlife surveys to quantify climatic parameters and timing of phenology for plants and animals using camera traps. Remote Sensing in Ecology and Conservation 6(2):129-140.

Holden, Z.A., Crimmins, M.A., Cushman, S.A., and Littell, J.S. 2011. Empirical modeling of spatial and temporal variation in warm season nocturnal air temperatures in two North Idaho mountain ranges, USA. Agricultural and Forest Meteorology 151:261-269.

Liu, J., Chen, R., Song, Y., Yang, Y., Qing, W., Han, C., and Liu, Z. 2015. Observations of precipitation type using a time-lapse camera in a mountainous region and calculation of the rain/snow proportion based on the critical air temperature. Environmental Earth Sciences 73(4):1545-1554.

Mech, L. D., Smith, D.W., Murphy, K.M., and MacNulty, D.R. 2001. Winter severity and wolf predation on a formerly wolf-free elk herd. Journal of Wildlife Management 65(4):998-1003.

Meter Environment. 2021. ATMOS 41—Correction of air temperature measurements from a radiation-exposed sensor. http://publications.metergroup.com/Sales%20and%20Support/METER%20Environment/Website%20Articles/atmos-41-correction-air-temperature-measurements-radiation-exposed-sensor.pdf.

Microsoft Corporation. 2018. *Microsoft Excel*. Retrieved from https://office.microsoft.com/excel.

R Core Team. 2022. R: A language and environment for statistical computing. R Foundation for Statistical Computing, Vienna, Austria. <https://www.R-project.org/>.

Sirén, A.P.K., Somos-Valenzuela, M., Callahan, C., Kilborn, J.R., Duclos, T., Trager, C., and Morelli, T.L. 2018. Looking beyond wildlife: Using remote cameras to evaluate accuracy of gridded snow data. Remote Sensing in Ecology and Conservation 4(4):375-386.

Steenweg, R., Hebblewhite, M., Kays, R., Ahumada, J., Fisher, J.T., Burton, C., Townsend, S.E., Carbone, C., Rowcliffe, J.M., Whittington, J., Brodie, J., Royle, J.A., Switalski, A., Clevenger, A.P., Heim, N., and Rich, L.N. 2017. Scaling-up camera traps: monitoring the planet’s biodiversity with networks of remote sensors. Frontiers in Ecology and Evolution 15(1):26–34. https://doi.org/10.1002/fee.1448.

Thimonier, A., Sedivy, I., and Schleppi, P. 2010. Estimating leaf area index in different types of mature forest stands in Switzerland: A comparison of methods. European Journal of Forest Research 129:543-562.

Figures and Tables

Table 2. Model covariates for biophysical model to correct Reconyx Hyperfire II camera temperature measurements.

Variable	Description	Value
T_a	Air temperature (°C)	To be calculated
T_{cam}	Camera temperature (°C)	Extracted from images
α_s **	Shortwave absorptivity of the camera (unitless)	1.00
α_L **	Longwave absorptivity of the camera (unitless)	0.868
S_{bd}	Incoming shortwave radiation (W/m^2)	Measured using a pyranometer, calculated using hemispherical photography, or modeled in Geographic Information Systems (Hofierka and Suri 2002)
L_a	Incoming longwave radiation from the sky (W/m^2)	Measured using a pyrgeometer or calculated using algorithms (Flerchinger et al. 2009)
L_s	Incoming longwave radiation from surrounding objects (W/m^2)	Measured using a pyrgeometer or calculated using $\varepsilon_L \sigma T_{cam}^4$, assuming that surrounding objects are at the same temperature as the camera
σ	Stefan-Boltzmann constant ($W/m^2/K^4$)	$5.67 * 10^{-8}$
c_p	Molar specific heat of air (J/mol/°C)	29.3
u	Wind speed (m/s)	Measured using an anemometer, collected from weather data, or modelled (ex. De Rooy and Kok 2004)
F_a	View factor of the sky (unitless)	Calculated using hemispherical photography or approximated using percent canopy cover and (1 – CC) / 2, assuming that the lower hemisphere of the view factor is entirely made up of ground and vegetation
F_s	View factor of surroundings (unitless)	calculated using hemispherical photography or approximated using 1- F_a
ρ_s **	Reflectivity of the surroundings (unitless)	0.230 (bare ground) 0.411 (snow-covered ground)
d	Characteristic dimension of the camera (m)	0.095 (the average of the width and depth of a camera body)

** α_s, α_L, and ρ_s were solved for using Microsoft Excel's Solver functionality. Since the true camera temperature was already known, Solver was used to solve for the values of α_s, α_L, and ρ_s which minimized the sum of squared differences between the actual and predicted camera temperatures.

Fig. 5. Ensemble mean temperatures on an hourly basis recorded by Reconyx Hyperfire II cameras and a weather station (ATMOS 41). Shaded areas are the range of temperatures recorded at that hour.

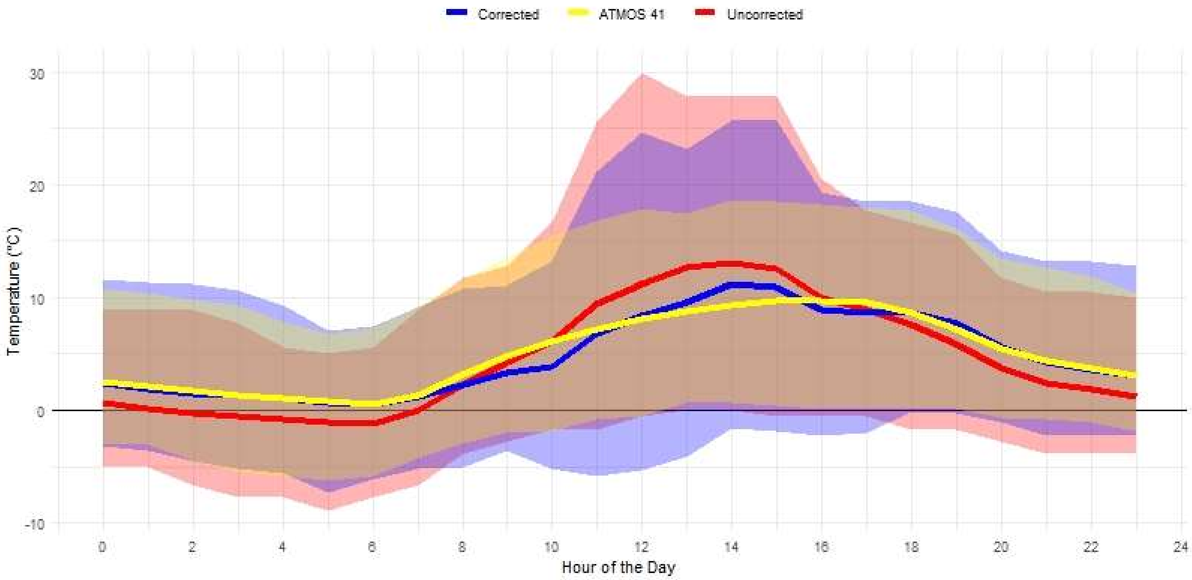

Fig. 6. Bias error of temperature measurements from Reconyx® Hyperfire™ II cameras compared to temperature measurements from an ATMOS 41 weather station (Meter Environment®. Panels are A) bias error versus hour of the day, B) absolute bias error versus hour of the day, C) bias error shortwave radiation, and D) absolute bias error versus shortwave radiation.

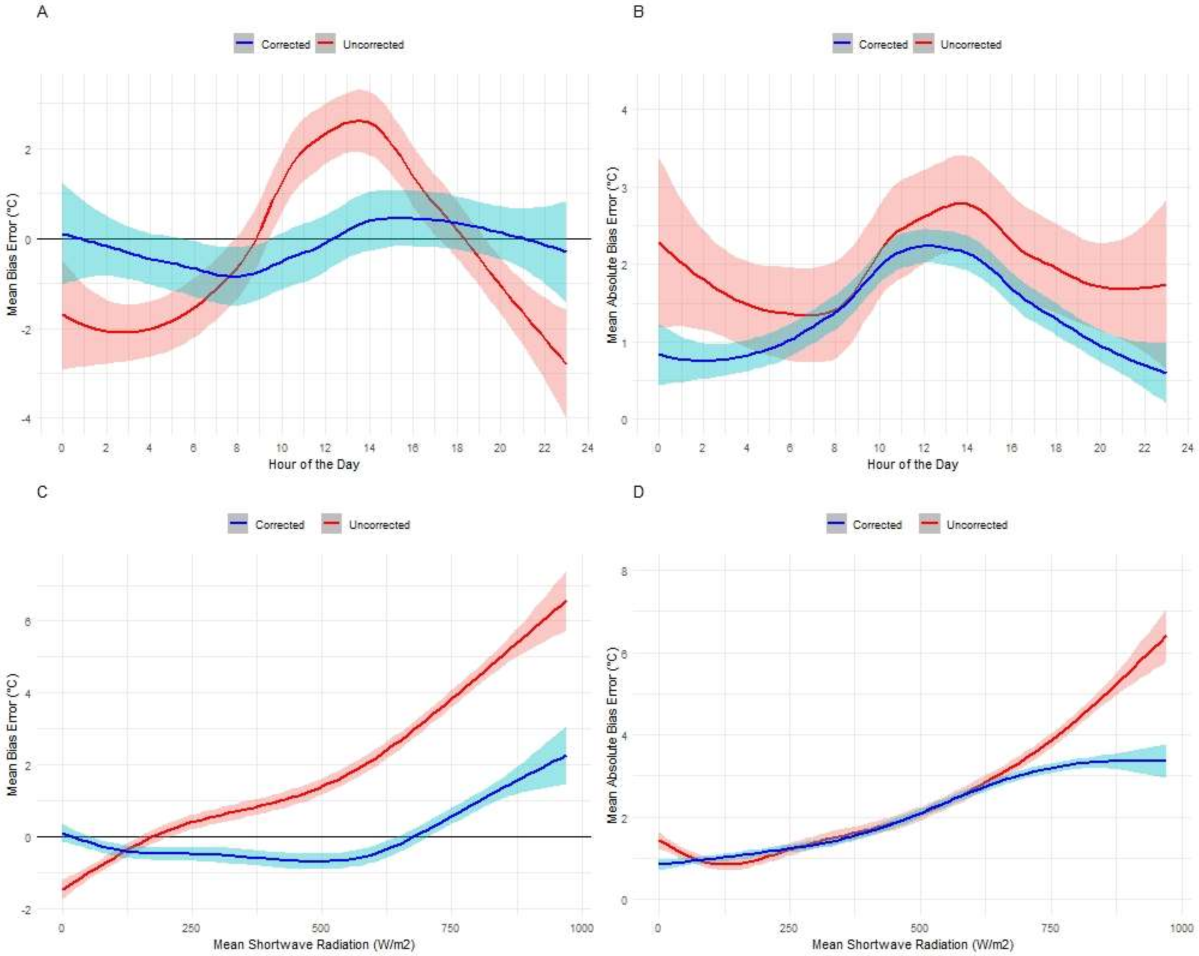

Fig. 7. Root mean squared deviation (RMSD) of temperature measurements from Reconyx® Hyperfire™ II cameras compared to temperature measurements from an ATMOS 41 weather station (Meter Environment®) on an hourly basis.

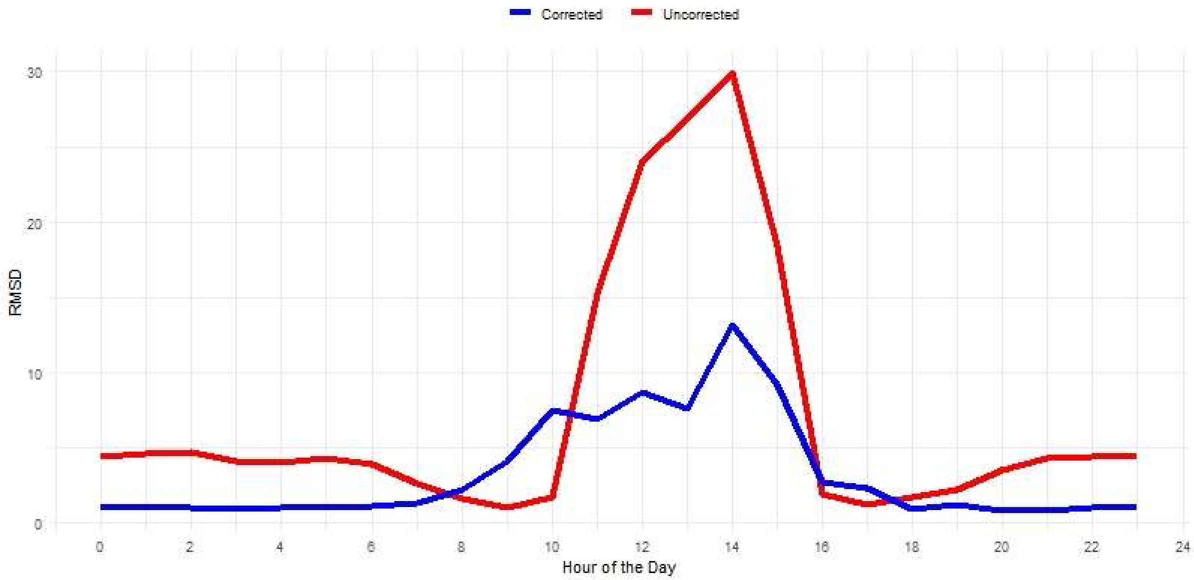

Fig. 8. Error in A) uncorrected and B) corrected temperature measurements made by Reconyx® Hyperfire™ II cameras from March-April 2021. The interval contained in the dashed lines is the snow-covered period, while the intervals outside the dashed lines are bare ground periods. The shaded area indicates temperatures within 2°C.

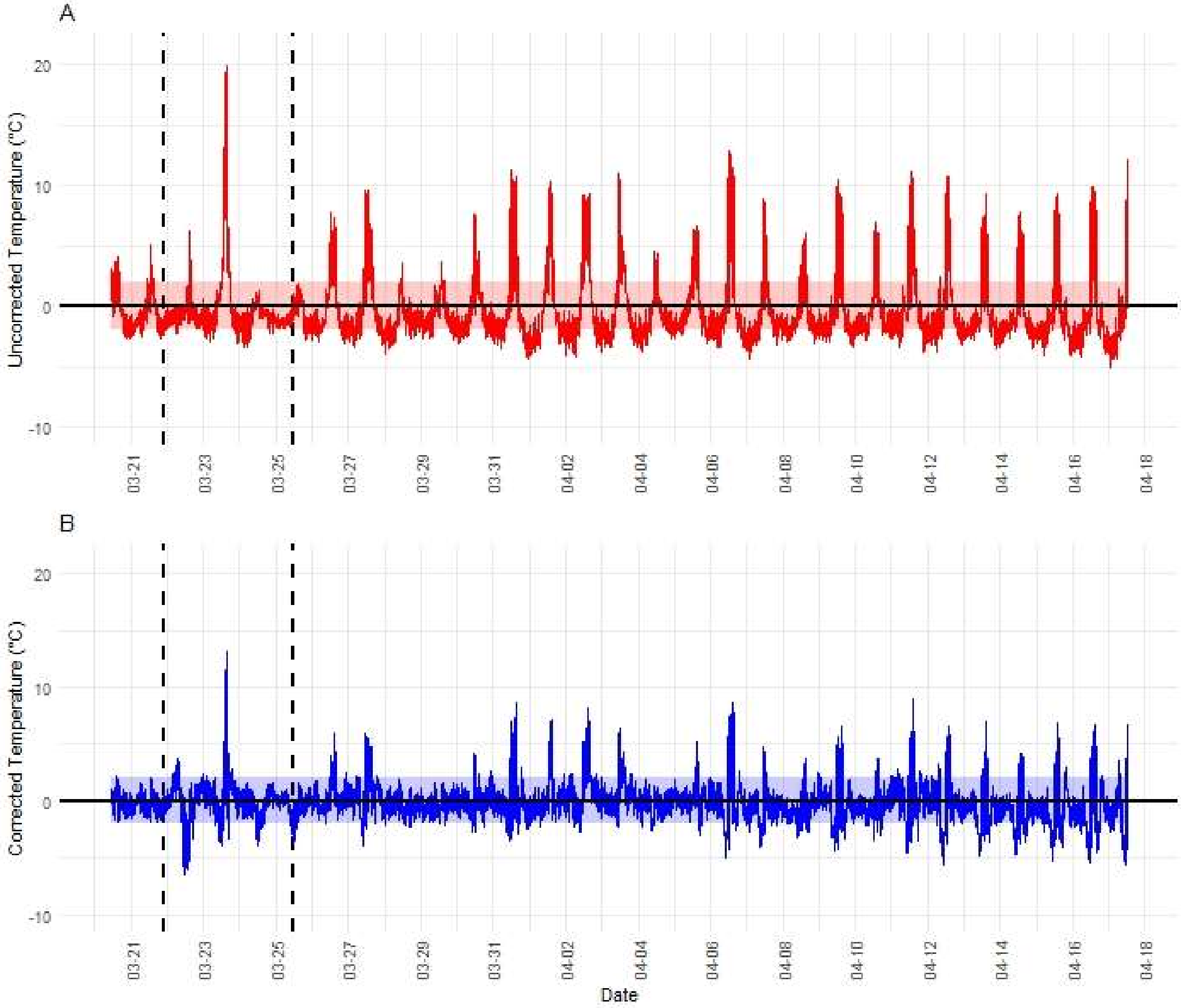

Chapter 2: Identifying Snow Refugia in Complex Forested Terrain Using Camera Data

Abstract

Knowledge of snow cover properties on fine scales is imperative for modeling of hydrologic processes and for habitat management of wildlife species that rely on snow cover. Identification of snow refugia, or places with relatively late snow disappearance dates compared to surrounding areas, are especially important as climate change continues to alter snow cover timing and duration. However, many snow data products are either too coarse scale to capture variations in snow cover, too expensive, or too logistically challenging to collect over broad spatial extents. The purpose of this study was to use remote cameras to collect snow data at fine spatial and temporal scales in a complex forested terrain for the identification of snow refugia. We built generalized linear models to relate the snow disappearance dates (SDDs) at the camera sites to their topographic and vegetation characteristics. We built a model to describe SDDs of camera sites which contained elevation, aspect, and an interaction between canopy cover and cold-air pooling potential. This model could predict SDDs to within 2 weeks and to within 1 week of true SDD for 93% and 71% of the camera sites, respectively. This model used only data which are readily available as spatially distributed datasets, which allowed for mapping of SDDs across the entire study site. This model and map can be used to guide forest management for the retention of snow, increase the accuracy of hydrologic models, and inform habitat management for snow-dependent wildlife species.

Introduction

Snow conditions can vary widely even at fine spatial scales. These fine-scale variations in snow conditions can cause differences in local hydrology, which has cascading effects on vegetation and wildlife. Jost et al. (2007) determined their snow-water equivalent (SWE) measurements, a measure of the amount of liquid water present in a snowpack if it was melted, were no longer spatially dependent on each other at distances even less than 10 or 20 m. Heterogeneity in snow conditions is caused by differences in rates of accumulation, melt, and sublimation (direct phase change from ice to water vapor). Factors affecting these rates include precipitation, temperature, canopy interception, radiation loading, and wind redistribution (Luce et al. 1998, Dickerson-Lange et al. 2017).

Terrain attributes can enhance or diminish the importance of each of these factors in determining local snow conditions. Elevation and rain shadows play a role in precipitation variations in complex terrain (Leung et al. 2003). It has been well established that increasing elevation decreases air temperature, though the exact amount of increase varies by latitude, pressure, and season (Stone and Carlson 1979). Cold-air pooling, the process by which dense, cold air settles into low-lying areas, can cause low-elevation areas and topographic concavities to regularly experience localized temperature inversions (Lundquist et al. 2008, Daly et al. 2010, Curtis et al. 2014). Additionally, the density of canopy cover and the air temperature affect the efficiency of canopy interception (Roth and Nolin 2019) and turbulent transport (Strasser et al. 2008) of snow. While snow may unload from the canopy, some of it sublimates directly from the canopy, causing forests to have lower snow depths than nearby unforested areas (Dickerson-Lange et al. 2017, Jeníček et al 2020). Tree canopies shade direct shortwave radiation (0.28 – 3.5 μm) from reaching the snow surface while simultaneously emitting longwave radiation (3.5 – 100 μm) causing snow immediately around trees to melt more quickly (Dickerson-Lange et al. 2017). Needles, bark, and other debris on the snow surface lower the albedo of the snow (the ability for the snow to reflect incoming radiation) and increase the amount of radiation absorbed by the snow (Hardy et al. 2000, Dickerson-Lange et al. 2017). Slopes and concavities prevent direct shortwave radiation from reaching the snow surface at certain times of the day due to self- and/or adjacent terrain shading (Curtis et al. 2014). Finally, snow redistribution by wind and gravity changes the spatial distribution and depth of snow (Bernhardt et al. 2008, Marshall et al. 2019). These processes can combine synergistically or antagonistically to produce snow conditions that are highly complex even at very fine scales.

Knowledge of the biophysical factors affecting variability in snow cover on fine scales can improve monitoring and modeling of water resources. Because considerable amounts of water are stored as snow in snow-dominated systems, the timing, duration, and magnitude of snowmelt controls spring streamflow dynamics, groundwater recharge, and soil moisture in these watersheds (Jost et al. 2007). Thus, reliable estimation and modeling of the amount of area as well as specific locations covered in snow are crucial for accurate modeling of water resources in these systems. However, using relatively coarse-scale topography, canopy cover, and solar radiation data to drive these models may cause snowmelt dynamics to be improperly modeled. Additionally, remnant patches of snow may be misclassified as snow-free or newly emerging patches of bare ground may be misclassified as snow-covered if they occur at spatial scales smaller than those captured by gridded snow cover data products (Molotch and Margulis 2008). Both issues lead to uncertainty in snow-water equivalent (SWE) estimates derived from hydrologic models. For instance, Molotch and Margulis (2008) found peak SWE estimates from their physically based snow model could be 44-68% lower when the snow-covered area was modeled at 1-km^2 resolution instead of 30-m^2 resolution. Such differences in SWE estimates can radically change estimates of other hydrologic variables such as soil moisture and runoff during the modeling process, which confounds inference and hampers effective decision-making regarding the use of available water resources.

When topographic, vegetation, and hydrometeorological factors at a site create optimal conditions for the retention of snow, this area can be thought of as a “snow refugium.” The concept of climate refugia is a relatively new concept in ecology (Klein et al. 2009). McLaughlin et al. (2017) defined “hydrologic refugia” as areas relatively shielded from high evapotranspiration rates, which allows them to provide soil moisture to local vegetation later in the year. Snowmelt and snow cover were discussed as factors contributing to hydrologic refugia (McLaughlin et al. 2017). Curtis et al. (2014) noted that incorporating cold-air pooling into their projections of April 1st SWE suggested the presence of “climate refugia” for snow-dependent species such as wolverine (*Gulo gulo*). Building on this idea, we define “snow refugia” as areas with later snow cover relative to surrounding areas due to mechanisms including radiation shading, cold air retention, lack of canopy snow interception, and wind redistribution of snow.

Snow refugia will provide critically important habitat for snow-dependent wildlife species as climate change continues to alter snow regimes. Species can be dependent on snow for a variety of reasons including thermal cover, competitive advantage over less snow-adapted species, camouflage, emergence timing, and flowering timing (Steen et al. 1992, Inman et al. 2012, Kudo and Ida 2013, Pozzanghera et al. 2016, Penczykowski et al. 2017, Mills et al. 2018, Goldberg et al. 2020). Many of these species are of conservation concern because climate change is reducing the snow cover and depth they need for reproduction and survival (Kudo and Ito 2013, Curtis et al. 2014). Identification of snow refugia and the landscape characteristics producing snow refugia are thus of utmost importance for conservation of snow-dependent wildlife species in a changing climate.

Current snow data products are limited by their spatial or temporal resolution, cost, and effort, making them insufficient for characterizing snow cover at fine scales and identifying snow refugia. Manual field observations such as snow courses are limited by resource availability and safe accessibility. Snow Telemetry (SNOTEL) stations are often only placed in small canopy gaps and are relatively expensive to establish, limiting their usefulness for monitoring of snow cover variations in areas with heterogenous snow conditions such as in complex forested terrain (but see Molotch and Bales 2006). Satellite- and model-derived snow data products such as Moderate Resolution Imaging Spectroradiometer (MODIS; Hall et al. 2006), Snow Data Assimilation Systems (SNODAS; NSIDC 2004), Advanced Very High Resolution Radiometer (AVHRR; Vermote 2019), and Landsat Enhanced Thematic Mapper Plus (ETM+; USGS EROS Center 2018) can provide snow cover data, but selecting a satellite snow data source is often a tradeoff between spatial and temporal resolution. Spatial resolutions of these data sources range from 30 m^2 for ETM+ to 1 km^2 for SNODAS, while temporal resolutions range from daily for AVHRR and SNODAS to every 16 days for ETM+. Cloud and canopy cover add additional uncertainty to the frequency, spatial extent, and quality of satellite data (Hall and Riggs 2007). SNODAS, being a physically based modeled data product, is also subject to considerable modeling error (Clow et al. 2012, Meromy et al. 2012, Sirén et al 2018). Light Detection and Ranging (LiDAR), structure-from-motion, and other physically based models such as SnowModel (Liston and Elder 2006) can provide incredibly fine-scale information, but the amount of field or computational effort, time, and expertise necessary to derive these data make them less practical for many applications (Deems et al. 2013, Fernandes et al. 2018, Mahoney et al. 2018). Resource managers would therefore benefit from a cost-effective, reliable tool for estimating snow conditions and identifying snow refugia for species of conservation concern, particularly in complex forested terrain undergoing a transition from snow- to rain-dominated precipitation.

Remote cameras are a widely used tool in various natural resources applications. Remote cameras are one of the fastest-growing data collection tools in wildlife science and can be used for numerous applications (Steenweg et al. 2017). Though they have been used less frequently in hydrologic studies, remote cameras have been successfully used to assess bias in SNODAS snow depth estimates (Sirén et al. 2018), measure snow-covered area and snow depth, (Hedrick and Marshall 2014, Giuliani et al. 2016, Pimentel et al. 2015), estimate canopy interception (Garvelmann et al. 2013), validate models of snow albedo (Melloh et al. 2002), and capture rain-on-snow events (Floyd and Weiler 2008).

Remote cameras are a useful and powerful option for monitoring snow cover in complex terrain. Cameras remotely collect data at a much finer spatial resolution (i.e., the viewshed of the camera) than is captured by many other remote data collection methods. Cameras can be programmed to take timelapse images at intervals ranging from days to seconds, allowing for regular monitoring of snow within the camera viewshed. Cameras can be placed anywhere there is a vertical surface to which a camera can be attached. A temperature measurement is also recorded with each image, which is useful for the identification of local freeze-thaw cycles and cold-air pools. Because of their low power requirements, cameras require very little maintenance, and they can be reused for several years of data collection. Cameras can also be programmed to take both motion-triggered and timelapse images, so the capture of images of snow does not interfere with concurrent wildlife data collection. This allows wildlife researchers to co-locate wildlife detections and snow conditions at a site.

The general objective of this research was to improve our understanding of how biophysical conditions contribute to formation of snow refugia at fine scales (~ 30 m^2) in complex forested terrain. We hypothesized a combination of topography, cold-air pooling, vegetation, and hydrometeorological conditions would best explain SDDs and locations on the landscape serving as snow refugia. Our secondary objective was to use only data from cameras, other field data, and readily available elevation and canopy cover datasets to determine these patterns in snow retention. While biophysical models exist which can estimate distributed snow data (Liston and Elder 2006), we sought to determine if data derived from simpler methods would be sufficient to identify snow refugia. To accomplish these objectives, we deployed a stratified network of remote cameras in a complex forested terrain to monitor snow conditions at fine scales and performed regression analysis to determine which site covariates best explained the snow disappearance date (SDDs; the final day with snow cover) at each site. Those areas with the latest SDDs would be considered snow refugia. Identifying the factors facilitating snow retention will inform how forests might be managed to improve availability of late-season snow cover. The resultant model can also be used to map potential locations of snow refugia and pinpoint priority areas of conservation for snow-dependent wildlife species.

Methods

Study Area

The study area for this project is the Palouse Range (hereafter Moscow Mountain) in Latah County, ID (Fig. 9). This field site was chosen because it has a wide variety of both topography and canopy cover in which to sample snow conditions and has a network of 61 trails covering 106 km with reasonable access during the winter months.

Moscow Mountain spans approximately 800 to 1500 m above sea level and is in the rain-snow transition zone of the Northwest United States. The forest cover is comprised of ponderosa pine (*Pinus ponderosa*) and Douglas-fir (*Pseudotsuga menziesii*) forests at low elevations and western red cedar (*Thuja plicata*) and fir (*Abies* sp.) forests at high elevations. The climate is characterized as continental-maritime comprised of generally Mediterranean conditions, with hot, dry summers and mild winters punctuated by periodic intrusions of cold air masses (Hubbart et al. 2007). Moscow Mountain receives an average of approximately 1060 mm of precipitation annually. The mean peak snow-water equivalent (SWE) for Moscow Mountain from water years 2001 – 2021 was 529 mm. In the winter 2020 – 2021 field season, the peak SWE was 594 mm, indicating the field season occurred in a snow year slightly above average. The peak SWE during the pilot field season in winter 2019-2020 was 518 mm, which is an average snow year for Moscow Mountain (USDA 2022).

Camera Data Collection

We deployed 138 camera stations from October 2020 – May 2021. We used Reconyx ® Hyperfire I and Hyperfire II cameras. We programmed the cameras to take one image each hour of the day, including nighttime hours, so each camera recorded at least 24 images every day throughout its deployment. Cameras were retrieved from April – May 2021. Cameras were retrieved when there was no snow in the immediate viewshed of the camera (up to 15 m away depending on the distribution of understory vegetation).

We stratified camera sites by elevation, aspect, and canopy cover. Elevation was classified from <925 m, 925-1,050 m, 1,050-1,175 m, 1,175-1,300 m, and >1,300 m; aspect was classified as N, S, E, or W; and canopy cover was classified as "sparse" for canopy covers <35%, "moderate" for canopy covers between 35-75%, and "dense" for canopy covers >75%. We took canopy cover measurements using a densiometer. We quasi-randomly selected sites within each strata to permit reasonable access via existing trail and forest road networks. However, trails themselves were not sampled because foot and vehicle traffic changes the depth and properties of the snow, so snow retention may be different on roads than it is in adjacent forest. After all strata were sampled, we placed additional cameras in landscape concavities and canopy gaps which are expected to retain snow later in the year (Lawler and Link 2011, Curtis et al. 2014). We also placed cameras at least 20 m away from other cameras given that snow conditions in complex terrains are often not correlated beyond this distance (Jost et al. 2007).

On the deployment date, we recorded the height and direction of the camera and the latitude, longitude, and elevation. We mounted and locked cameras onto trees at a height of 2–3 m to prevent snow from blocking the cameras. During camera deployment, we took reference images for superimposing a "virtual" snow stake (VSS) onto images to measure snow depth (Strickfaden et al., *in review*). We placed a reference snow stake with 2- and 10-cm gradations at 5, 10, and 15 m within the viewshed of the camera, and we allowed the camera to take motion-triggered images. We took an additional set of reference images on camera retrieval to account for potential changes in the camera's viewshed during its deployment. VSSs were then superimposed onto images using functions in the *edger* package (Strickfaden et al., *in review*). At a subset of cameras, we also installed a physical snow stake 5-15 m from the camera which was composed of a 183 cm U-post driven into the ground and a 152cm section of PVC pipe. These were used to verify measurements taken with the VSSs. We marked the white PVC pipe every 2 cm with black permanent marker and every 10 cm with brightly colored electrical tape. We then fixed a pipe to a U-post with cable ties. We maintained cameras throughout the season, coincident with snow density and hardness measurements, to change batteries, ensure proper function, and remove obstructing vegetation.

We placed an external LogTag ® TRIX 8 temperature recorder (hereafter 'LogTag') at each camera station. We programmed the LogTags to record temperatures at 45-minute intervals. The LogTags were housed inside of plastic protective coverings and radiation shields. Each radiation shield was comprised of 15 cm of PVC pipe covered in aluminum foil tape to reflect shortwave radiation and reduce longwave radiation loading. We drilled holes into the radiation shields to allow for increased air flow (Terando et al. 2017). We hung the LogTag in its housing at the same height as the camera on the north side of trees or under canopy cover to minimize the potential impacts of direct shortwave radiation. If no branches meeting these criteria were available on the camera tree, we hung it on a nearby tree.

Hemispherical Photography

To quantify vegetation cover and estimate incoming shortwave radiation, we took hemispherical photographs at each camera site. We used a Canon™ EOS 70D SLR camera with a Sigma 8mm circular fisheye lens. We took hemispherical photographs on days with little to no wind or precipitation and early in the morning (5AM – 7AM), late in the evening (7PM – 9PM), or on overcast days to maximize the contrast between sky and vegetation. We took photographs in June - July 2021, but nine camera sites were re-photographed in October 2021 due to poor quality of initial photographs. Overstory deciduous vegetation is rare at my study site, so summer changes in canopy cover are negligible.

At each camera site, we placed the DSLR camera with attached lens on a tripod 5 m into the camera viewshed and levelled it to point directly up into the canopy. We took photographs at a variety of exposures and manually selected the photograph with the best exposure for each camera site. We analyzed the best image from each location using Hemisfer software (Thimonier et al. 2010). We manually selected threshold values for distinguishing sky pixels from vegetation pixels for each image. Hemisfer then classifies sky and vegetation pixels in the photograph using this threshold, overlays a solar path onto photographs based on input georeferencing information and photograph orientation, and calculates hourly direct and diffuse shortwave radiation throughout time assuming 50% cloud cover. Hemisfer also outputs a count of sky and vegetation pixels in the image which we used to calculate the percent vegetation cover. Because the 180° image captures some understory vegetation in addition to the overstory vegetation, this value is different from the percent canopy cover value obtained using the densiometer.

Cold-air Pooling Model

To identify potential cold-air pools (CAPs), we developed a novel procedure which we adapted from methods used by Ashcroft and Gollan (2012). LiDAR flights were conducted on Moscow Mountain in 2009 from which a 1-m resolution DEM was created (Bright et al. 2019). This raster product was used to calculate log flow accumulation and relative elevation of each pixel. Ashcroft and Gollan (2012) also assessed distance to water, but few major water features are located on Moscow Mountain, and the few existing ones are captured well using the described procedure, so this was not included as a separate covariate. First, we calculated flow accumulation using the Hydrology tools in ArcGIS (ESRI). Though these tools are intended for water flow calculations, air, which is also a fluid, flows similarly to water. We took the natural log of the flow accumulation plus 1 because some pixels have a flow accumulation of 0. Second, we calculated relative elevation by determining the elevation of the lowest-elevation pixel within a 25, 50, and 100 m radius from each pixel. We subtracted the elevation of a particular pixel from the elevation of the lowest pixel in the focal radius to determine that pixel's relative elevation. We rescaled both the log flow accumulation and relative elevation rasters from 0-1.

Finally, we subtracted the log flow accumulation raster from the relative elevation rasters calculated at different focal radii. Negative differences indicate pixels had both high log flow accumulation and low relative elevation in that neighborhood, which together contribute to potential accumulation of cold air. Therefore, if the difference between the two values was negative, we assigned the pixel a value of 1 (CAP pixel), and if it was positive, we assigned it a value of 0 (non-CAP pixel). The 25-m, 50-m, and 100-m layers were finally merged into a single layer to indicate if a pixel was identified as a potential CAP in any of the three neighborhoods.

We assessed the accuracy of this layer by analyzing monthly minimum and maximum temperatures at air temperature monitoring stations (Maxim Integrated iButtons in radiation shields) distributed across Moscow Mountain from 2009-2011 (J. Abatzoglou, unpubl. data). After accounting for elevation, aspect, and canopy cover, iButtons in CAP pixels had lower minimum temperatures by 1°C and lower maximum temperatures by 3.5°C on average than iButtons not in CAP pixels, which suggests this layer adequately identified CAP pixels. Thus, this layer was used to classify whether a camera site was in a CAP.

Camera Data Processing

We manually recorded snow presence and snow depth in each image. We measured snow depth using any VSSs and physical snow stakes present in images. Snow depths sometimes exceeded 150 cm, which was the height of the snow stakes; if snow depth exceeded 150 cm, snow depth was recorded as "150+" until snow depth could be measured again. The SDD for a camera was defined as the first day on which there was no snow cover in the immediate viewshed of the camera. The SDD determined from the images was considered the true SDD for the site. Though some cameras had larger viewsheds than 15 m, the elevation and canopy cover further into the viewshed may have been substantially different than the elevation and canopy cover at the camera site; to limit bias, we only assessed snow presence within the distance of the furthest VSS, which could be up to 15 m into the camera viewshed. For those cameras which still had small amounts of snow at retrieval, SDD was defined as the day of camera retrieval. Snow events after the persistent snow cover at the camera site disappeared were not counted towards the SDD. We processed images using Timelapse2 software (Greenberg 2020).

Data Analysis

We built a suite of generalized linear models (GLMs) to predict the SDD in Julian days. Model predictors included elevation (classification or value in meters); slope (degrees); aspect (cardinal direction or degree); canopy or vegetation cover (classification or percent); CAP potential (indicator); mean daytime shortwave radiation (Watts/m^2); mean temperature in December, January, and February (mean DJF temperature) from the LogTag (°C); and mean snow depth (value in cm). Maximum snow depth was not included because snow depth could not be measured at depths >150 cm with the snow stakes used. Snow-water equivalent (SWE) would also be a useful metric to test, but this would require modeling of SWE which is beyond the scope of this research.

We recognized some variables might make the resultant model less accessible to most researchers. Fine-scale temperature and snow depth data are rarely available for determining mean DJF temperature and mean snow depth, and the percent vegetation cover covariate must be collected using hemispherical photography. Thus, we decided to run an additional suite of models excluding mean DJF temperature, mean snow depth, and vegetation cover as potential covariates to determine if a comparable model could be built using only data which are more readily available or easy to derive. Models containing the limited pool of variables will be referred to as "data-constrained," while the other models will be referred to as "data-rich."

Combinations of the predictors and interactions between them were tested, and the best-fit model for each data pool was selected using Akaike's Information Criterion for small sample sizes (AICc; Hurvich and Tsai 1989) and the MuMIn package (Barton 2022) in program R (R Core Team 2021). Models were additionally tested on data from a pilot season conducted during winter 2020 at the same study site. We deployed 17 cameras in January 2020 using the same deployment protocol as in the 2020-2021 field season, and the SDD was determined for each camera.

Results

Data from 134 of the 138 cameras deployed in 2020-2021 were used. One camera was stolen, and two cameras malfunctioned so images were not captured on or near their SDDs. A fourth camera did not have a functioning LogTag accompanying it, so it was also excluded. A total of 562,000 timelapse images were captured by the remaining 134 cameras. Though snow depth could only be measured up to 150 cm from images, snow depths of up to 203 cm were recorded during concurrent snow density and hardness sampling (Chapter 3). SDDs in 2021 ranged from 18 March – 26 May and in the 2020 pilot season ranged from 11 March – 25 May.

The data-rich GLM to predict SDD with the most support included cardinal aspect (i.e., N, E, S, or W), percent vegetation cover, and an interaction between mean DJF temperature and mean snow depth (Table 3, Fig. 10). The best-fit model could predict 2021 SDDs to within 2 weeks and to within 1 week of the true SDD for 98% and 74% of the camera sites, respectively (Fig. 11). For each 0.09°C decrease in mean DJF temperature

(95% CI: [0.07, 0.13]), SDD was predicted to increase by 1 day. For each 3 cm increase in mean snow depth (95% CI: [2.1, 4.6]), SDD was predicted to increase by 1 day. Increasing DJF temperatures had a much greater effect on SDDs in areas with shallow snowpack than in areas with deeper snowpack (see Fig. 10A). Sites on west-facing aspects had the earliest SDDs, with south-facing aspects 1.4 days later (95% CI: [-1.8, 4.5]), east-facing aspects 3.6 days later (95% CI: [0.4, 6.8]), and north-facing aspects 6.1 days later (95% CI: [2.8, 9.4]) than west-facing aspects. Finally, for each 8% increase in vegetation cover (95% CI: [5.5, 15.6]), SDD was predicted to increase by 1 day (Table 4). Modeled SDDs in 2020 were within 2 weeks and within 1 week of true SDD for 88% and 59% of cameras, respectively.

The data-constrained GLM with the most support contained elevation, cardinal aspect, and an interaction between percent canopy cover and CAP potential (Fig. 12, Table 5). This model could predict 2021 SDDs to within 2 weeks and to within 1 week of the true SDD for 93% and 71% of the camera sites, respectively (Fig. 13). For each 20 m increase in elevation (95% CI: [17.1, 22.6]), SDD was predicted to increase by 1 day. Sites on west-facing aspects had the earliest SDDs, with south-facing aspects 2.5 days later (95% CI: [-1.3, 6.3]), east-facing aspects 6.9 days later (95% CI: [3.0, 10.9]), and north-facing aspects 11.4 days later (95% CI: [7.5, 15.3]) than west-facing aspects. For sites not in CAP pixels, each 10% increase in canopy cover (95% CI: [6.6, 18.8]) was predicted to increase SDD by 1 day, while for sites in CAP pixels, it was a 4% increase (95% CI: [4.0, 72.9]; Table 6). Modeled SDDs in the 2020 data were within 2 weeks and within 1 week of true SDD for 71% and 41% of cameras, respectively. A considerable advantage of the constrained model is the data required by this model are readily available as spatially distributed datasets, which allows for the extension of this model beyond the camera sites to map SDDs across the entirety of our study area (Fig. 14). Mapping of SDDs identified isolated areas with later SDDs than their surroundings.

Discussion

We built a model using elevation, aspect, canopy cover, and CAP potential to predict the locations of snow refugia at small spatial extents (~ 30 m^2) with very little loss in performance compared to a more complex and data-intensive model. In fact, both models tended to underestimate the SDDs of the camera sites with the latest actual SDDs, meaning these sites are serving as even later-season snow refugia than are being predicted by the models. Thus, these are conservative estimates of snow refugia in our study area. The predictive accuracy of the best-fit data-constrained model for the pilot season data was lower than the best-fit data-rich model, likely because it did not account for the higher temperatures and lower snowfalls in winter 2019-2020. Scaling the predictions from 0-1 (i.e., interpreting the predictions as relative earliest to latest SDDs) may make the predictions more robust to annual temperature and precipitation differences. This is reasonable because the biophysical processes underlying differences in SDD with elevation, aspect, and cold-air pooling are unlikely to change due to climate change (i.e., high elevations, north aspects, and CAPs are still expected to have the latest SDDs regardless of climate change).

However, associations between canopy cover and SDD may change if certain temperature thresholds are exceeded because of climate change. Lundquist et al. (2013) found locations with mean DJF temperatures <-6°C would have later SDDs under canopies than in the open, while climates with mean DJF temperatures >-1°C would have earlier SDDs under canopies. In cold climates, shortwave radiation is the dominant cause of midwinter melt events, while in warm climates, longwave radiation emission by vegetation is the dominant cause of midwinter melt events (Lundquist et al. 2013). Additionally, warmer air temperatures can cause snow to adhere to the forest canopy more efficiently. Assuming it is not warm enough for snow to immediately unload from the canopy, this reduces accumulation under the canopy and allows for more sublimation from the canopy (Lundquist et al. 2013, Roth and Nolin 2019). This suggests that as mean temperatures increase, denser forest cover will be detrimental to snow retention. Both best-fit models predicted denser vegetation cover promoted snow retention in our study site. However, the mean DJF temperatures at the Moscow Mountain SNOTEL station were -1.3°C in 2019-2020 and -2.0°C in 2020-2021, which are approaching the threshold for midwinter melt events on Moscow Mountain to become longwave radiation-dominated. As climate change continues to increase mean temperatures on Moscow Mountain, SDDs may need to be reevaluated to determine if patterns of SDD with canopy cover have shifted.

Climate change is also increasing forest disturbance due to fire and insect outbreaks. Disturbances can reduce canopy cover and canopy density, which would affect canopy interception rates (Teich et al. 2019), shortwave and longwave radiation loading (Schwartz et al. 2021), and surface albedo (Zhang and Liang 2014). Teich et al. (2019) found little difference in variability in snow stratigraphy for intact forest versus forest recently disturbed by insects and attributed this to the continued presence of small twigs in the disturbed stand. Salvage-logged forests, conversely, had much more homogenous snow stratigraphy. This suggests larger disturbances have a greater effect on snow conditions. Canopy cover layers used to run our model for a particular study area should be current to ensure the model accurately reflects canopy conditions.

Additionally, increased mean temperatures and lower snowfall may increase snow ephemerality. Ephemeral snow cover is snow cover persisting for <60 consecutive days, though areas with ephemeral snow cover may still experience several snow-covered periods throughout the winter (Petersky et al. 2019). Sites with ephemeral snow cover have very similar SDDs (Dickerson-Lange et al. 2015). Four low-elevation cameras had SDDs which were considerably earlier than either model predicted and were very similar to each other (see Figs. 11 and 13). At many times, these cameras had very little snow cover, but because of how SDD was defined in this study (all snow had to be melted within the first 15 m of the camera viewshed), these four cameras were classified as having snow present for >60 consecutive days. However, these characteristics indicated these sites had snow cover that was more ephemeral. This likely caused the poor prediction of SDDs at these sites. While ephemeral snow cover was not the focus of this study or the resulting models, remote cameras are a promising tool for capturing the spatial and temporal complexity of ephemeral snow covers. Further, methods exist to extract snow-covered area data from images (Giuliani et al. 2016, Pimentel et al. 2015), meaning snow cover can be quantified at even finer scales than used in this study.

The data-rich model could provide spatially distributed estimates of SDD if mean DJF temperatures and snow depths can be estimated across the area of interest. This may not require biophysical modeling of temperature and snow depth; rather, these values can be forecast on a broad scale from historical data and available satellite- and model-based data products for the year of interest. The actual SDDs predicted may be more informative for management than the relative SDDs used when predicting with the data-constrained model, provided the forecasted mean DJF temperatures and snow depths are reasonably accurate.

Importantly, we did not quantify the effects of small canopy gaps (1-3 tree heights in diameter) on snow retention. Small canopy gaps have a unique canopy structure that creates a distinct radiative environment compared to open or contiguous forest (Lawler and Link 2011). South sides of small canopy gaps block direct shortwave radiation without providing the enhanced longwave radiation emission common in closed canopies, allowing south sides of canopy gaps to be local all-wave radiation minima. Conversely, north sides of canopy gaps are all-wave radiation maxima for the opposite reasons, as they often receive a large amount of direct shortwave radiation plus enhanced longwave radiation from the sunlit trees (Lawler and Link 2011, Seyednasrollah and Kumar 2014, Sun et al. 2018). Bradshaw and Spies (1992) used 2-D wavelet analysis to identify gaps in the canopy structure, while Falkowski et al. (2014) used 2-D wavelet analysis to determine both the height and diameter of tree crowns. The effect canopy gaps have on snow is the result of the width of the gap in relation to the height of the trees on the edges of the gap; combining their two methods (i.e., using a Mexican hat wavelet to determine the height and diameter of canopy gaps) may provide a means by which canopy gaps important to snow retention can be identified.

Wind redistribution of snow was also not explicitly quantified in this study. Estimation of wind redistribution of snow requires complex biophysical modeling (e.g., Mott and Lehning 2010). The goal of this study was to determine and predict SDDs across my study area using only camera data along with readily available terrain data, and wind modeling falls outside of this goal. However, the effect of wind redistribution is indirectly accounted for in the best-fit data-rich model through mean snow depth, as areas affected by wind redistribution would have shallower or deeper snowpacks dependent on if snow is moved to or away from those areas.

While we examined outliers to search for potential causes of modeling errors, we found no obvious explanations. Snow ephemerality, canopy gaps, snow drifting by wind, or combinations of processes, as have already been discussed, may have played roles in the discrepancies. Edge habitats, much like canopy gaps, have unique snow processes and dynamics (Webb et al. 2020). Though we attempted to not place cameras in obvious edge habitats, the effects of edges can extend up to 44 m into the forest (Webb et al. 2020). We did not explicitly account for edge effects, but they may have introduced some error in model predictions.

Conclusions

Snow data are often only available at relatively broad spatial resolutions (e.g., $\geq$500 m^2), leading to spurious estimates of snow cover in complex forested terrain and a poor understanding of the availability of snow refugia for snow-dependent wildlife. For example, in our study area, a group of cameras contained within a 500 m^2 grid cell could have SDDs >1 month apart. This immense complexity is difficult to capture because satellites can misclassify snow under canopy cover while other methods are expensive and logistically challenging. Therefore, key processes dictating snow retention in complex terrain are lost. Conversely, by using remote cameras, we quantified SDDs at fine spatial and temporal scales with certainty because we have a literal snapshot of snow conditions in a complex terrain. We built a relatively simple model which predicted those SDDs to within 2 weeks of truth in 93% of camera sites and to within 1 week of truth in 71% of camera sites.

This model can be used to estimate the area and extent of snow cover available throughout the winter, which is useful for management of both water resources and wildlife. For water resources management, finer-scale knowledge of snow cover can improve model estimates of SWE, leading to better estimates of water availability for several hydrologic processes including soil moisture and runoff (Molotch and Margulis 2008). For wildlife management, identifying the locations of snow refugia can provide insight into the amount of available late-season habitat for snow-dependent species, which will become increasingly important as these species' ranges continue to contract due to climate change (Curtis et al. 2014). Further, forest management practices can be guided towards retaining snow in light of this research. For example, high elevation, north-facing slopes experiencing cold-air pooling can be managed for the optimal amount of forest cover dependent on the dominant radiative processes (i.e., denser cover in colder environments and sparser cover in warmer environments).

Remote cameras are already widely used in the natural resources field. Determining the SDD of a camera is simple, as it only requires noting the date on which all snow at a camera site melted out. This date, along with site data which are commonly recorded during camera deployment no matter the study objectives, allows for mapping of SDDs across an entire study with little additional field effort. This is particularly beneficial in areas where snow data are rarely or never measured. The presented models are most appropriate for complex forested terrain, particularly in the rain-snow transition zone of the Pacific Northwest. SDDs in areas with very simple terrain, considerable wind redistribution of snow, or ephemeral snow cover may not be adequately predicted.

References

Ashcroft, M.B., and J.R. Gollan. 2012. Fine-resolution (25 m) topoclimatic grids of near-surface (5 cm) extreme temperatures and humidities across various habitats in a large (200 x 300 km) and diverse region. International Journal of Climatology 32(14): 2134-2148.

Barton, K. 2022. MuMIn: Multi-model inference. R package version 1.46.0. https://CRAN.R-project.org/package=MuMIn.

Bernhardt, M., Schulz, K., Liston, G.E., and Zängl, G. 2012. The influence of lateral snow redistribution processes on snow melt and sublimation in alpine regions. Journal of Hydrology 424-425:196-206.

Bradshaw, G.A., and Spies, T.A. 1992. Characterizing canopy gap structure in forests using wavelet analysis. Journal of Ecology 80(2):205-215.

Bright, B.C. Hudak, A.T., and McCarley, T.R. 2019. Digital surface, terrain, and canopy height models for Moscow Mountain in 2009. Fort Collins, CO: Forest Service Research Data Archive. https://doi.org/10.2737/RDS-2019-0045.

Clow, D.W., Nanus, L., Verdin, K.L., and Schmidt, J. 2012. Evaluation of SNODAS snow depth and snow water equivalent estimates for the Colorado Rocky Mountains, USA. Hydrological Processes 26:2583-2591.

Curtis, J.A., Flint, L.E., Flint, A.L., Lundquist, J.D., Hudgens, B., Boydston, E.E., and Young, J.K. 2014. Incorporating cold-air pooling into downscaled climate models increases potential refugia for snow-dependent species within the Sierra Nevada ecoregion, CA. PLoS ONE 9(9): e106984. doi:10.1371/journal.pone.0106984.

Daly, C., Conklin, D.R., and Unsworth, M.H. 2010. Local atmospheric decoupling in complex topography alters climate change impacts. International Journal of Climatology 30:1857–1864.

Deems, J.S., Painter, T.H., and Finnegan, D.C. 2013. Lidar measurement of snow depth: a review. Journal of Glaciology 59(215):467-479.

Dickerson-Lange, S.E., Lutz, J.A., Martin, K.A., Raleigh, M.S., Gersonde, R., and Lundquist, J.D. 2015. Evaluating observational methods to quantify snow duration under diverse forest canopies. Water Resources Research 51:1203:1224.

Dickerson-Lange, S.E., Gersonde, R.F., Hubbart, J.A., Link, T.E., Nolin, A.W., Perry, G.H., Roth, T.R., Wayand, N.E., and Lundquist, J.D. 2017. Snow disappearance timing is dominated by forest effects on snow accumulation in warm winter climates of the Pacific Northwest, United States. Hydrological Processes 31:1846-1862.

ESRI. 2011. ArcGIS Desktop: Release 10. Redlands, CA: Environmental Systems Research Institute.

Falkowski, M.J., Evans, J.S., Martinuzzi, S., Gessler, P.E., and Hudak, A.T. 2009. Characterizing forest succession with lidar data: An evaluation for the Inland Northwest, USA. Remote Sensing of Environment 113:946–956.

Fernandez, R., Prevost, C., Canisius, F., Leblanc, S.G., Maloley, M., Oakes, S., Holman, K., and Knudby, A. 2018. Monitoring snow depth change across a range of landscapes with ephemeral snowpacks using structure from motion applied to lightweight unmanned aerial vehicle videos. Cryosphere 12:3535:3550.

Floyd, W., and Weiler, M. 2008. Measuring snow accumulation and ablation dynamics during rain-on-snow events: Innovative measurement techniques. Hydrological Processes 22:4805-4812.

Garvelmann, J., Phol, S., and Weiler, M. 2013. From observation to the quantification of snow processes with a time-lapse camera network. Hydrology and Earth System Sciences 17:1415-1429.

Giuliani, M., Castelletti, A., Fedorov, R., and Fraternali, P. 2016. Using crowdsourced web content for informing water systems operations in snow-dominated catchments. Hydrology and Earth System Sciences 20:5049-5062.

Goldberg, A.R., Conway, C.J., Mack, D.E., and Burak, G. 2020. Winter versus summer habitat selection in a threatened ground squirrel. Journal of Wildlife Management 84(8):1548-1559.

Greenberg, S. 2020. The Timelapse user guide version 2.2.3.6. http://saul.cpsc.ucalgary.ca/timelapse/pmwiki.php?n=Main.Userguide.

Hall, D.K., Riggs, G.A., and Salomonson, V.V. 2006. MODIS/Terra Snow Cover 5-Min L2 Swath 500m. Version 5. Boulder, Colorado USA: NASA National Snow and Ice Data Center Distributed Active Archive Center.

Hall, D.K. and Riggs, G.A. 2007. Accuracy assessment of the MODIS snow products. Hydrological Processes 21:1534-1547.

Hardy, J.P., Melloh, R., Robinson, P., and Jordan, R. 2004. Incorporating effects of forest litter in a snow process model. Hydrological Processes 14:3227-3237.

Hedrick, A.R. and Marshall, H.P. 2014. Automated snow depth measurements in avalanche terrain using time-lapse photography. 2014 International Snow Science Workshop.

Hubbart, J.A., Link, T.E., Gravelle, J.A., and Elliot, W.J. 2007. Timber harvest impacts on water yield in the continental/maritime hydroclimatic region of the United States. Forest Science 53(2):169-180.

Hurvich, C.M and Tsai, C. 1989. Regression and time series model selection in small samples. Biometrika 76(2):297-307.

Inman, R.M., Magoun, A.J., Persson, J., and Mattisson, J. 2012. The wolverine’s niche: Linking reproductive chronology, caching, competition, and climate. Journal of Mammalogy 93(3):634-644.

Jeniček, M., Hotovy, O., and Matejka, O. 2020. Snow accumulation and ablation in different canopy structures at a plot scale: Using degree-day approach and measured shortwave radiation. Acta Universitatis Carolinae Geographica 52(1):61–72.

Jost, G., Weiler, M., Gluns, D.R., and Alila, Y. 2007. The influence of forest and topography on snow accumulation and melt at the watershed-scale. Journal of Hydrology 347:101-115.

Klein, C., Wilson, K., Watts, M., Stein, J., Berry, S., Carwardine, J., Smith, M.S., Mackey, B., and Possingham, H. 2009. Incorporating ecological and evolutionary processes into continental-scale conservation planning. Ecological Applications 19(1):206-217.

Kudo, G. and Ida, T.Y. 2013. Early onset of spring increases the phenological mismatch between plants and pollinators. Ecology 94(10):2311-2320.

Lawler, R.R. and Link, T.E. 2011. Quantification of incoming all-wave radiation in discontinuous forest canopies with application to snowmelt prediction. Hydrological Processes 25:3322-3331.

Leung, L.R., Qian, Y., and Bian, X. 2003. Hydroclimate of the western United States based on observations and regional climate simulation of 1981–2000. Part I: Seasonal statistics. Journal of Climate 16:1892-1911.

Liston, G.E. and Elder, K. 2006. A distributed snow-evolution modeling system (SnowModel). Journal of Hydrometeorology 7:1259-1276.

Luce, C.H., Tarboton, D.G., and Cooler, K.R. 1998. The influence of the spatial distribution of snow on basin-averaged snowmelt. Hydrological Processes 12:1671-1683.

Lundquist, J.D., Pepin, N., and Rochford, C. 2008. Automated algorithm for mapping regions of cold-air pooling in complex terrain. Journal of Geophysical Research 113: D22107.

Lundquist, J.D., Dickerson-Lange, S.D., Lutz, J.A., and Cristea, N.C. 2013. Lower forest density enhances snow retention in regions with warmer winters: A global framework developed from plot-scale observations and modeling. Water Resources Research 49:6356-6370.

Mahoney, P.J., Liston, G.E., Lapoint, S., Gurarie, E., Mangipane, B., Wells, A.G., Brinkman, T.J., Eitel, J.U.H., Hebblewhite, M., Nolin, A.W., Boelman, N., and Prugh, L.R. 2018. Navigating snowscapes: Scale-dependent responses of mountain sheep to snowpack properties. Ecological Applications 28(7):1715–1729.

Marshall, A.M., Link, T.E., Abatzoglou, J.T., Flerchinger, G.N., Marks, G.D., and Tedrow, L. 2019. Warming alters hydrologic heterogeneity: Simulated climate sensitivity of hydrology-based microrefugia in the snow-to-rain transition zone. Water Resources Research 55:2212-2141.

McLaughlin, B.C., Ackerly, D.D., Klos, P.Z., Natali, J., Dawson, T.E., and Thompson, S.E. 2017. Hydrologic refugia, plants, and climate change. Global Change Biology 23:2941-2961.

Melloh, R.A., Hardy, J.P., Bailey, R.N., and Hall, T.J. 2002. An efficient snow albedo model for the open and sub-canopy. Hydrological Processes 16:3571-3584.

Meromy, L., Molotch, N.P., Link, T.E., Fassnacht, S.R., and Rice, R. 2012. Subgrid variability of snow water equivalent at operational snow stations in the western USA. Hydrological Processes 27:2383-2400.

Mills, L.S., Bragina, E.V., Kumar, A.V., Zimova, M., Lafferty, D.J.R., Feltner, J., Davis, B.M., Hackländer, K., Alves, P.C., Good, J.M., Melo-Ferreira, J., Diez, A., Abramov, A.V., Lopatina, N., and Fay, K. 2018. Winter color polymorphisms identify global hot spots for evolutionary rescue from climate change. Science 359:1033-1036.

Molotch, N.P. and Bales, R.C. 2006. SNOTEL representativeness in the Rio Grande headwaters on the basis of physiographics and remotely sensed snow cover persistence. Hydrological Processes 20:723-739.

Molotch, N.P. and Margulis S.A. 2008. Estimating the distribution of snow water equivalent using remotely sensed snow cover data and a spatially distributed snowmelt model: A multi-resolution, multi-sensor comparison. Advances in Water Resources 31:1503-1514.

Mott, R. and Lehning, M. 2010. Meteorological modeling of very high-resolution wind fields and snow deposition for mountains. Journal of Hydrometeorology 11(4):934-939.

NSIDC. 2004. Snow Data Assimilation System (SNODAS) Data Products at NSIDC, Version 1. Boulder, Colorado USA. NSIDC: National Snow and Ice Data Center. doi: https://doi.org/10.7265/N5TB14TC.

Penczykowski, R.M., Connolly, B.M., and Barton, B.T. 2017. Winter is changing: Trophic interactions under altered snow regimes. Food Webs 13:80-91.

Petersky, R.S., Shoemaker, K.T., Weisberg, P.J., and Harpold, A.A. 2019. The sensitivity of snow ephemerality to warming climate across an arid to montane vegetation gradient. Ecohydrology 12:e2060.

Pimentel, R., Herrero, J., and Polo, M.J. 2015. Subgrid parameterization of snow distribution at a Mediterranean site using terrestrial photography. Hydrology and Earth System Sciences 21:805-820.

Pozzanghera, C.B., Sivy, K.J., Lindberg, M.S., and Prugh, L.R. 2016. Variable effects of snow conditions across boreal mesocarnivore species. Canadian Journal of Zoology 94(10):697-705.

R Core Team. 2021. R: A language and environment for statistical computing. R Foundation for Statistical Computing, Vienna, Austria. <https://www.R-project.org/>.

Roth, T.R. and Nolin, A.W. 2019. Characterizing maritime snow canopy interception in forested mountains. Water Resources Research 55:4564–4581.

Schwartz, A., McGowan, H., and Callow, N. 2021. Snowpack thermal patterns in pre- and post-bushfire snow gum forests. Journal of Hydrology 602:126789.

Seyednasrollah, B. and Kumar, M. 2014. Net radiation in a snow-covered discontinuous forest gap for a range of gap sizes and topographic configurations. Journal of Geophysical Research: Atmospheres 119:10323-10342.

Sirén, A.P.K., Somos-Valenzuela, M., Callahan, C., Kilborn, J.R., Duclos, T., Trager, C., and Morelli, T.L. 2018. Looking beyond wildlife: Using remote cameras to evaluate accuracy of gridded snow data. Remote Sensing in Ecology and Conservation 4(4):375-386.

Steen, J.B., Erikstad, K.E., and Høidal, K. 1992. Cryptic behaviour in moulting hen willow ptarmigan lagopus l. lagopus during snow melt. Ornis Scandinavica 23(1):101-104.

Steenweg, R., Hebblewhite, M., Kays, R., Ahumada, J., Fisher, J.T., Burton, C., Townsend, S.E., Carbone, C., Rowcliffe, J.M., Whittington, J., Brodie, J., Royle, J.A., Switalski, A., Clevenger, A.P., Heim, N., and Rich, L.N. 2017. Scaling-up camera traps: monitoring the planet's biodiversity with networks of remote sensors. Frontiers in Ecology and Evolution 15(1):26–34.

Stone, P.H. and Carlson, J.H. 1979. Atmospheric lapse rate regimes and their parameterization. Journal of the Atmospheric Sciences 36:415-423.

Strasser, U., Bernhardt, M., Weber, M., Liston, G.E., and Mauser, W. 2008. Is snow sublimation important in the alpine water balance? The Cryosphere 2(1):53-66.

Strickfaden, K.M., Marshall, A.M., Svancara, L.K., Ausband, D.E., and Link, T.E. edger: An R package facilitating distance and snow depth measurements at remote camera stations. Remote Sensing in Ecology and Conservation. In review.

Sun, N., Wigmosta, M., Zhou, T., Lundquist, J.D., Dickerson-Lange, S.E, and Cristea, N. 2018. Evaluating the functionality and streamflow impacts of explicitly modelling forest–snow interactions and canopy gaps in a distributed hydrologic model. Hydrological Processes 32:2128-2140.

Teich, M., Giunta, A.D., Hagenmuller, P., Bebi, P., Schneebeli, M., and Jenkins, M.J. 2019. Effects of bark beetle attacks on forest snowpack and avalanche formation – Implications for protection forest management. Forest Ecology and Management 438:186-203.

Terando, A.J., Youngsteadt, E., Meineke, E.K., and Prado, S.G. 2017. Ad hoc instrumentation methods in ecological studies produce highly biased temperature measurements. Ecology and Evolution 7:9890-9904.

Thimonier, A., Sedivy, I., and Schleppi, P. 2010. Estimating leaf area index in different types of mature forest stands in Switzerland: a comparison of methods. European Journal of Forest Research 129:543-562.

USDA Natural Resources Conservation Service. 2022. Report Generator 2.0. Retrieved from https://wcc.sc.egov.usda.gov/reportGenerator/. Accessed 8 June 2022.

USGS EROS Center. 2018. USGS EROS Archive - Landsat - Landsat Level-3 Fractional Snow Covered Area (fSCA) Science Product. doi: /10.5066/F7XK8DS5.

Vermote, E. 2019. NOAA Climate Data Record (CDR) of AVHRR Surface Reflectance, Version 5. NOAA National Centers for Environmental Information. https://doi.org/10.7289/V53776Z4.

Webb, R.W., Raleigh, M.S., McGrath, D., Molotch, N.P., Elder, K., Hiemstra, C., Brucker, L., and Marshall, H.P. 2020. Within-stand boundary effects on snow water equivalent distribution in forested areas. Water Resources Research 56: e2019WR024905.

Zhang, Y. and Liang, S. 2014. Surface radiative forcing of forest disturbances over northeastern China. Environmental Research Letters 9(2):024002.

Figures and Tables

Table 3. Model selection table for data-rich generalized linear models. Variables are mean December-February air temperature (MeanDJFTemp), mean snow depth (MeanSD), aspect, vegetation cover percent from hemispherical photographs (VegCover), and cold-air pooling potential (CAP). Only shown are models with w_i >= 0.01.

	Intercept	df	Log Likelihood	AIC_c	ΔAIC_c	w_i
MeanDJFTemp * MeanSD +Aspect + VegCover	73.61	9	-430.64	880.74	0.00	0.54
MeanDJFTemp * MeanSD + VegCover + Aspect + CAP	73.61	10	-430.64	883.08	2.34	0.17
VegCover * CAP + MeanDJFTemp + Aspect + MeanSD	80.60	10	-430.96	883.72	2.98	0.12
MeanDJFTemp + Aspect + VegCover + MeanSD	79.31	8	-434.14	885.44	4.70	0.05
MeanDJFTemp * VegCover + Aspect + MeanSD	81.67	9	-433.89	887.25	6.50	0.02
MeanDJFTemp + Aspect * VegCover + MeanSD	73.94	11	-431.59	887.37	6.63	0.02
MeanDJFTemp + Aspect + VegCover * MeanSD	77.52	9	-433.98	887.42	6.68	0.02
MeanDJFTemp + Aspect + VegCover + CAP + MeanSD	79.32	9	-434.14	887.74	7.00	0.02

Table 4. Covariates in best-fit data-rich model. Variables are mean December-February air temperature (MeanDJFTemp; continuous), mean snow depth (MeanSD; continuous), aspect (categorical, reference is West), and vegetation cover percent from hemispherical photographs (VegCover; continuous).

Coefficient	Beta	Std. Error	Low 95% CI	High 95% CI	p-value
Intercept	73.605	3.187	67.358	79.852	<0.001
MeanDJFTemp	-11.344	1.848	0.350	6.853	<0.001
MeanSD	0.344	0.066	2.760	9.449	<0.001
AspectEast	3.602	1.659	-1.751	4.505	0.032
AspectNorth	6.105	1.706	0.064	0.181	<0.001
AspectSouth	1.377	1.596	-14.965	-7.722	0.390
VegCover	0.123	0.030	0.216	0.473	<0.001
MeanDJFTemp * MeanSD	0.073	0.028	0.018	0.128	0.010

Table 5. Model selection table for data-constrained generalized linear models. Variables are elevation (Elev), aspect, canopy cover percent from a densiometer (CanCover), and cold-air pooling potential (CAP). Only shown are models with $w_i >= 0.01$.

Model	Intercept	df	Log Likelihood	AIC_c	ΔAIC_c	w_i
Elev + Aspect + CanCover * CAP	45.6	9	-455.6	930.65	0	0.60
Elev + Aspect * CanCover + CAP	39.03	11	-454.75	933.69	3.03	0.13
Elev + Aspect + CanCover + CAP	46.08	8	-458.28	933.72	3.07	0.13
Elev * CanCover + Aspect + CAP	39.42	9	-457.84	935.15	4.5	0.06
Aspect + CanCover + Elev * CAP	45.39	9	-458.22	935.9	5.25	0.04
Elev + CanCover + Aspect * CAP	47.13	11	-457.06	938.3	7.64	0.01

Table 6. Covariates in best-fit data-constrained model. Variables are elevation (Elev; continuous), aspect (categorical, reference is West), canopy cover percent from a densiometer (CanCover; continuous), and cold-air pooling potential (CAP; indicator).

Coefficient	Beta	Std. Error	Low 95% CI	High 95% CI	p-value
Intercept	45.600	4.434	36.910	54.291	<0.001
Elev	0.051	0.004	0.044	0.059	<0.001
AspectEast	6.944	2.011	3.004	10.885	<0.001
AspectNorth	11.374	2.002	7.451	15.298	<0.001
AspectSouth	2.513	1.935	-1.280	6.305	0.197
CanCover	0.103	0.025	0.053	0.152	<0.001
CAP	-2.051	3.776	-9.452	5.349	0.588
CanCover * CAP	0.135	0.060	0.018	0.252	0.025

Fig. 9. Camera locations on Moscow Mountain in Latah County, ID in winter 2020-2021.

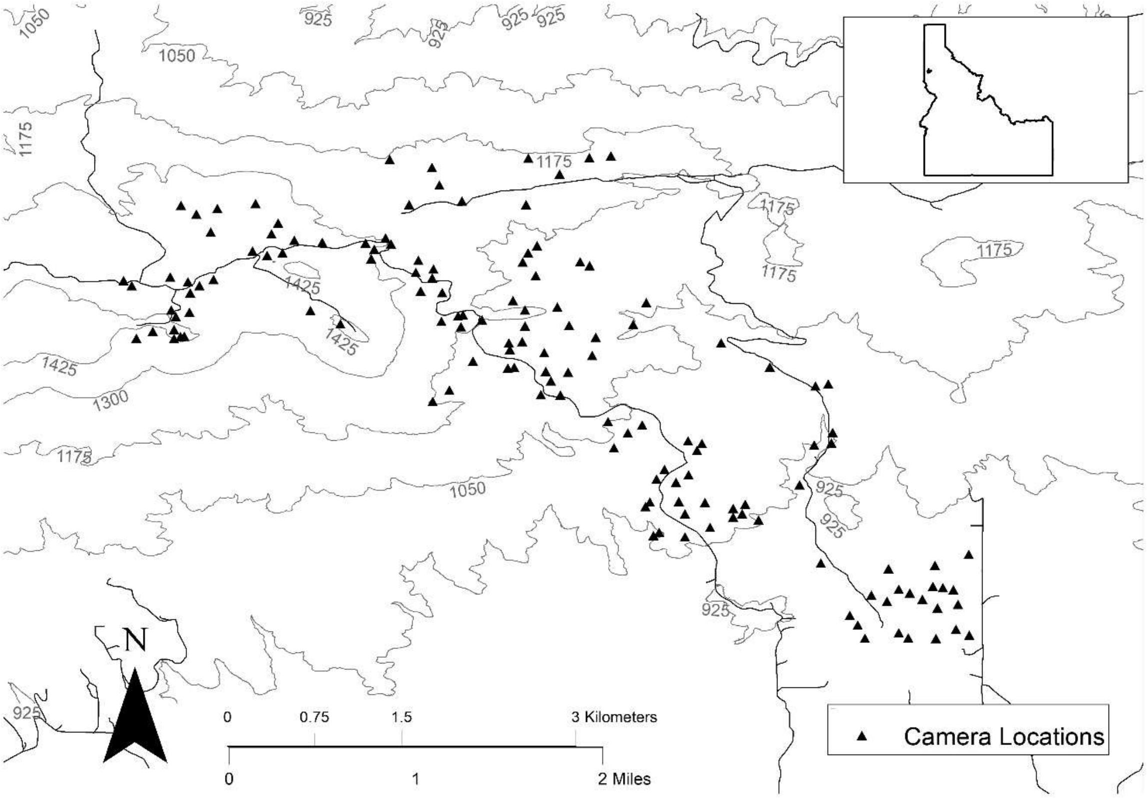

Fig. 10. Model predictions of snow disappearance date as a function of A) mean December-February (DJF) temperature and mean snow depth and B) aspect and vegetation cover percent.

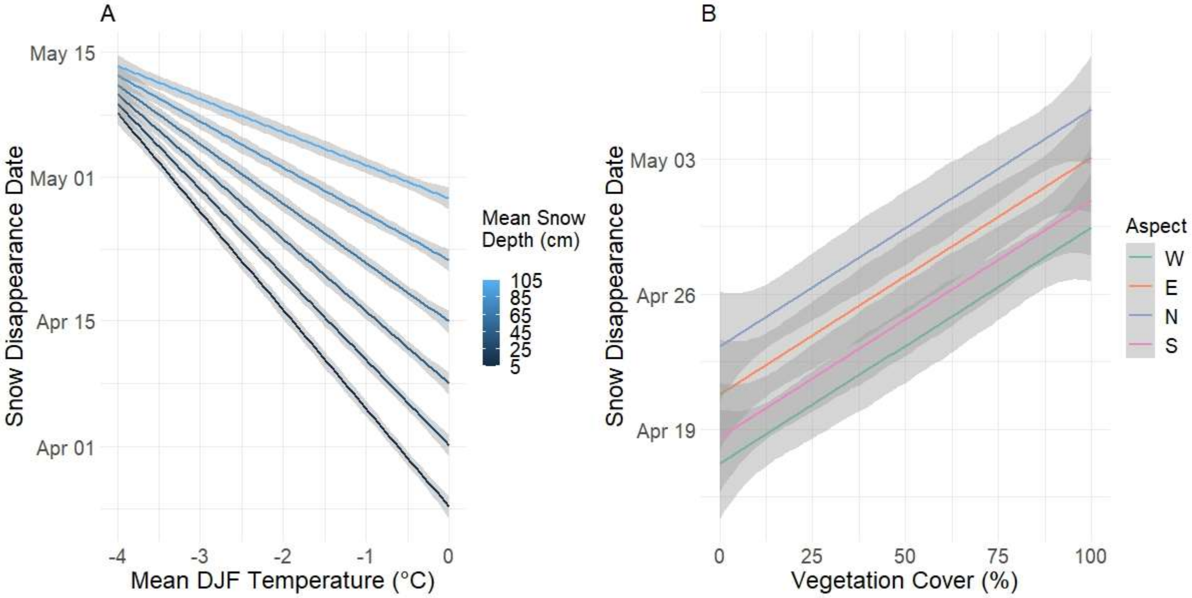

Fig. 11. Model predictions of the best-fit data-rich model compared to true snow disappearance dates (SDDs) of remote camera sites on Moscow Mountain in Latah County, ID.

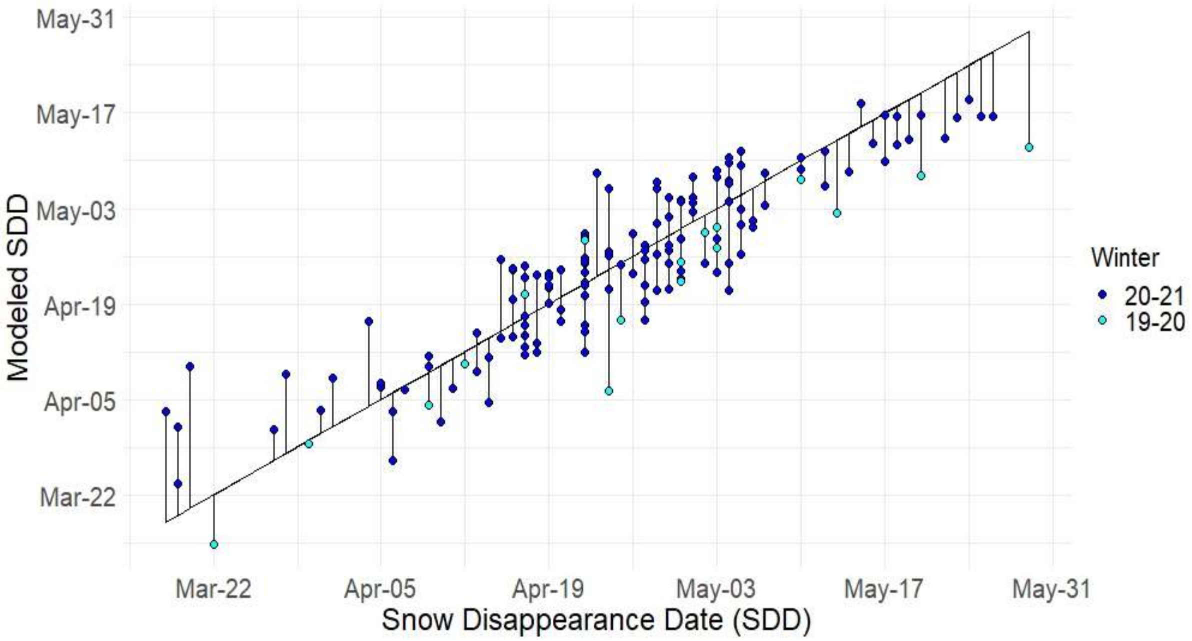

Fig. 12. Model predictions of snow disappearance date as a function of A) canopy cover percent and cold-air pooling (CAP) potential and B) elevation and aspect.

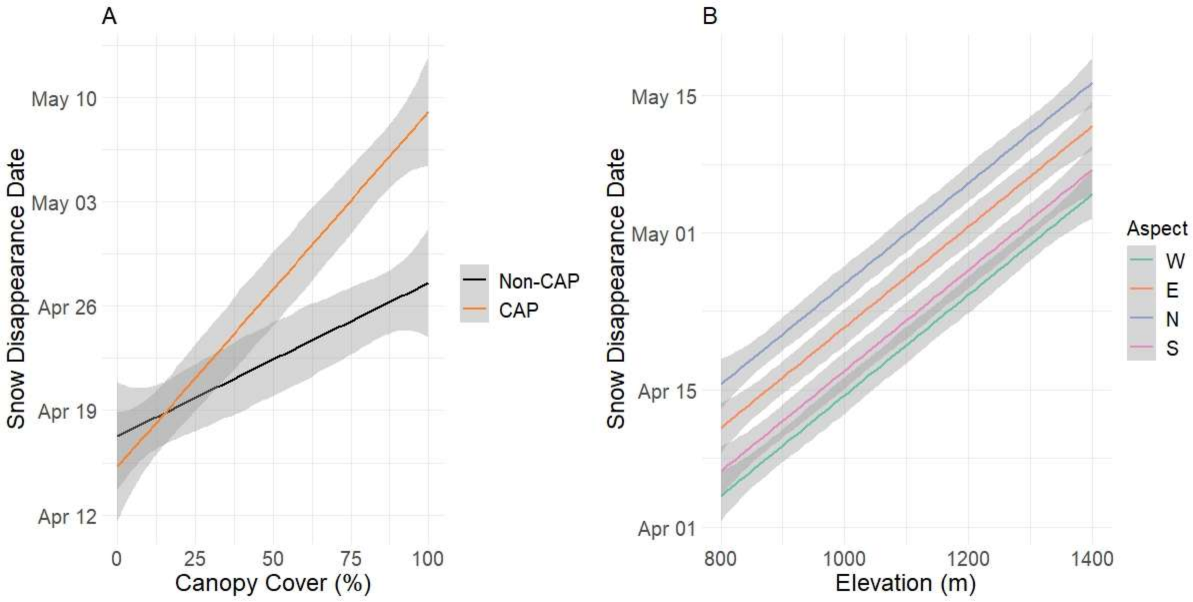

Fig. 13. Model predictions of the best-fit constrained model compared to true snow disappearance dates (SDDs) of remote camera sites on Moscow Mountain in Latah County, ID.

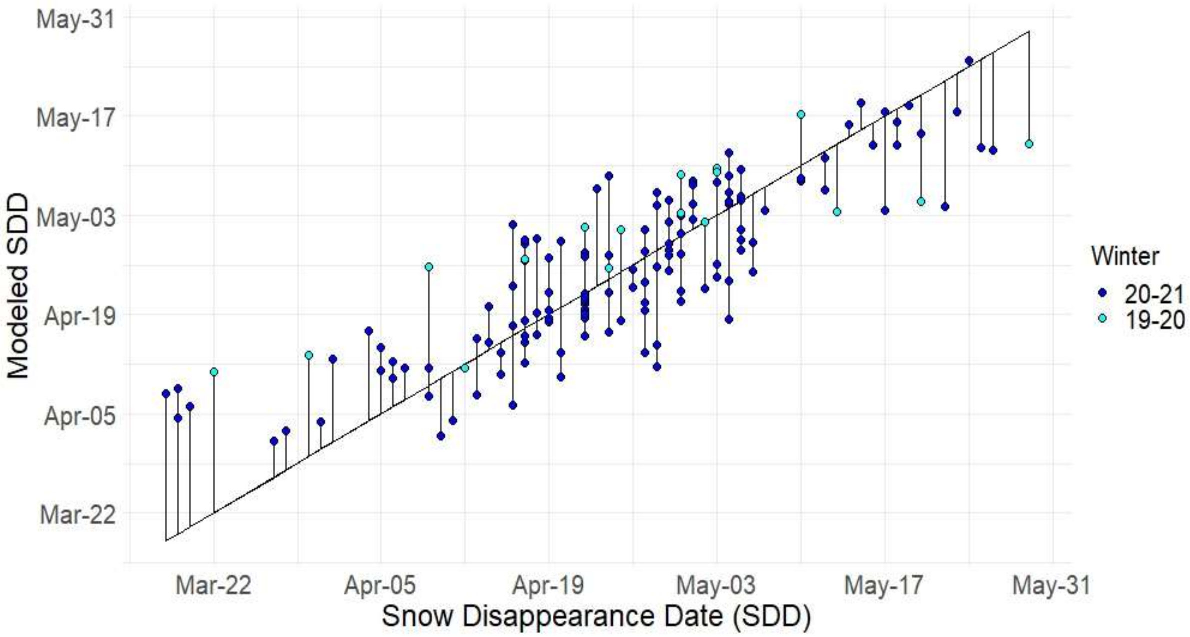

Figure 14. Maps of A) canopy cover, B) aspect, C) cold-air pooling potential, and D) relative snow disappearance date (SDD) predicted with the constrained model across Moscow Mountain in Latah County, ID. Pixels are 30 m^2 resolution except for Panel C in which pixels are 1 m^2 resolution.

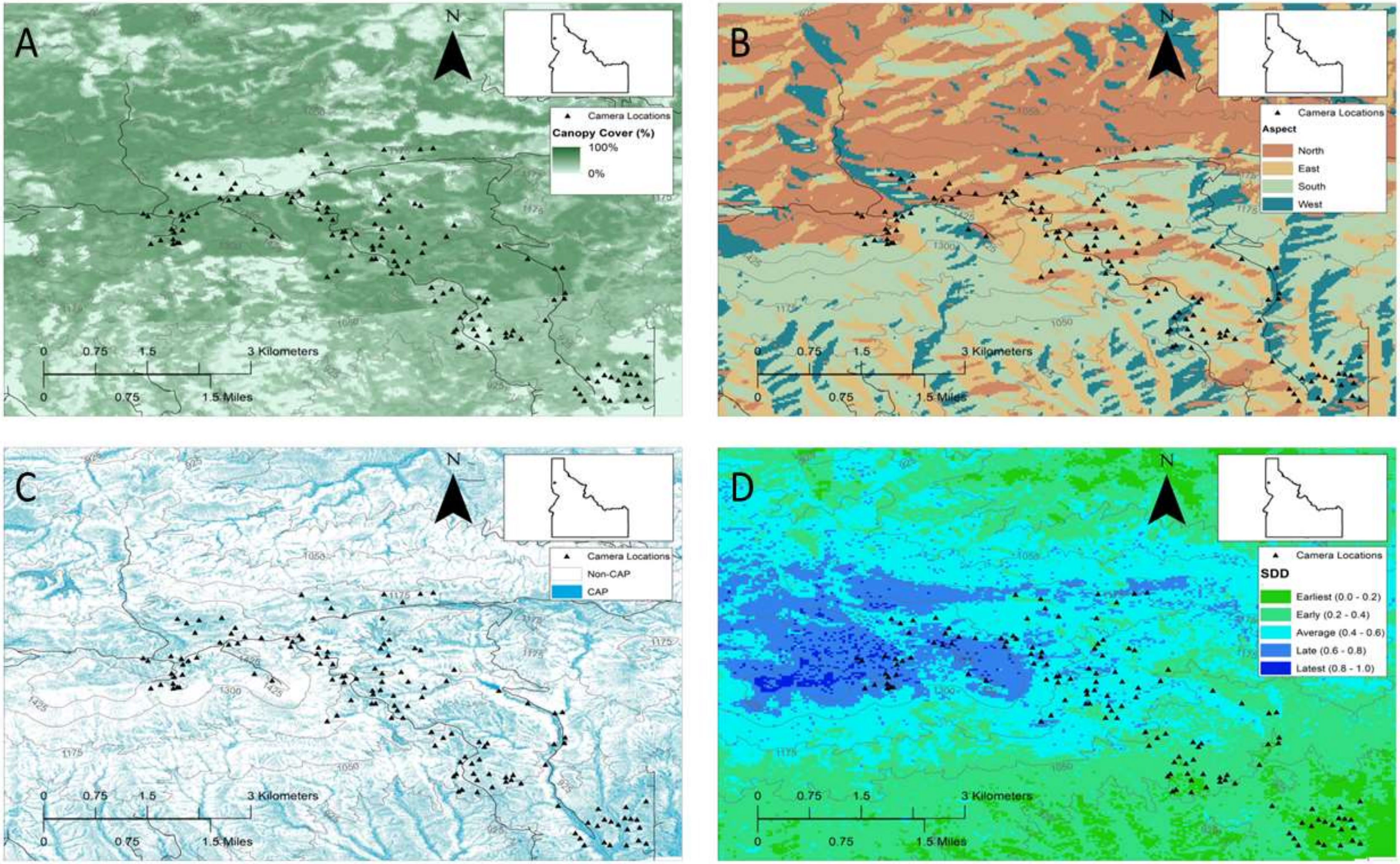

Chapter 3: Effects of Snow Conditions on Ungulate Presence at Camera Sites

Abstract

In the rain-snow transition zone of the Pacific Northwest, climate change is expected to increase the incidence of rain-on-snow and freeze-thaw events, which will change snow density and hardness dynamics. Wildlife species such as deer (*Odocoileus* spp.) and elk (*Cervus canadensis*) are affected by snow density and hardness through changes in their energy expenditure during movement and loss of access to forage. However, little is known about if and how ungulates select habitats based on snow density and hardness. We deployed a stratified network of remote cameras in a complex forested terrain to measure snow depth and detect deer and elk and collected snow density and hardness measurements throughout the winter to determine if the probability of ungulate presence at cameras was explained by snow conditions and air temperature at the sites. We found that snow depth and density had negative relationships with the probability of ungulate presence, while ram resistance (a proxy for snow hardness) had a marginal positive effect. We were able to estimate snow conditions at the camera sites using only camera data, which presents the opportunity for these methods to be used by managers who are interested in determining how ungulates are affected by snow depth, density, and hardness collectively. This knowledge can be used to inform ungulate management in a changing climate.

Introduction

Winter is a challenging period for wildlife communities. Species not using avoidance strategies such as migration or torpor must cope with snow, cold temperatures, and resource scarcity. Winter restructures foraging dynamics and predator-prey relationships between plants, herbivores, and carnivores and places greater energetic demands on all species (Penczykowski et al. 2017). Only limited quantities of low-quality forage are available to herbivorous species over winter because deciduous vegetation does not retain leaves throughout the winter and grasses and forbs are frequently covered by layers of snow and ice (Skogland 1978, Christianson and Creel 2007, Gilbert et al. 2017). Lower prey availability, either because prey animals have migrated or entered torpor or because remaining animals often hide in the subnivium of the snow, forces predators to use new hunting strategies to find food (Husseman et al. 2003). Even in mild winters, animals may be in a constant energy deficit (Parker et al. 1999). Low body mass or body fat condition during the winter increases the risk of death by predation or exposure (Mech et al. 2001), and low body condition continuing into the spring can affect an animal's ability to care for or even bear offspring (Horne et al. 2019).

Animals expend much more energy moving through snow than over bare ground (Parker et al. 1984, Bunnell et al. 1990). However, not all snow affects movement in the same way. The snowpack depth, density (the amount of water in a snowpack relative to its total depth), and hardness (mechanical strength) collectively determine how much difficulty wildlife have moving through snow (Bunnell et al. 1990) and subsequently if and how wildlife use specific habitats (Penczykowski et al. 2017). An animal's movement efficiency through snow is further dictated by its foot loading (the weight exerted over the surface area of its limbs) and chest height (Telfer and Kelsall 1984). Deeper and denser snow creates substantial drag on the legs of an animal as it wades through snow, forcing it to lift its legs higher to avoid having to wade through unfavorable snow (Parker et al. 1984). If the snow is dense or hard enough and the animal's foot loading is low enough, it may be able to walk on top of the snowpack rather than sink into it, allowing the animal to move effectively even where snow is deep (Parker et al. 1984). Furthermore, very dense and hard snow is also difficult for animals to dig through to find buried food resources (Skogland et al. 1978). Animals may use habitats with different snow conditions for different purposes. For instance, Pacific martens (*Martes caurina*) use areas with dense and hard snow for movement and hunting and use areas with deep and soft snow as thermal cover and visual cover from predators (Martin et al. 2020). Thus, a thorough understanding of wildlife habitat use in winter requires knowing not only the snow's depth but also its density and hardness.

Three species of management interest in the Northwestern United States are white-tailed deer (*Odocoileus virginianus*), mule deer (*O. hemionus*), and Rocky Mountain elk (*Cervus canadensis).* White-tailed and mule deer (collectively deer) and elk may conduct short migrations to find favorable winter range but often still occupy areas with snow cover in winter (Nicholson et al. 1997, Sabine et al. 2002, Rickbeil et al. 2019). Deer select areas with <38 cm of snow (DelGiudice et al. 2002) while elk select areas with <46 cm of snow

(Parker et al. 1984), though thresholds of selection often vary by study (see Table 1 in Ungulate Winter Range Technical Advisory Team 2005). Adult survival rates are lowest in the winter as they face higher risk of starvation and predation (Kautz et al. 2019). Ungulates, particularly juveniles, need access to high-quality summer and fall forage to build up necessary fat reserves for the winter (Hurley et al. 2014). Adult deer are at the highest risk of dying of malnutrition in severe winters when limited access to forage depletes their fat stores before the onset of snowmelt (Parker et al. 1999, Kautz et al. 2019).

Deer and elk sink deeper into snow than wolves (*Canis lupus*) and coyotes (*Canis latrans*) and thus have a more difficult time moving through the same snow while being pursued, which increases their risk of predation (Telfer and Kelsall 1984, Nelson and Mech 1986, Horne et al. 2019). Depleted fat reserves and poor snow conditions in late winter can exacerbate difficulties with escaping predation (Mech et al. 2001, DelGiudice et al. 2002, Kautz et al. 2019), particularly because intermediate snow densities provide the greatest movement advantage to predators over deer (Telfer and Kelsall 1984). Mech et al. (2001) reported a wolf pack had a high hunting success rate in a severe winter with an early rain-on-snow event that blocked forage access for the local elk herd. The milder winter the following year led to a decrease in the number of predation events, but it also led to a significant increase in predation on elk calves (Mech et al. 2001). Furthermore, females in poor body condition after a harsh winter may give birth to smaller fawns or calves, breed and give birth later in the year, or not breed at all (Horne et al. 2019). Juvenile ungulates, particularly smaller and younger individuals, have the highest winter mortality rate of any age class; at the same time, juvenile recruitment strongly influences population dynamics (Lukacs et al. 2018, Horne et al. 2019). Thus, the effects of a harsh winter on a population may not become apparent until years later when reproductive or recruitment rates are low (Horne et al. 2019).

Deer and elk are often managed post-winter using winter severity indices (WSIs), which quantify the difficulty of a winter in a particular study area using various hydrometeorological variables. The most common type of index such as the one by DelGiudice et al. (2002) scores each day based on if the snow depth exceeded a certain threshold and if its temperatures were lower than -17.7°C (0°F). The WSI is the sum of each day's score (DelGiudice et al. 2002). Other WSIs may include additional parameters such as a snowfall parameter (Boustead et al. 2005) or air chill and snow compaction parameters

(Verme 1968), or they may use snow-water equivalent instead of snow depth (Dawe and Boutin 2012). These WSIs can be used to predict the health of herds in the spring and subsequently inform management actions such as the number of tags to allocate to hunters (Dawe and Boutin 2012). Climate change is expected to generally decrease snow depths and increase temperatures overwinter, which, according to existing WSIs, will suggest that winters are becoming more favorable for ungulates. However, increased incidence of rain-on-snow (Knowles et al. 2006, Musselman et al. 2018) and freeze-thaw events (Masoero et al. 2020) and increased snowfall intensity (O'Gorman 2014) will alter snow density and hardness patterns, which may present new survival challenges to ungulates through increased energy expenditure during movement and decreased access to forage. Much attention has been paid to how deer and elk select habitats based on snow depth, but considerably less has been paid to how they select habitats based on snow density and hardness. Determining if and how ungulates select habitats based on the snow density and hardness will be crucial for effectively managing ungulates in a changing climate.

The general scientific objective of this study is to determine relationships between managed wildlife species and environmental variables which are expected to vary in a changing climate. We deployed a stratified network of remote cameras in complex forested terrain to measure snow depth and detect ungulates and paired these observations with snow density and hardness measurements at the sites to determine if the probability of ungulate presence was affected by snow and temperature conditions. We hypothesized there would be a combination of snow property and temperature predictors to best explain the probability of deer and elk presence at the camera sites. We predicted snow depth and snow density would be negatively related to detection probability, while snow hardness and air temperature would be positively related. Our secondary objective was to determine if we could use only data from cameras and data that could be reasonably collected in the field to detect these patterns of habitat use. While biophysical models exist which can estimate distributed snow data (Liston and Elder 2006), we sought to determine if snow properties derived from more empirical methods would be sufficient to detect patterns in ungulate use. This research will provide insight into how climate changes and variability are expected to affect ungulates in regions undergoing a transition from snow- to rain-dominated precipitation regimes.

Study Area

The study area for this project is the Palouse Range (hereafter Moscow Mountain) in Latah County, ID (Fig. 9). This field site was chosen because it has a wide variety of both topography and canopy cover in which to sample snow conditions and is conveniently located near the University of Idaho. Moscow Mountain has a network of 61 trails covering 106 km (66 miles) with reasonable access over winter.

Moscow Mountain spans approximately 800 to 1500 m above sea level. The forest cover is comprised of ponderosa pine (*Pinus ponderosa*) and Douglas-fir (*Pseudotsuga menziesii*) forests at low elevations and western red cedar (*Thuja plicata*) and fir (*Abies* sp.) forests at high elevations. The climate is characterized as continental-maritime comprised of generally Mediterranean conditions, with hot, dry summers and mild winters punctuated by periodic intrusions of cold air masses (Hubbart et al. 2007). Moscow Mountain receives an average of approximately 1060 mm of precipitation annually. The mean peak snow-water equivalent (SWE) for Moscow Mountain from water years 2001 – 2021 was 529 mm. In the winter 2020 – 2021 field season, the peak SWE was 594 mm, indicating the field season occurred in a snow year slightly above average. The peak SWE during the pilot field season in winter 2019-2020 was 518 mm, which is an average snow year for Moscow Mountain (USDA 2022). Moscow Mountain is also situated in the rain-snow transition zone of the Pacific Northwest, which is expected to undergo dramatic alterations to snow regimes in a changing climate (Klos et al. 2014, Marshall et al. 2019).

Methods

Snow Depth and Ungulate Detections from Cameras

We deployed 138 camera stations from October 2020 – May 2021. We used Reconyx® Hyperfire™ I and II cameras. We programmed cameras to record one image each hour of the day, including night hours, so each camera recorded at least 24 images every day throughout its deployment. We also programmed the cameras to take motion-triggered images to capture wildlife detections. We set cameras to the highest sensitivity with 3 images taken per trigger and a 1-second delay between images. We retrieved cameras after all snow cover had melted at the camera site (April – May 2021).

We stratified camera sites by elevation, aspect, and canopy cover. Elevation was classified from <925 m, 925-1,050 m, 1,050-1,175 m, 1,175-1,300 m, and >1,300 m; aspect was classified as N, S, E, or W; and canopy cover was classified as "sparse" for canopy covers <35%, "moderate" for canopy covers between 35-75%, and "dense" for canopy covers >75%. We took canopy cover measurements using a densiometer. We quasi-randomly selected sites within each strata to permit reasonable access via existing trail and forest road networks. After all strata were sampled, we placed additional cameras in landscape concavities and canopy gaps which are expected to retain snow later in the year (Curtis et al. 2014, Lawler and Link 2011). We also placed cameras at least 20 m away from other cameras given that snow conditions in complex terrains are often not correlated beyond this distance (Jost et al. 2007).

On the deployment date, we recorded the height and direction of the camera and the latitude, longitude, and elevation. We mounted and locked cameras onto trees at a height of 2–3 m to prevent snow from blocking the cameras. During camera deployment, we took reference images for superimposing a "virtual" snow stake (VSS) onto images to measure snow depth (Strickfaden et al., *in review*). We placed a reference snow stake with 2- and 10-cm gradations at 5, 10, and 15 m within the viewshed of the camera, and we allowed the camera to take motion-triggered images. We took an additional set of reference images on camera retrieval to account for potential changes in the camera's viewshed during its deployment. VSSs were then superimposed onto images using functions in the *edger* package (Strickfaden et al., *in review*). At a subset of cameras, we also installed a physical snow stake 5-15 m from the camera which was composed of a 183 cm U-post driven into the ground and a 152cm section of PVC pipe. These were used to verify measurements taken with the VSSs. We marked white PVC every 2 cm with black permanent marker and every 10 cm with brightly colored electrical tape. We then fixed a pipe to a U-post with cable ties. When a physical snow stake was installed at the camera site, we recorded the camera's horizontal distance to the physical snow stake. We maintained cameras throughout the season, coincident with snow density and hardness measurements, to change batteries, ensure proper function, and remove obstructing vegetation.

We placed an external LogTag ® TRIX 8 temperature recorder (hereafter 'LogTag') at each camera station. We programmed the LogTags to record temperatures at 45-minute intervals. The LogTags were housed inside of plastic protective coverings and radiation shields. Each radiation shield was comprised of 15 cm of PVC pipe covered in aluminum foil tape to reflect shortwave radiation and reduce longwave radiation loading. We drilled holes into the radiation shields to allow for increased air flow (Terando et al. 2017). We hung the LogTag in its housing at the same height as the camera on the north side of the tree or under canopy cover to minimize the potential impacts of direct shortwave radiation. If no branches meeting these criteria were available on the camera tree, we hung it on a nearby tree.

We recorded snow presence, snow depth, and detections of wildlife in each image. We measured snow depth using any VSSs and physical snow stakes present in images. Snow depths sometimes exceeded 150 cm, which was the height of the snow stakes; if snow depth exceeded 150 cm, snow depth was recorded as “150+” until snow could be accurately measured again. We identified wildlife to species or genus or marked them as “unknown” if they could not be confidently identified. We processed images using Timelapse2 software (Greenberg 2020).

Snow Density and Hardness Sampling

We took snow density and hardness measurements at camera sites during the winter beginning in December 2020. We took measurements every few weeks as logistics allowed. We took density and hardness samples near the camera site in snow visually similar to the snow in the camera viewshed to prevent snow conditions from being disturbed beyond normal camera deployment.

Snow density. We measured snow density with different samplers depending on snow depth. For snow depths <100 cm, we measured snow density using homemade samplers made of 3-inch diameter PVC pipe (Hanson 2015). For snow depths >100 cm, we measured snow density using a federal snow sampler. The sampler was inserted into the snow to remove a snow core. We retained the core if the depth of snow in the sampler was at least 90% of the actual snow depth and the base of the snowpack had been reached as evidenced by litter or a soil plug at the base of the core. After we removed the soil plug, we weighed the core to determine its snow-water equivalent (SWE). We converted the SWE measured with the samplers into a density measurement by dividing the SWE by the snow depth. If a snow core of adequate quality could not be obtained after several minutes of effort, we did not measure snow density on that sampling occasion.

We interpolated snow density values measured in the field to estimate snow density in the days between measurements. On the first day of snowfall, or on the day of camera deployment if the camera was deployed while snow was already present, we set the snow density to 80 kg/m^3 because this was the lowest snow density value recorded in field measurements. On the last day with snow cover, we set the snow density to 600 kg/m^3. We then linearly interpolated these values and the snow density values measured in the field to estimate the snow density on all camera deployment days. Though we recognize linear interpolation may miss out on some of the complexities of changes in snow density, more nuanced estimation of snow density would require modeling which does not align with the goals of this study.

Snow hardness. We measured snow hardness using a ram penetrometer or "ramsonde" (Snowmetrics; Fort Collins, CO). A ramsonde allows for an approximation of the amount of force needed to penetrate through layers of snow. A ramsonde is composed of a hammer, anvil, and tube. The hammer is dropped onto the anvil from a known height, and the depth to which the ramsonde penetrates the snow is recorded using gradations on the tube. Drops are performed until the ramsonde reaches the ground. Though the exact data recording process is subjective, data are typically recorded so the stratigraphy (layering) of the snowpack is captured. Ram resistance can be calculated for each snow layer using the equation $RR = 10 * (T + H + nfH/p)$, where T is the weight of the tube, H is the weight of the hammer, n is the number of drops, f is the height of the drops, and p is the penetration increment (American Avalanche Association 2016). The resultant ram resistance serves as a proxy for snow hardness (true hardness of snow cannot be measured with a ramsonde because of its physical properties; K. Elder, pers. comm.). We followed this procedure to collect snow hardness samples on 596 sampling occasions. We calculated ram resistance for the individual snow layers in the three hardness samples collected on each sampling occasion.

Takeuchi et al. (2007) derived an equation relating the hardness of snow to the snow's percent water content (WC) and density. WC is the percent of the snow's total water volume made up of liquid water, while density measures both liquid and frozen water. WC is related to snow hardness because liquid water breaks down the bonds between frozen water particles. The following is the equation from Takeuchi et al. (2007; hereafter the Takeuchi equation), as translated by Ito et al. (2012):

$$H = 1.31 * 10^{-8} * \rho^4 * e^{-0.18*WC} \qquad \textit{Eqn. 1}$$

where H is the snow hardness (in kPa), ρ is the snow density (in kg/m^3), and WC is the percent water content. This equation can then be rearranged to solve for WC.

$$WC = \frac{ln\left({}^{H}/_{1.31 * 10^{-8} * \rho^4}\right)}{-0.18} \qquad \textit{Eqn. 2}$$

Given a density sample and hardness profile for a camera site, this allows for the estimation of WC during each snow property sampling occasion.

Because the Takeuchi equation estimates snow hardness in kPa, we converted the ram resistance of each snow layer into an approximation in kPa by dividing the ram resistance by 1000 and then dividing again by the surface area of the conical head of the ramsonde, which is approximately 2.81 * 10^{-3} m^2. Both Takeuchi et al. (2007) and Ito et al. (2012) used a push-pull gauge to measure snow hardness, which measures the maximum hardness needed to break through the snow. Therefore, we used the mean of the maximum ram resistance values recorded in the three snow hardness samples as the maximum ram resistance value for that sampling occasion. We used the maximum ram resistance and the bulk snow density value to solve for WC using the rearranged Takeuchi equation. It should be noted Ito et al. (2012) measured density and hardness along fixed depth intervals into a snowpack. However, because we measured bulk density and did not take ram resistance measurements at fixed depth intervals, we had to approximate WC for the entire snowpack. Ram resistance could be biased low if the final drop of the ramsonde hammer caused the ramsonde to break through a very hard ice layer to penetrate a deep soft layer below. This is not something for which we could reasonably account.

This equation returned WC values <0 in 43% of observations, which is physically impossible. Ito et al. (2012) built their snow hardness equation using data collected in a highly controlled lab experiment over the course of only 2 days. The snowpack in our study experienced complex combinations of processes that would not be present in a short lab experiment, including both dry and wet snow metamorphism, compaction, canopy unloading, and wind scouring over a long period of time. These processes contributed to higher ram resistance values than would be expected at a given snow density, which caused the rearranged Takeuchi equation to output negative WC values. It follows that the observations with negative WC values are those for which the effects of these other snow cohesion processes have overcome the effects of snow density and WC on snow hardness as described by Ito et al. (2012). Therefore, we will instead refer to WC as a "snow metamorphism index" (SMI), where a negative SMI indicates snowpacks in which bonds have formed between snow granules because of these metamorphic processes, while a positive SMI indicates snowpacks in which bonds between snow granules are actively weakening due to wet snow metamorphism.

With these estimated SMI values on each sampling occasion, we built a suite of generalized linear models to predict SMI values from data collected at the camera sites. Variables included were the interpolated snow density; the air temperature at the time of the sample; a 12-, 24-, 48-, or 72-hour mean temperature before the sampling occasion; the number of freeze-thaw cycles that occurred in the 12, 24, 48, or 72 hours before the sampling occasion; the total number of freeze-thaw cycles that occurred before the sampling occasion; and whether it was precipitating during a sampling occasion. We defined a freeze-thaw cycle as a time interval in which both above-freezing and below-freezing temperatures were recorded. All temperature values used were those recorded by the LogTag rather than by the camera. We tested combinations of these variables and their interactions, and we selected the top model based on both its R^2 value and its score using Akaike's Information Criterion (AIC; Akaike 1973). Given the highly complex nature of snow hardness, we used many interactions in our models (Table S1).

The GLM with the highest R^2 value ($R^2 = 0.63$) contained interactions between snow depth, snow density, air temperature at the time of the sample, the 48-hour mean temperature, total freeze-thaw cycles, and the precipitation indicator. However, the model with the second highest R^2 value ($R^2 = 0.60$) had the lowest AIC score of all tested models and had a considerably lower AIC score than the first model ($\Delta AIC = 38.77$). Therefore, we decided this model had the most support and had an adequate fit. This model contained interactions between snow depth, snow density, air temperature at the time of the sample, the 48-hour mean air temperature, and total freeze-thaw cycles. Though the highly complex interactions make it difficult to determine the relative influence of each of these variables on predicted maximum ram resistance, this is acceptable because these variables, except for snow density, may not be indicative of snow hardness out of the context of the other variables.

The maximum ram resistance calculated with the predicted SMI values matched reasonably well with the measured maximum ram resistance at lower maximum ram resistance values but matched more poorly at higher maximum ram resistance values. When the true measured value was >100 kPa (n = 197), 52% of predicted values were less than half of their true measured values (Fig. 15). Conversely, when the true measured value was <100 kPa (n = 337), only 9.8% of predicted values were less than half of their true measured value. Predictions were more than double their true measured value in 9.9% of observations, and predictions were only doubled at true measured values <100 kPa. Altogether, these results indicate this model of WC has a greater tendency to underestimate ram resistance.

The GLM for SMI was applied to the camera data and used to predict ram resistance values. Some predicted ram resistance values exceeded a reasonable upper limit of 3,000 kPa for snow hardness (Höller and Fromm 2010). Predicted ram resistance values exceeding this upper limit were set to 3,000 kPa. Despite errors in the predictions at higher ram resistance values (>100 kPa), only 25% of all predicted ram resistance values were >100 kPa. These modeled ram resistance values are sufficient to begin to determine patterns between snow hardness and ungulate detection.

Data Analysis

We used logistic regression analysis to examine associations between snow and temperature conditions and ungulate presence at cameras. We grouped data by camera day. Snow depth, snow density, ram resistance, and air temperature from the LogTag were recorded as means for each data. We scaled predictors without centering before model fitting to make the estimates more comparable. We recorded ungulate presence as a 1 if a deer or elk was detected at any time on a day and as a 0 if no deer or elk were detected. Every model also included a random effect for camera site. We tested combinations of these predictors and interactions between them using the lme4 package (Bates et al. 2015) in the R programming language (R Core Team 2022), and we selected the best-fit model using AIC scores (Akaike 1973). We also assessed the classification accuracy of the models using Area Under Curve (AUC; Hosmer and Lemeshow 2000) analysis with the pROC package (Robin et al. 2011).

We used DeLong's test for ROC curves to determine significant differences between AUC scores (DeLong et al. 1988). Finally, we used analysis of variance (ANOVA) to assess the significance of the random effect.

Results

We used data from 134 of the 138 cameras deployed in 2020-2021. One camera was stolen, and two cameras malfunctioned. A fourth camera did not have a functioning LogTag accompanying it, so it was also excluded. We captured approximately 852,000 images with the remaining 134 cameras across 23,111 camera days. About 551,600 of these images were timelapse images, while 300,200 were motion-triggered images. We detected wildlife in 33,158 images (Table S2). We detected 1,930 deer in 16,377 images distributed across 917 camera days. We included 24 images of 6 individuals known to be in the *Odocoileus* genus but could not be identified to the species level. We only detected elk in 27 images with no snow. Thus, we excluded elk from our analysis and instead focused our analysis on deer presence at camera sites. The mean snow depth, snow density, and maximum ram resistance were 49.9 cm (SD = 44.7), 247.9 kg/m^3 (SD = 130.3), and 68.1 kPa (SD = 87.9), respectively (Fig. S1). Though snow depth could only be measured to 150 cm from images, snow depths of up to 203 cm were recorded during snow density and hardness sampling.

There were 3 competing logistic regressions describing daily probability of deer presence at cameras (Table 7). All three competing models contained snow depth, snow density, and an interaction between depth and density. Two of the top models also contained ram resistance, and one contained air temperature, though temperature was not a significant parameter in this model ($p = 0.894$). The model with the lowest AIC score contained snow depth, snow density, an interaction between depth and density, and ram resistance (Table 8). In this model, snow density and the interaction term were highly significant ($p < 0.001$ for both), snow depth was significant ($p = 0.052$), and ram resistance was marginally significant ($p = 0.097$; Fig. 16). The mean daily probability of deer presence when there was no snow was 0.16. For each 10 cm increase in snow depth, the probability of detecting a deer decreased by 12%. For each 50 kg/m^3 increase in snow density, the probability of detecting a deer decreased by 9%. The rate of decrease in detection probability is greater at high values of depth or density than at low values as density or depth increase (Fig. 17). Finally, for each

50 kPa increase in ram resistance, the probability of detecting a deer increased by 3%. The ANOVA test on the top model with and without the random effect found the random effect for camera was significant ($p < 0.001$), and adding the random effect reduced the AIC score by 275 points.

The single-variable model with the highest AUC score was the snow depth model, followed by snow density, ram resistance, and finally mean temperature. The AUCs of the three competing models were all around 0.885, indicating very high predictive power (Fig. 18). These models all had significantly different AUC scores ($p < 0.001$) than a "status quo" model containing only snow depth and mean temperature (AUC = 0.873). This suggests the top models all were significantly better at predicting whether a deer was detected on a particular day than the status quo model.

Discussion

We found snow depth and density had strong negative effects on the probability of deer presence at camera sites, while maximum ram resistance (the proxy for snow hardness) had a slight positive effect on probability of deer presence. These findings suggest deer select for habitats to minimize their energy expenditure during movement. This is consistent with Parker et al. (1999), who found movement through snow and burial of forage by snow contributed 4.7 times more on average to energy expenditure in black-tailed deer (*O. hemionus sitkensis*) than cold temperatures. There was also considerable variability in probability of deer presence between camera sites which was captured by the random effect for camera in the models. This random effect could have been capturing factors such as home ranges of individual deer or deer groups on Moscow Mountain, the distribution of forage resources, and risk of predation for which we did not explicitly account. Despite the highly influential random effect, the three snow property parameters still had significant or marginally significant effects on probability of deer presence.

Snow depths of 38 cm are often thought to represent an upper limit of snow depth beyond which deer will no longer select habitats. However, we detected 129 individual deer across 52 camera days in snow depths >38 cm, and we even detected 9 deer at snow depths >100 cm. When deer detections occurred at deeper snow depths, they occurred in one of three sets of conditions: 1) in early winter when the body condition of deer was at its highest and they had sufficient energy to wade through deep snow, 2) on dense and hard snow in which sinking depths would be low, or 3) when deer could follow existing tracks which were functionally localized areas of hard-packed snow in otherwise softer snow. These observations highlight that snow depth alone is not always sufficient for determining deer habitat selection in the winter.

We originally set out to examine the effects of snow conditions on both deer and elk. However, elk were rarely detected by our cameras and could not be included in our analysis. Elk in the study area likely move to lower-elevation agricultural fields with low snow depths and easier access to graze over winter (T. Link, pers. comm.). Associations of elk with snow density and hardness warrant further research in known elk winter range. We expect such research would discover a quadratic relationship between elk detection probability and snow density and hardness. Low values of density and hardness might be indicative of areas with greater foraging opportunity for grazers such as elk (Fortin et al. 2005), while high values of density and hardness would indicate areas of more efficient movement as was likely the case with deer. Mid-range values of density and hardness would provide poor conditions for either behavior because denser and harder snow is more difficult to move aside to access forage and also increases energy expenditure during movement.

Deer may more easily be able to cope with changes in snow properties than elk. Deer and elk have similar indices of movement efficiency in snow according to Telfer and Kelsall (1984), but deer have a lower chest height and lower foot loading, while elk have a greater chest height and greater foot loading. Additionally, deer can splay their hooves to further reduce their foot loading whereas elk cannot (Parker et al. 1984). When snow is soft and powdery, elk have an easier time moving through the snow than deer because of their proportionally longer legs. However, when snow is dense and hard, deer have the advantage because their lower foot loading reduces their sinking depths (Parker et al. 1984). Elk prefer to graze (Christianson and Creel 2007), which forces them to dig through the snow (crater) to expose forage. When snow is very dense and hard, cratering may not be possible or worth the energetic cost (Skogland 1978). For that reason, rain-on-snow events are particularly problematic for elk, as they create hard frozen layers elk have difficulty cratering (Mech et al. 2001). Conversely, shrubs, tree limbs, lichens, and even some invasive plant species such as spotted knapweed (*Centaurea stoebe*) are often available above snow cover as forage for browsers without much effort (Wright and Kelsey 1997, Christenson et al. 2014). White-tailed deer have also been known to take advantage of hard and compacted snow to reach arboreal forage (Massé and Côté 2012). We did not find any documented accounts of elk using this foraging strategy. Altogether, these factors might suggest deer exhibit more plastic movement and foraging behaviors that give them an advantage in poor snow conditions over elk (Telfer and Kelsall 1984).

All the variables used in the final model of probability of deer presence are variables which can be estimated or derived from camera data. We derived snow depth from hourly images taken by the cameras. Air temperature measurements of cameras which are not in direct sunlight are accurate to within 2°C of true air temperature about 66% of the time (Chapter 1B). Models exist which allow for the estimation of snow density based on day of year (Pistocchi 2016) or meteorological data (Meløysund et al. 2007). The most difficult parameter to estimate is ram resistance. Snow hardness is highly complex and can change drastically over the course of a day dependent on meteorological conditions. We were able to estimate maximum ram resistance for the purpose of this study using an empirical model, particularly when maximum ram resistance was <100 kPa. However, a single estimate of maximum ram resistance may not paint a complete picture of deer habitat use over winter. Deer may respond differently to hard crusts at the surface, middle, or bottom of a snowpack (Bunnell et al. 1990). Snow hardness may be a snow property which should be estimated using complex biophysical models, because these biophysical models would capture more of the snow's stratigraphy and more accurately categorize very hard snowpacks.

Conclusions

Deer are an economically and ecologically important species in the Pacific Northwest that are often managed post-winter using winter severity indices including only snow depth and temperature. However, we found evidence deer also select habitats based on snow density and hardness. Habitat selection decisions by deer have important implications for their energy expenditure and forage intake over winter, which have cascading effects on their survival and reproduction. We were able to measure or estimate snow properties using remote cameras, which are a cost-effective tool already widely used for wildlife research. This presents the opportunity to estimate these crucial snow parameters on fine scales so that they can be used to inform ungulate management in the changing climate of the rain-snow transition zone of the Pacific Northwest.

References

American Avalanche Association. 2016. Snow, weather, and avalanches: Observation guidelines for avalanche programs in the United States. Third edition. Victor, ID.

Akaike H. 1973. Information theory and extension of the maximum likelihood principle. Pages 267–281 in Petrov BN, Csaki F, editors. Second international symposium on information theory. Akademiai Kiando, Budapest, Hungary.

Bates, D., Maechler, M., Bolker, B., and Walker, S. 2015. Fitting linear mixed-effects models using lme4. Journal of Statistical Software 67(1):1-48. doi:10.18637/jss.v067.i01.

Boustead, B.E.M., Hilberg, S.D., Shulski, M.D., and Hubbard, K.G. 2015. The accumulated winter season severity index (AWSSI). Journal of Applied Meteorology and Climatology 54:1693-1712.

Bunnell, F.L., Parker, K.L., McNay, R.S., and Hovey, F.W. 1990. Sinking depths of black-tailed deer in snow, and their indices. Canadian Journal of Zoology 68:917-922.

Christianson, D.A. and Creel, S. 2007. A review of environmental factors affecting elk winter diets. Journal of Wildlife Management 71(1):164-176.

Curtis, J.A., Flint, L.E., Flint, A.L., Lundquist, J.D., Hudgens, B., Boydston, E.E., and Young, J.K. 2014. Incorporating cold-air pooling into downscaled climate models increases potential refugia for snow-dependent species within the Sierra Nevada ecoregion, CA. PLoS ONE 9(9): e106984. doi:10.1371/journal.pone.0106984.

Dawe, K.L. and Boutin, S. 2012. Winter severity index using widely available weather information. Wildlife Research 39(4):321-328.

DelGiudice, G.D., Riggs, M.R., Joly, P., and Pan, W. 2002. Winter severity, survival, and cause-specific mortality of female white-tailed deer in north-central Minnesota. Journal of Wildlife Management 66(3):698-717.

DeLong, E.R., DeLong, D.M., and Clarke-Pearson, D.L. 1988. Comparing the areas under two or more correlated receiver operating characteristic curves: A nonparametric approach. Biometrics 44:837-845.

Fortin, D., Morales, J.M., and Boyce, M.S. 2005. Elk winter foraging at fine scale in Yellowstone National Park. Oecologia 145:335–343.

Gilbert, S.L., Hundertmark, K.J., Person, D.K., Lindberg, M.S., and Boyce, M.S. 2017. Behavioral plasticity in a variable environment: snow depth and habitat interactions drive deer movement in winter. Journal of Mammalogy 98(1):246-259.

Greenberg, S. 2020. The Timelapse user guide version 2.2.3.6. http://saul.cpsc.ucalgary.ca/timelapse/pmwiki.php?n=Main.Userguide.

Hanson, G. 2015. “Low Cost Snow Tube Fabrication.” National Weather Service. https://www.weather.gov/media/btv/snowtubeinstr.pdf. Accessed 3 December 2020.

Höller, P. and Fromm, R. 2010. Quantification of the hand hardness test. Annals of Glaciology 51(54):39-44.

Horne, J.S., Hurley, M.A., White, C.G., and Rachael, J. 2019. Effects of wolf pack size and winter conditions on elk mortality. Journal of Wildlife Management 83(5):1103–1116. doi:10.1002/jwmg.21689.

Hubbart, J.A., Link, T.E., Gravelle, J.A., and Elliot, W.J. 2007. Timber harvest impacts on water yield in the continental/maritime hydroclimatic region of the United States. Forest Science 53(2):169-180.

Hurley, M.A., Hebblewhite, M., Gaillard, J-M, Dray, S., Taylor, K.A., Smith, W.K., Zager, P., and Bonenfant, C. 2014. Functional analysis of Normalized Difference Vegetation Index curves reveals overwinter mule deer survival is driven by both spring and autumn phenology. Philosophical Transactions of the Royal Society B 369: 20130196.

Ito, Y., Matsushita, H., Hirashima, H., Ito, Y., and Noro, T. 2012. Change in snow strength caused by rain. Annals of Glaciology 53(61):1-5.

Jenkins, D.A., Schaefer, J.A., Rosatte, R., Bellhouse, T., Hamr, J., and Mallory, F.F. 2007. Winter resource selection of reintroduced elk and sympatric white-tailed deer at multiple spatial scales. Journal of Mammalogy 88(3):614–624.

Kautz, T.M., Belant, J.L., Beyer, D.E., Strickland, B.K., and Duquette, J.F. 2020. Influence of body mass and environmental conditions on winter mortality risk of a northern ungulate: Evidence for a late-winter survival bottleneck. Ecology and Evolution 10:1666-1677.

Knowles, N., Dettinger, M.D., and Cayan, D.R. 2006. Trends in snowfall versus rainfall in the western United States. Journal of Climate 19:4545-4559.

Lawler, R.R., and Link, T.E. 2011. Quantification of incoming all-wave radiation in discontinuous forest canopies with application to snowmelt prediction. Hydrological Processes 25:3322-3331.

Liston, G.E., and Elder, K. 2006. A distributed snow-evolution modeling system (SnowModel). Journal of Hydrometeorology 7:1259-1276.

Lukacs, P.M., Mitchell, M.S., Hebblewhite, M., Johnson, B.K., Johnson, H., Kauffman, M., Proffitt, K.M., Zager, P., Brodie, J., Hersey, K., Holland, A.A., Hurley, M.A., McCorquodale, S., Middleton, A., Nordhagen, M., Nowak, J.J. and White, P.J. 2018. Factors influencing elk recruitment across ecotypes in the western United States. Journal of Wildlife Management 82(4):698–710.

Martin, M.E., Moriarty, K.M., and Pauli, J.N. 2020. Forest structure and snow depth alter the movement patterns and subsequent expenditures of a forest carnivore, the Pacific marten. Oikos 129:356–366.

Masoero, G., Laaksonen, T., Morosinotto, C., and Korpimäki, E. 2020. Climate change and perishable food hoards of an avian predator: Is the freezer still working? Global Change Biology 26:5414–5430.

Massé, A. and Côté, S.D. 2012. Linking alternative food sources to winter habitat selection of herbivores in overbrowsed landscapes. Journal of Wildlife Management 76(3):544–556.

Mech, L.D., Smith, D.W., Murphy, K.M., and MacNulty, D.R. 2001. Winter severity and wolf predation on a formerly wolf-free elk herd. Journal of Wildlife Management 65(4):998-1003.

Meløysund, V., Leira, B., Høiseth, K.V., and Lisø, K.R. 2007. Predicting snow density using meteorological data. Meteorological Applications 14:413-423.

Musselman, K.N., Lehner, F., Ikeda, K., Clark, M.P., Prein, A.F., Liu, C., Barlage, M., and Rasmussen, R. 2018. Projected increases and shifts in rain-on-snow flood risk over western North America. Nature Climate Change 8:808-812.

Nelson, M.E. and Mech, L.D. 1986. Relationship between snow depth and gray wolf predation on white-tailed deer. Journal of Wildlife Management 50(3):471-474.

Nicholson, M.C., Bowyer, R.T., and Kie, J.G. 1997. Habitat selection and survival of mule deer: Tradeoffs associated with migration. Journal of Mammalogy 78(2):483-504.

O’Gorman, P.A. 2014. Contrasting responses of mean and extreme snowfall to climate change. Nature 512:416-418.

Olson, L.O., Van Deelen, T.R., Storm, D.J., and Crimmins, S.M. 2021. Understanding environmental patterns of canid predation on white-tailed deer (Odocoileus virginianus). Canadian Journal of Zoology 99:912–920.

Parker, K.L. Robbins, C.T., and Hanley, T.A. 1984. Energy expenditures for locomotion by mule deer and elk. Journal of Wildlife Management 48(2):474-488.

Parker, K.L., Gillingham, M.P., Hanely, T.A., and Robbins, C.T. 1999. Energy and protein balance of free-ranging black-tailed deer in a natural forest environment. Wildlife Monographs 143:1-48.

Penczykowski, R.M., Connolly, B.M., and Barton, B.T. 2017. Winter is changing: Trophic interactions under altered snow regimes. Food Webs 13:80-91.

Pistocchi, A. 2016. Simple estimation of snow density in an alpine region. Journal of Hydrology: Regional Studies 6:82-89.

R Core Team. 2022. R: A language and environment for statistical computing. R Foundation for Statistical Computing, Vienna, Austria. <https://www.R-project.org/>.

Rickbeil, G.J.M., Merkle, J.A., Anderson, G., Atwood, M.P., Beckmann, J.P., Cole, E.K., Courtemanch, A.B., Dewey, S., Gustine, D.D., Kauffman, M.J., McWhirter, D.E., Mong, T., Proffitt, K., White, P.J., and Middleton, A.D. 2019. Plasticity in elk migration timing is a response to changing environmental conditions. Global Change Biology 25:2368–2381.

Robin, X., Turck, N., Hainard, A., Tiberti, N., Lisacek, F., Sanchez, J., and Müller, M. 2011. pROC: An open-source package for R and S+ to analyze and compare ROC curves. BMC Bioinformatics 12:77. doi: 10.1186/1471-2105-12-77.

Sabine, D.L., Morrison, S.F., Whitlaw, H.A., Ballard, W.B., Forbes, G.J., and Bowman, J. 2002. Migration behavior of white-tailed deer under varying winter climate regimes in New Brunswick. Journal of Wildlife Management 66(3):718-728.

Skogland, T. 1978. Characteristics of the snow cover and its relationship to wild mountain reindeer (Rangifer tarandus tarandus l.) feeding strategies. Arctic and Alpine Research 10(3):569-580.

Strickfaden, K.M., Marshall, A.M., Svancara, L.K., Ausband, D.E., and Link, T.E. edger: An R package facilitating distance and snow depth measurements at remote camera stations. Remote Sensing in Ecology and Conservation. In review.

Takeuchi, Y, Endo, Y., Murakami, S. and Niwano, S. 2007. Characteristics of snow hardness at Tokamachi during the winter of 2005–06. Journal of the Japanese Society of Snow and Ice 69:61–69 [in Japanese with English summary].

Takeuchi, Y., Nohguchi, Y., Kawashima, K., and Izumi, K. 1998. Measurement of snow-hardness distribution. Annals of Glaciology 26:27–30.

Telfer, E.S. and Kelsall, J.P. 1984. Adaptation of some large North American mammals for survival in snow. Ecology 65(6):1828-1834.

Terando, A.J., Youngsteadt, E., Meineke, E.K., and Prado, S.G. 2017. Ad hoc instrumentation methods in ecological studies produce highly biased temperature measurements. Ecology and Evolution 7:9890-9904.

Ungulate Winter Range Technical Advisory Team (UWRTAT). 2005. Desired conditions for mule deer, elk and moose winter range in the southern interior of British Columbia. BC Ministry of Water, Land and Air protection, Biodiversity branch, Victoria BC, Wildlife Bulletin B-120.

Wright, A.L. and Kelsey, R.G. 1997. Effects of spotted knapweed on a cervid winter-spring range in Idaho. Journal of Range Management 50(5):487-496.

Figures and Tables

Table 7. Top models for probability of deer presence on Moscow Mountain in Latah County, ID in winter 2020-2021. Only shown are models with $w_i > 0.01$.

Model	Intercept	df	Log Likelihood	AIC	ΔAIC	w_i
Depth * Density + Resistance	-1.94	6	-2958.66	5929.33	0	0.41
Depth * Density	-1.93	5	-2959.90	5929.81	0.48	0.32
Depth * Density + Resistance + AirTemp	-1.94	7	-2958.66	5931.32	1.98	0.15
Depth * Density + AirTemp	-1.92	6	-2959.87	5931.74	2.41	0.12

Table 8. Model coefficients and 95% confidence intervals (CI) for top logistic regression model of probability of deer presence on Moscow Mountain in Latah County, ID in winter 2020-2021. Estimates and CIs are presented as odds ratios.

Coefficient	Estimate	Low 95% CI	High 95% CI	P-Value
Intercept	0.144	0.118	0.174	<0.001
Depth	0.564	0.314	1.013	0.052
Density	0.782	0.732	0.834	<0.001
Resistance	1.058	0.985	1.128	0.097
Depth:Density	0.355	0.251	0.496	<0.001

Fig. 9. Camera locations on Moscow Mountain in Latah County, ID in winter 2020-2021.

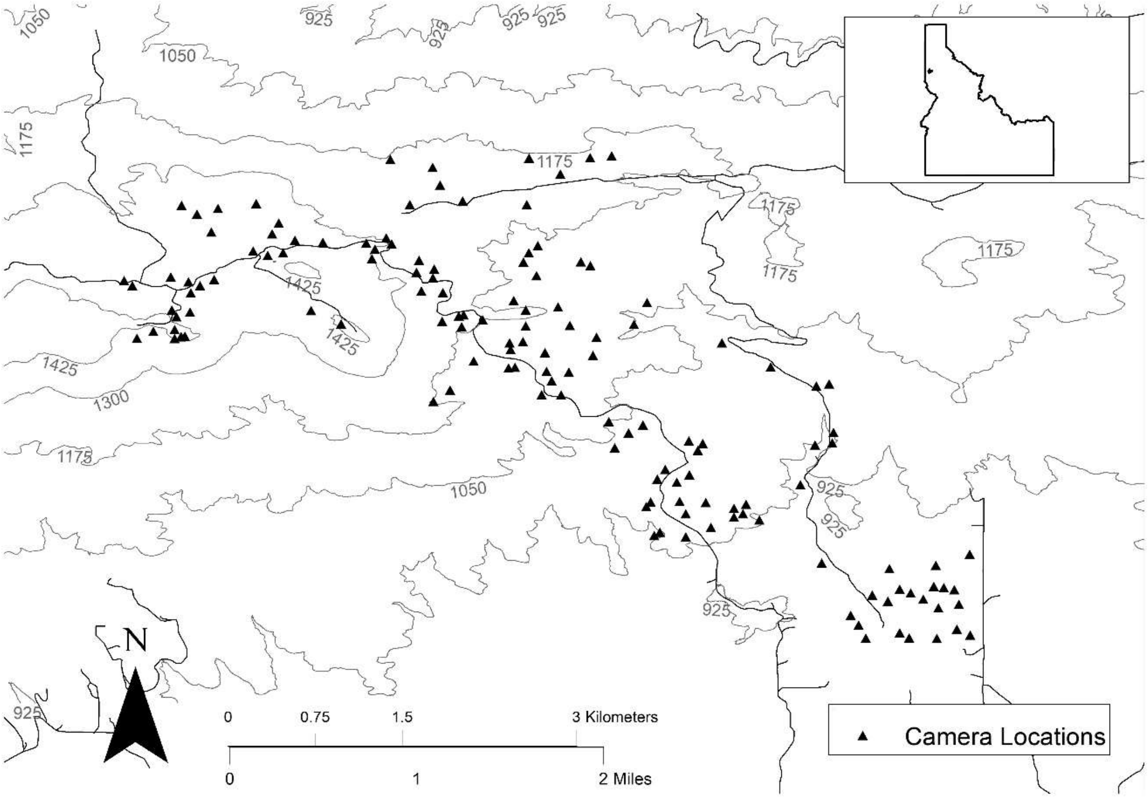

Fig. 15. A) Estimated snow metamorphism index (SMI) versus predicted SMI from a generalized linear model and B) actual ram resistance from field measurements versus predicted maximum ram resistance using the predicted SMI values. The black line is a 1:1 line indicating perfect prediction, while the red line is the best-fit line.

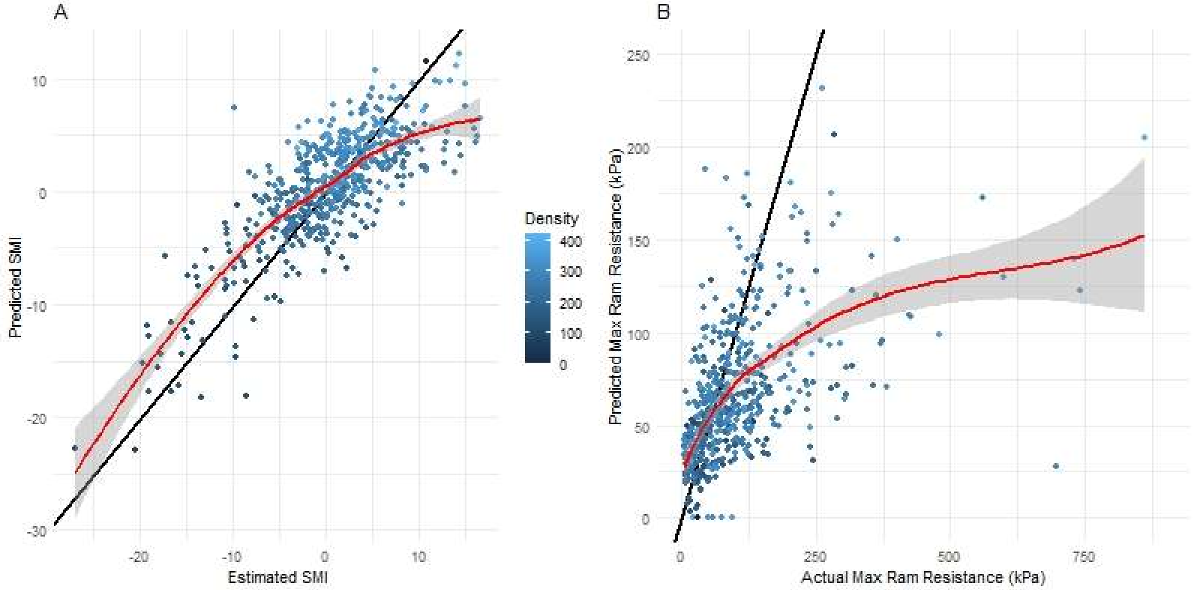

Fig. 16. Mean estimates and 95% confidence intervals for odds ratios of scaled variables in top model of probability of deer presence on Moscow Mountain in Latah County, ID in winter 2020-2021. When variables are scaled, the scalar is provided in the text box above each error bar along with the mean estimate. The dashed line shows where no change in odds occurs.

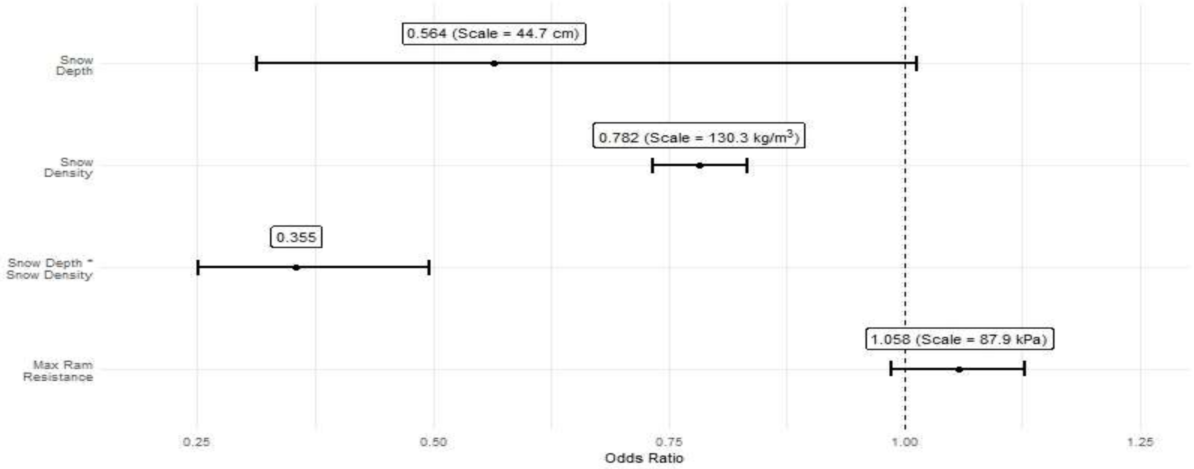

Fig. 17. Predicted probabilities of deer presence on Moscow Mountain in Latah County, ID in winter 2020-2021. Sub-plots are different levels of maximum ram resistance (in kilopascals).

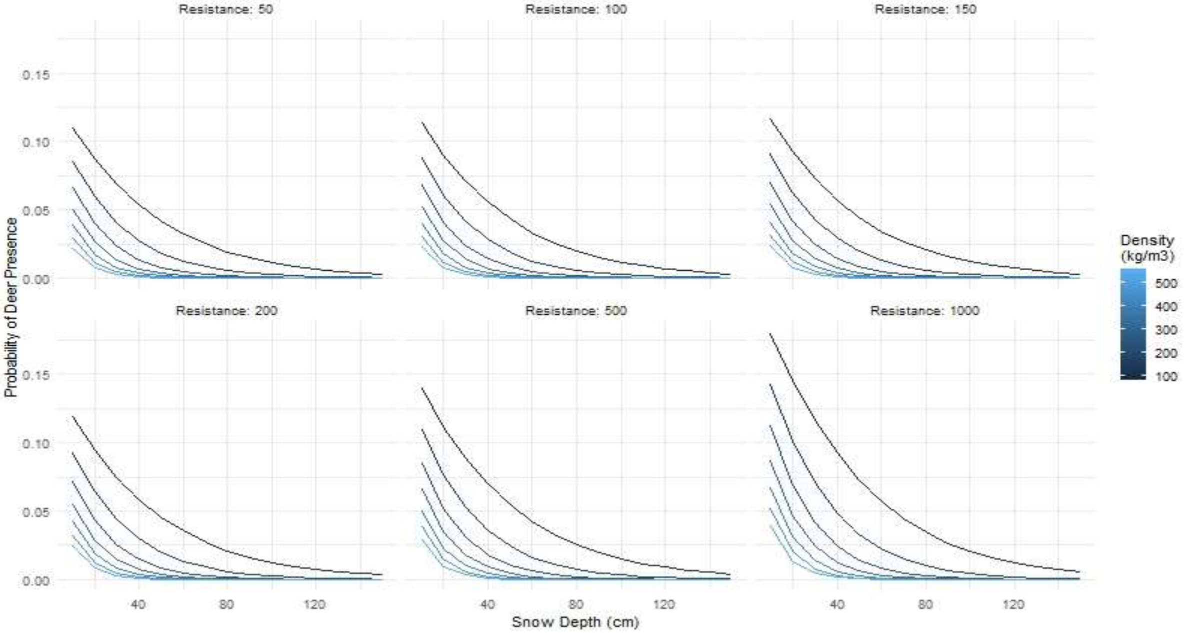

Fig. 18. P-values of differences between AUC scores of two models according to DeLong's test for Receiver Operating Characteristic (ROC) curves for models of probability of deer presence on Moscow Mountain in Latah County, ID in 2020-2021. Zeroes indicate p-values < 0.001.

	Snow Depth	Snow Density	Resistance	Mean Temp	Depth + Temp	Depth * Density + Resistance	Depth * Density	Depth * Density + Resistance + Temp
Depth * Density + Resistance + Temp (AUC = 0.8854)	0	0	0	0	0	0.056	0.435	1
Depth * Density (AUC = 0.8855)	0	0	0	0	0	0.312	1	0.435
Depth * Density + Resistance (AUC = 0.8853)	0	0	0	0	0	1	0.312	0.056
Depth + Temp (AUC = 0.873)	0.128	0	0	0	1	0	0	0
Mean Temp (AUC = 0.7717)	0	0.004	0	1	0	0	0	0
Resistance (AUC = 0.7979)	0	0.627	1	0	0	0	0	0
Snow Density (AUC = 0.8025)	0	1	0.627	0.004	0	0	0	0
Snow Depth (AUC = 0.8722)	1	0	0	0	0.128	0	0	0

Appendix A: Supplemental Information for Chapter 3

Table S1. Models of snow metamorphism index (SMI) used for approximating ram resistance from remote camera data.

Model	Intercept	df	Log Likelihood	AIC	ΔAIC	w_i	R^2
AirTemp * Depth * Density * MeanTemp48 * TotalFT	-20.77	33	-1504.21	3078.92	0.00	1.00	0.61
AirTemp * Depth + Density * MeanTemp48 * TotalFT * Precip	-13.10	20	-1524.74	3091.11	12.19	0.00	0.58
AirTemp * Depth + Density * MeanTemp48 * TotalFT	-14.62	12	-1534.33	3093.26	14.35	0.00	0.56
AirTemp * Depth * Density * MeanTemp48 + TotalFT * Precip	-13.79	20	-1525.94	3093.51	14.59	0.00	0.58
AirTemp * Depth * Density * MeanTemp48 + TotalFT	-15.24	18	-1529.73	3096.78	17.87	0.00	0.57
AirTemp * Depth * Density + MeanTemp48 + TotalFT * Precip	-17.43	13	-1540.35	3107.40	28.49	0.00	0.55
AirTemp * Depth * Density + MeanTemp48 * TotalFT * Precip	-17.19	16	-1537.73	3108.51	29.59	0.00	0.56
AirTemp * Depth * Density + MeanTemp48 * TotalFT	-19.15	12	-1542.53	3109.65	30.74	0.00	0.55
AirTemp * Depth + Density * MeanTemp48 + TotalFT * Precip	-10.50	11	-1544.55	3111.60	32.68	0.00	0.55
AirTemp * Density * MeanTemp48 * TotalFT	-13.19	17	-1538.32	3111.82	32.91	0.00	0.56
AirTemp * Depth * Density + MeanTemp48 + TotalFT	-19.50	11	-1545.48	3113.47	34.55	0.00	0.54
AirTemp * Depth * Density * MeanTemp48 * TotalFT * Precip	-15.63	65	-1484.64	3117.62	38.70	0.00	0.64
AirTemp * Density * MeanTemp48 * TotalFT * Precip	-10.83	33	-1523.92	3118.34	39.42	0.00	0.58
AirTemp * Depth + Density * MeanTemp48 + TotalFT	-11.50	9	-1551.29	3120.92	42.01	0.00	0.53
AirTemp * Density * MeanTemp48 + TotalFT * Precip	-11.06	12	-1552.44	3129.48	50.56	0.00	0.53
AirTemp * Density * MeanTemp48 + TotalFT	-11.89	10	-1557.41	3135.25	56.33	0.00	0.52

AirTemp * Density + MeanTemp48 + TotalFT * Precip	-12.54	9	-1563.38	3145.11	66.19	0.00	0.51
AirTemp * Density + MeanTemp48 * TotalFT * Precip	-12.47	12	-1561.89	3148.38	69.46	0.00	0.52
AirTemp * Depth + Density + MeanTemp48 * TotalFT * Precip	-10.97	13	-1560.90	3148.50	69.58	0.00	0.52
AirTemp * Density + MeanTemp48 * TotalFT	-13.81	8	-1568.76	3153.79	74.87	0.00	0.50
AirTemp * Density + MeanTemp48 + TotalFT	-13.91	7	-1570.30	3154.81	75.89	0.00	0.50
AirTemp * Depth + Density + MeanTemp48 + TotalFT * Precip	-10.73	10	-1569.40	3159.21	80.29	0.00	0.50
AirTemp * Depth + Density + MeanTemp48 * TotalFT	-12.43	9	-1571.93	3162.20	83.28	0.00	0.50
AirTemp * Depth + Density + MeanTemp48 + TotalFT	-12.36	8	-1583.52	3183.32	104.41	0.00	0.48

Table S2. Summary of wildlife detections on Moscow Mountain in Latah County, ID in winter 2020-2021.

Species	Individuals	Images
White-tailed Deer (*Odocoileus virginianus*)	1,788	15,331
Mule Deer (*Odocoileus hemionus*)	136	1,022
Odocoileus spp.	6	24
Rocky Mountain Elk (*Cervus canadensis nelsoni*)	2	18
Moose (*Alces alces*)	523	11,902
Cougar (*Puma concolor*)	2	8
Coyote (*Canis latrans*)	226	930
Bobcat (*Lynx rufus*)	30	142
Snowshoe Hare (*Lepus americanus*)	705	2,330
American Red Squirrel (*Tamiasciurus hudsonicus*)	100	290
North American Porcupine (*Erethizon dorsatum*)	8	42
Raccoon (*Procyon lotor*)	3	11
River otter (*Lontra canadensis*)	1	2
Mouse/vole spp.	1	1
Wild Turkey (*Meleagris galloparvo*)	172	873
Grouse (*Phaseanidae* spp.)	3	6
Other bird spp.	17	50
Unknown	16	176
TOTAL	3,739	33,158

Fig. S1. Density plots of A) snow depth, B) snow density, C) max ram resistance, and D) mean temperature on all days (black lines) and on days with deer detections (orange lines).